Doctoral Dissertation

On Brainless-Robot Approach to Emergence of Motor Patterns

Yoichi Masuda

January 2019

Graduate School of Engineering,

Osaka University

Abstract

Despite the many results suggesting the universal principle in which animals select some gaits consistent with their own body and the surrounding environment, underlying mechanisms for generating the motor patterns in nature animals are still enigmatic. Motor patterns of animals are, in general, produced as a result of interaction between the brain–nerve, body, and uncertain environment. Although this interaction is quite complicated to clarify, it is challenging to identify which factor is crucial in gait generation and transition. In quest of this issue **"what is the source of motor patterns?"**, this thesis proposes two distinct approaches based on robotics and physiology.

This thesis is composed of two parts. In Part I, we develop a quadruped robot that provides a clue to the issue: a sufficient condition for generating the animal gaits. The major contribution of this part is discovery of a new phenomenon in which an extremely simple robot exhibits various animal gaits and adaptive transition. Among them, surprisingly, although the robot has no sensor, microprocessor or explicit controller, the robot changes their gait from walk to gallop according to the input voltages. Moreover, the different types of brainless robots (snake-like and earthworm-like robots) generate various animal motions that suit their own body dynamics and constraint condition from the environments. The key of the adaptivity is an electrical passivity of low-torque DC motors which rotate each limb of the robot. When disturbance force is applied from the ground surface to the foot, load torque is applied to the motor shaft, and the torque affects the rotational speed of the motor through the electrical passivity. In the robot design, instead of considering this delay as disturbance, we exploit this external torque as a control law to adjust the phase differences between the limbs. In other words, the low-torque DC motor is a physical device that has functions of sensor, microprocessor, and actuator.

To evaluate this control strategy, we conduct some walking experiments and show that the robot exhibits the animal gaits and adaptive transition (walk to gallop) according to the input voltages. Moreover, to further investigate this characteristics of the low-torque motor, we conduct some experiments, simulations, and theoretical analysis for two fundamental systems (a spring-mass system and a planar quadruped model). The experiments and simulations show a key feature that the electrical passivity of the motors generates resonant modes of the system. This feature allows the robot to generate various large amplitude motions even with uncertain body structures and environments. In the simulations, we investigate some robustness for parameter variations, such as the motor parameters and initial states. The theoretical results provide an interpretation for the function of the low-torque DC motor.

The proposed method has three clear advantages that differs from the conventional decentralized controllers. First, since the method needs no sensor, microprocessor, certain precise and high-torque motor nor explicit controller, it significantly reduces the implementation cost of conventional decentralized controllers. Second, this method needs no global information of the mechanical system and uses only the local force feedback. Therefore, the module may generate resonance modes of uncertain or unpredictable systems. As a result, if the body and environment dynamics is changed by some troubles, the electrical passivity of motors

instantly adjusts the motions and adapts to these uncertainty. Third, while the proposed control method is powerless and inaccurate, it can generates physically natural motion that suits for the robot body and environment. Although this method does not suit for static and heavy workload tasks (e.g., position control or object manipulation), it will be a new approach for robot design by using this method as a fundamental basis of the robot motor control and adding just a little explicit controllers, such as the motor command from the brain, for the heavy workload tasks.

In Part II, we construct a physiological model showing that the interaction among the local controllers in animal muscles plays an important role for generating motor patterns. The major contribution of this part is to suggest that the fundamental basis of animal motor patterns is found in the body dynamics, and the simple reflex controllers play a role to adjust the waveforms of the body motions. This model utilizes a primitive local control in animals, called the *stretch reflex*, and it is based on the analytical results of the brainless walking, which is introduced in Part I.

To construct the physiological model, we extract a dominant dynamics from the brainless walking in two steps. First, we construct a model based on a dominant dynamics of the brainless walking, called the DFFB (Direct Force Feedback) model. To verify this model, we show some simulations for a spring-mass system and a planar quadruped model. The DFFB model provides almost the same time response and resonant modes as the low-torque DC motor model.

Second, we focus on the other aspect of the DFFB model. The DFFB model can be considered as a rough model of the stretch reflex strategy of actual animals. When an animal muscle receives a force from the body or environment, the stretch reflex functions to maintain its current muscle length. As with the stretch reflex, the DFFB model maintains the current length of the linear actuator by decreasing the oscillation speed when the module detects the reaction force. Based on this analogy, we modify the DFFB model using the physiological knowledge, and as a result, we construct a physiological model that explain a function of the reflex chains. In the simulations, the reflex model automatically generates resonant modes without any explicit neural connection between the models. Moreover, the model adjusts these motor patterns adaptively to changes in the parameters of the body structure. From these results, we conclude that a source of pattern formation is in the body dynamics, because the physical interaction between the local stretch reflex controllers has a function to adjust the waveform of the body motion.

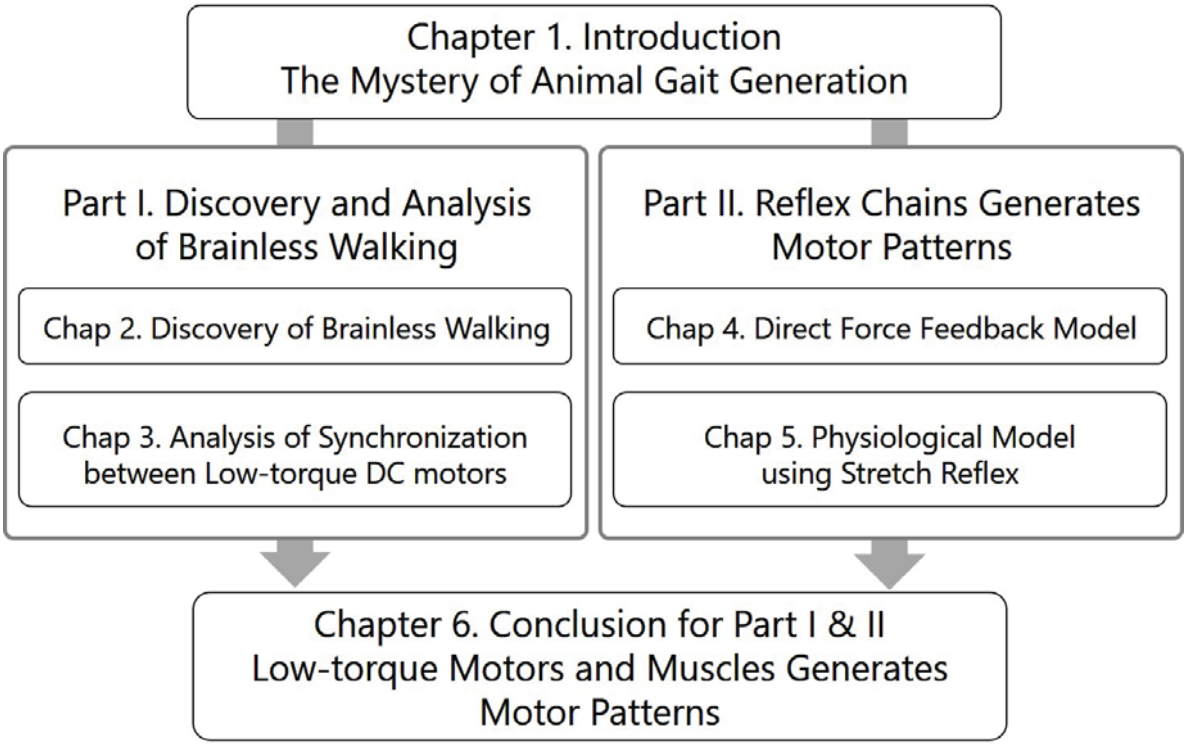

Fig. 1 Outline of this thesis.

Acknowledgement

本論文は，著者が大阪大学大学院機械工学専攻博士後期課程に在籍した間に従事した研究を集成したものである．

本論文の執筆にあたり，石川将人教授には数え切れないほどのご助力をいただきました．特に，私の興味をこの上なく理解してくださったうえで，そのエネルギを最大限に活かすご指導を賜りましたことに心から感謝の意を表します．また，博士後期課程の大先輩としてアドバイスをいただいた南裕樹講師に厚く御礼を申し上げます．

忙しい合間を縫って本論文の副査を快く引き受けてくださり，懇切丁寧なご指導を賜った大須賀公一教授，金子真教授，細田耕教授に厚く御礼を申し上げます．大須賀公一教授には，完成した摩訶不思議なロボット達をいち早く見ていただき，熱い議論を交わす得難い機会をいただきました．金子真教授には，とある機会に口頭発表の極意を授けていただき，今もあらゆる場面で手本として役立てております．細田耕教授には，ロボットから生体まで幅広い内容を扱う本稿に，是非ともご指摘いただきたいという著者の勝手なお願いから副査を引き受けていただき，とても実り多い議論を賜りました．

本研究の発見に辿り着くためには，CREST メンバーを中心とする研究コミュニティの存在が不可欠でした．小林亮教授，青沼仁志教授，杉本靖博准教授，末岡裕一郎助教，そしてメンバーの皆様には，研究を開始した直後の未熟な研究について議論のお時間をいただき，テーマを形作る上で実りある多数のご助言を賜りました．特に，東北大学の石黒章夫教授，加納剛史准教授，大脇大助教，そして無脳ロボットの実現に必要な最後の示唆を与えて下さった伊藤賢太郎講師には，夢と情熱あふれる議論ならびに著者の研究に対する多大なるご助言をいただきましたことを感謝いたします．また，大学は異なれど学年も近く，著者にとっては身近な博士後期課程の先輩であった福原洸助教には，ことあるごとに議論の相手をしていただき良い刺激となりました．

つぎに，本課程に入学する以前から，私の研究能力の基礎作りにご助力賜りました皆様に感謝の意を表します．学部生活において理論研究の素晴らしさと研究に対する姿勢を教えて下さり，修士論文執筆時にも激励を賜った安田一則先生，私が学んできた制御理論をより実践的レベルにまで引き上げて下さった長瀬賢治教授，私の現在の興味と得意分野の源となる知見と哲学を授けて下さった徳田献一講師に厚く御礼を申し上げます．

そして，著者の日々の学生生活を愉快で素晴らしいものに彩ってくれた周囲の皆様，ありがとうございました．石川研究室ならびに大須賀・杉本研究室の皆様方，旧友たち，両親，そして猫に感謝の意を表します．特に，博士後期課程の真っただ中に，協働により新たな研究の世界を切り拓いた浪花啓右さん，藤田帝智君，田中颯樹君に感謝いたします．

最後に，本研究に対してご支援を頂いた JSPS 日本学術振興会様，公益財団法人 立石科学技術振興財団様に感謝を申し上げます．

Contents

List of Figures

Chapter 1

Introduction

1.1 Motivation: The Mystery of Animal Gait Generation

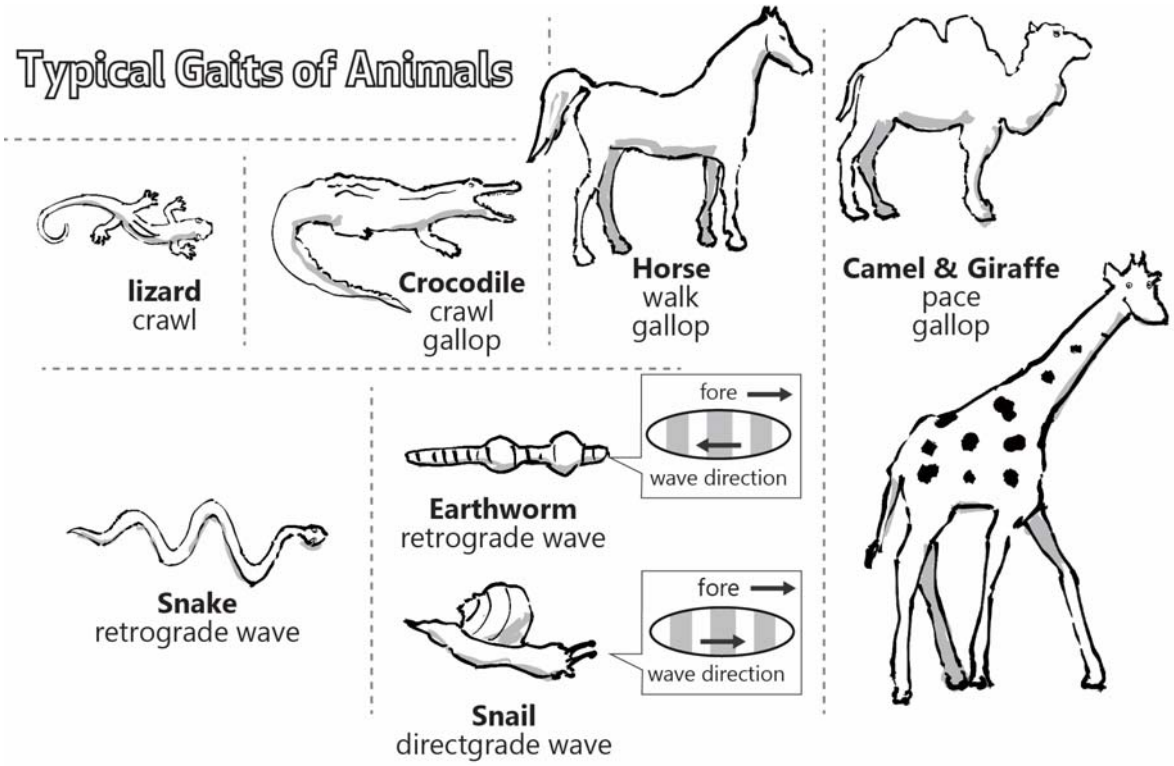

Fig. 1.1 Typical gaits of animals. What is the source?

Animals synchronize their rhythmic motions in each body part (e.g., limbs and spines) and generate versatile motor patterns (Fig. 1.1). These patterns is typically observed in animal locomotions, walking, running, hopping, crawling, swimming, flying and so on, and these skills make nature animals possible to escape from predators or to seek food and water. These characteristic patterns are called the *gaits* and defined as "a pattern of locomotion characteristic of a limited range of speeds, described by quantities of which one or more change discontinuously at transitions to other gaits" [3]. Furthermore, it is well known that animals

change their gaits from one to another adaptively. This behavior, called the *gait transitions*, are typically observed in legged animals: for example, quadrupeds select a suitable one from the six gaits according to their speed [4].

Animal gaits have long been studied in biology [5, 6, 7, 8], and also, attempts to understand mechanisms underlying the gait generation and transition were proposed in some studies. An experiment [9] shows that horses select an efficient gait in terms of oxygen consumption per meter. This result explains an adaptability that animals select some kind of energetically optimal gait to survive in nature with limited resources. Studies with different types of animals [10, 11] show that the stride frequency at the gait transition point (trot–gallop) changes in a regular manner with body mass, and relation between the frequency and mass is linear in logarithmic coordinates. This result suggests that the body dynamics is a crucial factor to determine the transition point, and in other words, some universal principles in which the different species select a suitable gait for their own body dynamics may be hidden.

Despite the many results suggesting the universal principle in which animals select some gaits consistent with their body and the surrounding environment, underlying mechanisms that enable the gait generation in nature animals are still enigmatic. Animal gaits are, in general, produced as a result of interaction between the brain–nerve, body, and uncertain environment. Although this interaction is quite complicated to clarify, it is challenging to identify which factor is crucial in gait generation and transition. In quest of this issue **"what is the source of motor patterns?"**, this thesis show a way to disentangle the interaction using an approach, called the *brainless robotics*.

1.2 Background: Motor Controllers in Animals

In other to find out the source of motor control in animals, a large number of studies have been performed in biology. In these study, some fundamental functions in animals that play an important role for generating motor commands was reported. These functions are mainly produced by two controllers in animals: sensory feedback through the musculoskeletal system, called reflex action, and neural networks in the spinal cord, called central pattern generators.

1.2.1 Local reflex action

Animals have two kinds of motor controllers, voluntary and involuntary ones (Fig. 1.2). The voluntary control from the brain is suitable for complex cognitive tasks, but it causes long delays (220 ms during a simple reaction time task [12]). Whereas the involuntary controller, which is decentralized in each part of the animal body, enables a quick adaptation for changes in the external environment. When an animal body receives some disturbance from the outside world, receptors in musculoskeletal system detect a physical quantity as the sensory information[*1]. The sensory information is sent to motor neurons in the spinal cord through nerve fibers, and the neurons produce motor commands to muscles (Fig. 1.3). Such fundamental response to a stimulus is the *reflex action* belongs to involuntary controls. The reflex

[*1] Strictly speaking, receptors are also in our joints, skins, and so on, but this thesis focus on the receptors in muscles and tendons.

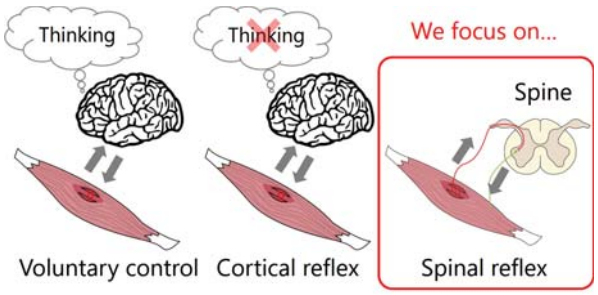

Fig. 1.2 Animals have two kinds of motor controllers, voluntary and involuntary ones (e.g., cortical reflex and spinal reflex).

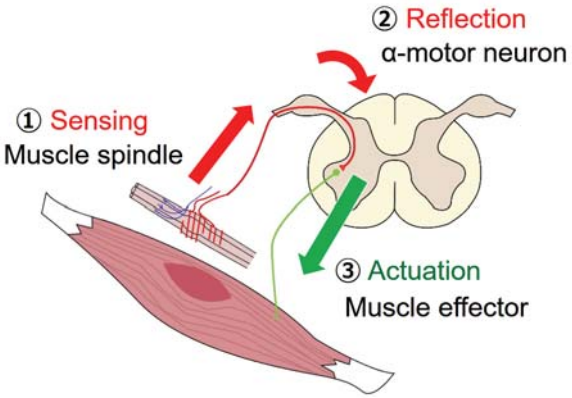

Fig. 1.3 Motor neurons produce motor commands to muscles.

is mainly used for relatively quick and simple motion tasks, and its delay is 30 ms with short-latency and is 50 to 60 ms with long-latency [13].

Functions of the reflex action for motor control have been reported by many researchers. Experiments with decerebrate cats [14] showed that, the neural reflex circuits contribute to adapt muscles activity to variable load [15], to stabilize walking gaits [16], and to compensate for muscle nonlinearities and regulate muscle stiffness [17, 18]. Moreover, this reflex action also contributes to human locomotions [19] during standing [20], walking [21], and hopping [22, 23, 24]. These results suggest that the functions for quick adaptation are embedded in our body as an enormous amount of local controllers. The interaction between the reflex controllers, called the *reflex chains*, is thought to adjusts muscle activities each other and shape the motor patterns.

1.2.2 CPG: Central Pattern Generator

Another key discovery in this research field is neural networks in the spinal cord, called the *central pattern generators* (CPG) [25]. The CPGs are found in both invertebrate and vertebrate animals [26, 27]. The spinal cord of the lamprey, that is isolated from the body, produces fundamental rhythmic activities [28, 29], called the *fictive locomotion*. Moreover CPG in the lamprey entrains its activity to a rhythmic mechanical stimulus from the outside [30]. Similarly, an experiment on cat hind legs [31] showing that the spinal cord could still generate stereotypic alternating activity between flexor and extensor muscles when it was deafferented by cutting the dorsal roots. From these evidences, animals have some kind of controller in their spinal cord to generate rhythms centrally.

In other experiments focusing on locomotor patterns, the decerebrated cat generates a walking gait on a treadmill [32] and also shows gait transition from walk to trot to gallop [33, 34] [*2]. The gait speed in the decerebrated cat depends on the stimulus intensity of a region in the brain stem called *Mesencephalic Locomotor Region* (MLR) [35], and at a threshold, higher stimulation induce gait transition from walk to trot to gallop [14].

[*2] This result is in the unpublished film by T.G. Brown (https://www.youtube.com/watch?v=wPiLLplofYw)

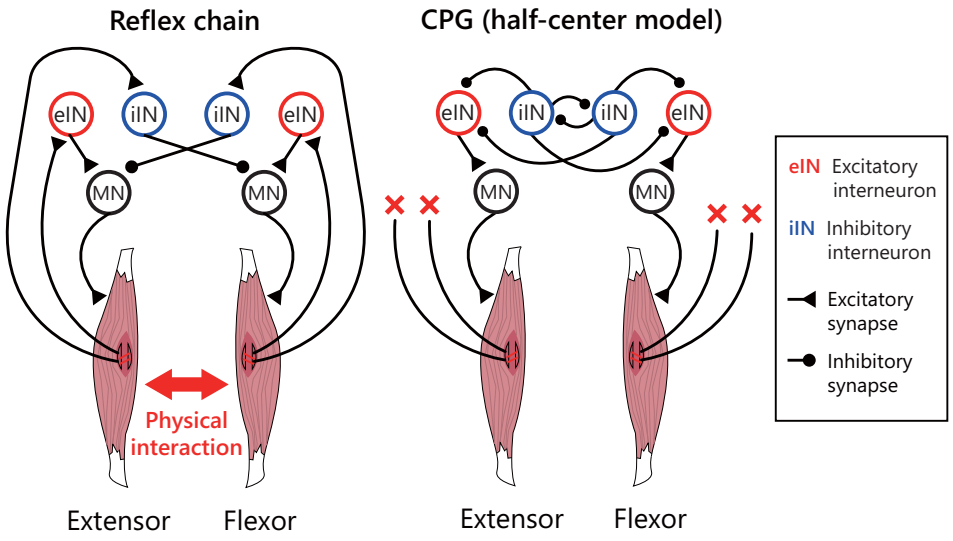

Fig. 1.4 Which is the source of motor patterns, the reflex chain or CPG?. At the beginning of the 19th century, the source of animal motions was widely believed to result from the reflex chains (chains of local sensory feedback through the muscles). However, after a key result, it has been assumed that the source of animal motions is in the CPG, and the reflex chains is not essential for generating the fundamental animal motions.

After the discovery of CPG, attempts to construct mathematical CPG models have been conducted [27, 36]. Roughly speaking, the artificial CPGs are classified into the *connectionist models* and *oscillator models*. First, the connectionist approach, which is based on mathematical neuron models, has been studied in order to explore the relation between inter-neuron connections and generated patterns. A fundamental connectionist model is called the *half-center model* [37], and it shows that mutually coupled neurons generate alternating rhythmic activity. More complex models (e.g., a detailed neural and body model in animals [38] and a multiple-layer CPG models [39, 40, 41]) have been proposed, and it can also produce some cyclic motions.

Next, oscillator models, more abstract models, are based on nonlinear coupled oscillators. The well-known *Kuramoto oscillator* [42] and *Matsuoka oscillator* [43] are relatively easy to describe and analyze theoretically. These CPG models has also been employed as robot controllers [36], however, most of the output waveform was fixed for a given frequency. Recent advances in this field, a CPG model [44] exhibits some animal motions and its transition. However the analysis for the generated motions and its mechanism is still limited, thus a question "how animals generate gait patterns that suit their body and uncertain environment?" is still unclear.

1.2.3 Which is the source of motor patterns, reflex chain or CPG?

As we mentioned above, animals have two different motor controllers, the reflex chains and CPG. Now then—which is the source of motor patterns, the reflex chain or CPG? (Fig. 1.4).

Although this question still remains to be solved, there has been some discussions so far [25, 36, 27]. At the beginning of the 19th century, the source of animal motions was widely

believed to result from the reflex chains (chains of local sensory feedback through the muscles) [45]. This reflex chain hypothesis claims that the sensory feedback plays an important role in triggering switches between different phases in locomotion, such as the stance and swing phase. Contrary to this hypothesis, T.G. Brown showed an evidence that the cat hind legs could generate alternating activity without sensory feedback through the dorsal roots [31]. After this result, it has been assumed that the source of animal motions is in the CPG, and the reflex chains is not essential for generating the fundamental animal motions. We refer to this claim as the CPG hypothesis.

Here, for discussions, we introduce following two terms: the *"rhythm generation"* that provides the temporal rhythmicity, and the *" pattern formation"* that adjust the waveform of the body motions. The CPG hypothesis is clearly correct in terms of the simple "rhythm generation" to generate some fundamental nerve activity (e.g., the heartbeat and the fictive locomotion). However, it is a bit inaccurate in terms of more complex and synergetic "pattern formation". As pointed out in a review [25], the animals utilize both aspect, the reflex chains and CPG, for generating synergetic motor patterns of muscles, such as gait patterns.

Although some physiological studies [41] proposed some novel CPG models (e.g., the multiple-layer CPG model [39, 40] that is composed of two network layers that provide the functions for the "rhythm generation" and "pattern formation" respectively), most of researcher pay only little attention to the body dynamics where the sensory information comes from. It is well known that gait patterns and its frequency are affected by the physical features of animals (body size, mass, and morphology) [3, 4, 46, 10], therefore, the source of gait patterns and adaptive transitions are not provided only by the CPG, but also by the reflex chains through the body dynamics. In this thesis, particularly in Part II, we will investigate the functions of the reflex chains through the body dynamics, rather than the CPG through the neural circuit. The results based on the robot experiments in Part I and the physiological simulation in Part II prove some functions of the reflex chains while generating and adjusting the gait patterns.

1.3 Sub-Issues and Approaches

In the above sections, we overviewed some attempts to understand the mechanisms underlying the gait generation and transition. Although some experimental knowledges have been obtained by these studies, the source of motor patterns that integrate these knowledges is still undiscovered. For this issue, we deal with following two sub-issues in this thesis:

1.3.1 Sub-Issue I. How to investigate the entangled nerve–body–environment interaction?

Animal gaits are generated as a result of the entangled interaction between the brain–nerve, body, and uncertain environment. The major difficulty in this challenge is that the nerve–body–environment dynamics is quite complicated to understand which elements in animals contribute to the gait generation (Fig. 1.5). Most of the traditional studies in nature science have been based on the reductionism, an approach focusing on its constituent elements, to

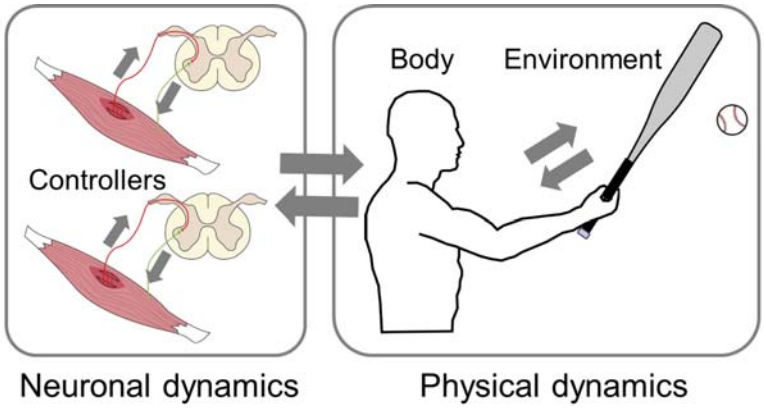

Fig. 1.5 The nerve–body–environment dynamics is quite complicated to understand which elements in animals contribute to the gait generation. To identify the source of motor patterns, we have to simplify the entangled interaction at a proper level in which the gait generation is maintained.

explain a biomechanical phenomenon. However, a motor function in animals is provided by the multiple feedback loops through the mechanical and electro-physiological elements, and also these elements related to another motor functions. Therefore analyses based on the reductionism break some feedback loops and obscure the essential phenomenon that should be observed. To identify the source of motor patterns, we have to simplify the entangled interaction at a proper level in which the gait generation is maintained.

To address this problem, in this thesis, we attempt to extract the source of patterns based on a design approach, called the *minimalistic design approach*. This approach was taken by D. Owaki and A. Ishiguro [47, 48], and they developed a simple legged robot based on it. Their work showed that the animal gaits are generated even without an interlimb neural connection. This result means that a new sufficient condition for the animal gait generation was proved using the simple designed robot (for more detail, see the beginning of Chapter 2). Based on this success, we also take the minimalistic design to address the first issue "How to investigate the entangled nerve–body–environment interaction?". We aim to identify a sufficient condition for the animal gait generation by constructing further simple robots. This extremely simple robot, called the *brainless robot*, has no sensor, microprocessor, or explicit controller, but provides some fruitful suggestion to identify the source of motor patterns.

1.3.2 Sub-Issue II. How to explain actual animal functions with simple robot?

The brainless robot, which will be introduced in Part I, brought us some knowledges of the gait generation conditions. However, roughly speaking, all biomimetic robots are not more than a toy model of animals. Therefore it is difficult to explain the source of motor patterns in terms of physiological view only with the minimalistic design approach. In contrast, the realistic models (the connectionist CPG models) is complicated to even explain and understand its own mechanisms. A new approach is needed to explain the relation between the toy

models (in this thesis, the brainless robot) and actual animal functions.

To solve the issue "How to explain actual animal functions with simple robot?", this thesis takes the *gradual modeling approach*. In this approach, we extract a dominant dynamics of the brainless walking as another new oscillator model, called the *DFFB (direct force feedback) model*. Moreover, gradually modify the DFFB model by focusing on the analogy between the DFFM model and the reflex action in animals. As a result, we will introduce a physiological model that explain some functions of the reflex chains in Part II.

1.4 Thesis Outline and Contributions

This thesis take two distinct based on robotics and physiology. Each approach is described in following two parts:

- Part I. Discovery of Brainless Walking
- Part II. Reflex Chains Generate Motor Patterns

1.4.1 Part I. Discovery of brainless walking

The contributions of Part I are follows:

- Chapter 2
  - develop an extremely simple quadruped robot, called the brainless robot
    - design the robot without a sensor, microprocessor, or explicit controller
    - explain the mechanism of the brainless robot using an electrical passivity of low-torque DC motors
  - conduct some walking experiments
    - show that the robot exhibits various animal gaits and adaptive transition (walk to gallop) according to the input voltages
- Chapter 3
  - conduct some experiments and simulations with a spring-mass system
    - show a key feature that the electrical passivity of the motors generates resonant modes of the system
    - show some robustness for parameter variations

The major contribution in Part I is the discovery of a new phenomenon in which an extremely simple robot exhibits various animal gaits and adaptive transition (Fig. 1.6).

In Chapter 2, we develop a quadruped robot that provides a clue to the issue: a sufficient condition for generating the animal gaits. Among them, surprisingly, although the robot has no sensor, microprocessor, or explicit controller, the robot changes their gait from walk to gallop according to the input voltages. Moreover, the different types of brainless robots (Fig. 1.7) generate various animal motions that suits their own body dynamics and constraint condition from the environments[*3]. The key of the adaptivity is an electrical passivity of low-

[*3] The snake-like robot and earthworm-like robot is introduced in Appendix

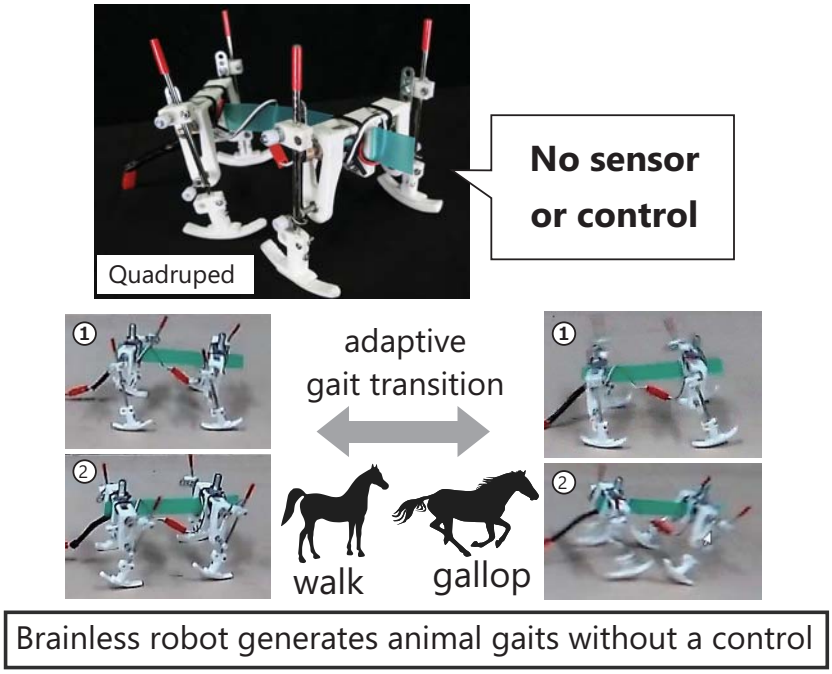

Fig. 1.6 Overview of Part I. We develop the quadruped robot, called the brainless robot. Among them, surprisingly, although the robot has no sensor, microprocessor, or explicit controller, the robot changes their gait from walk to gallop according to the input voltages.

torque DC motors [*4] which rotate each limb of the robot. When a disturbance force is applied from the ground surface to the foot, a load torque is applied to the motor shaft, and the torque affects the rotational speed of the motor through the electrical passivity. In the robot design, instead of considering this delay as a disturbance but exploit this external torque as a control law to adjust the phase differences between the limbs. In other words, the low-torque DC motor is a physical device that has functions of a sensor, microprocessor, and actuator. To evaluate this control strategy, we conduct some walking experiments and show that the robot exhibits various animal gaits and adaptive transition (walk to gallop) according to the input voltages.

In Chapter 3, we show some experiments, simulations, and theoretical results for a spring-mass system and a planar quadruped model to investigate the fundamental characteristics of the low-torque motor. The experiments and simulations show a key feature that the electrical passivity of the motors generates resonant modes of the system. This feature allow the robot to generate various large amplitude motions even with uncertain body structures and environments. In the simulations, we investigate some robustness for parameter variations, such as the motor parameters and initial states. The theoretical results provide an interpretation for the function of the low-torque DC motor.

[*4] Note that this passivity is different from the concept of backdriverbility. Our concept positively utilizes the phase delay due to the low-torque motor for cooperative control

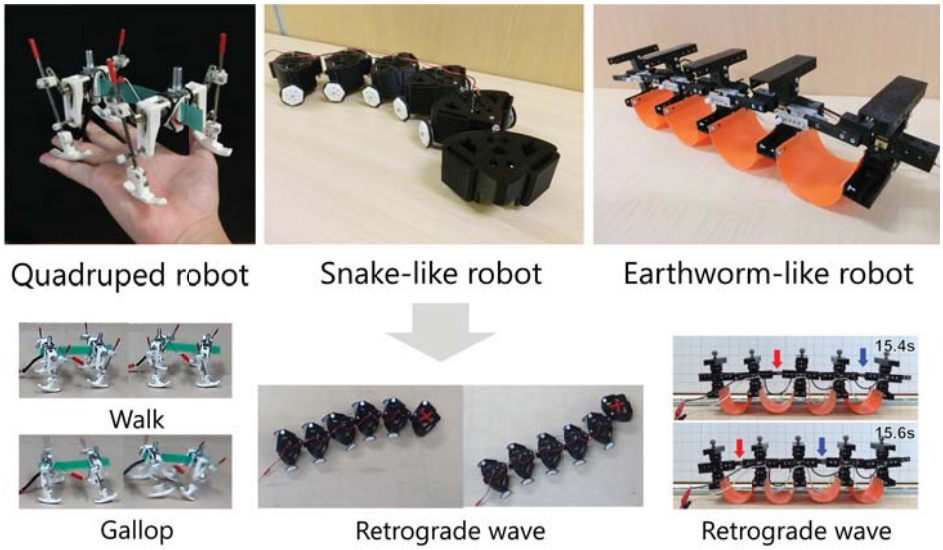

Fig. 1.7 The different types of brainless robots generate various animal motions that suits their own body dynamics and constraint condition from the environments. The snake-like robot and earthworm-like robot is introduced in Appendix.

1.4.2 Part II. Reflex chains generate motor patterns

The contributions of Part II are follows:

- Chapter 4
  - construct a model, called the DFFB model
    - extract a dominant dynamics of the electrical passivity of the low-torque DC motors as another new model
    - design the model without any electrical interaction between the models
  - conduct some simulations with the spring-mass system
    - show that the DFFB model achieves the same function (the resonant mode generation, its transition, and time response) with the low-torque motors
- Chapter 5
  - construct a physiological model of the reflex action in animals
    - design the model without any neuronal interaction between the reflex models
  - conduct some simulations with the spring-mass and musculoskeletal models
    - show that the reflex model achieves the same function (the resonant mode generation, its transition) with the low-torque motors and DFFB model
    - discuss that the reflex chain plays an important role in generating motor patterns

The major contribution in Part II is to suggest that the source of pattern formation is in

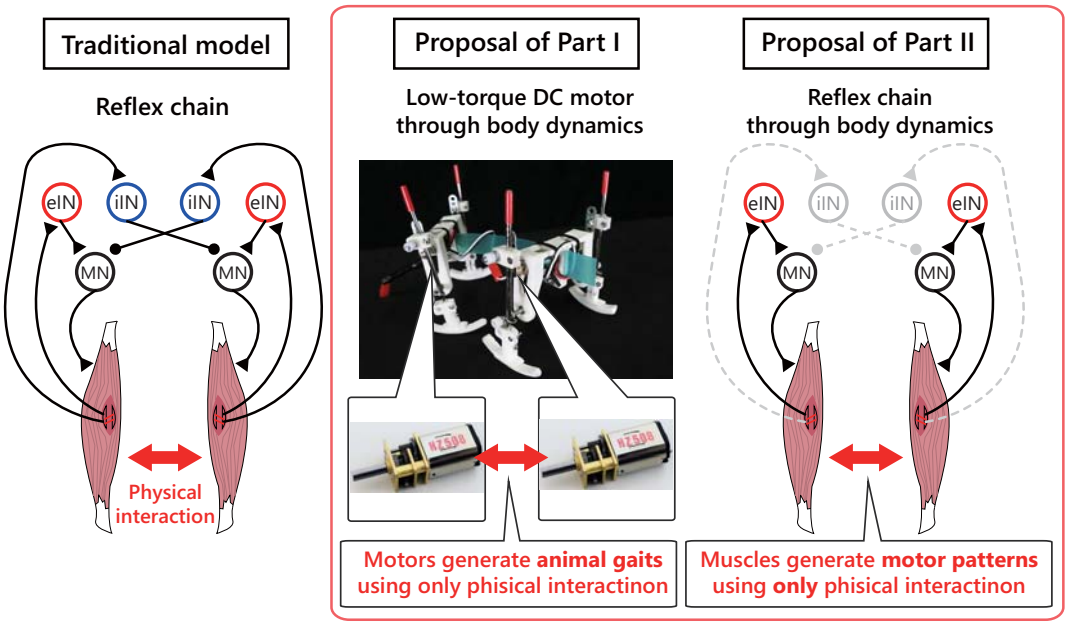

Fig. 1.8 Overview of Part II. We construct a physiological model in which local stretch reflex controllers generate motor patterns through body dynamics (having no neural interaction). This controller is based on the analytical results of the brainless walking, which is introduced in Part I.

the body dynamics, and the physical interaction between the local stretch reflex controllers has a function to adjust the waveforms of the body motions (Fig. 1.8). In the end of Part II, we construct a physiological model showing that the reflex chain through the body dynamics plays an important role in generating motor patterns. This model denotes a primitive local control in animals, called the stretch reflex, and it is based on the analytical results of the brainless walking, which is introduced in Part I. To construct the physiological model, we extract a dominant dynamics of the brainless walking gradually.

In Chapter. 4, we construct a model based on a dominant dynamics of the brainless walking, called the DFFB (Direct Force Feedback) model. To verify the model, we show some simulations for a spring-mass system and a planar quadruped model. The DFFB model provides almost the same time response and resonant modes as the low-torque DC motor model.

In Chapter. 5, we focus on the other aspect of the DFFB model. The DFFB model can be considered as a rough model of the stretch reflex strategy of actual animals. When an animal muscle receives a force from the body or outside world, the stretch reflex functions to maintain its current muscle length. As with the stretch reflex, the DFFB model maintains the current length of the linear actuator by delaying the oscillation speed when the module detects the reaction force. Based on this analogy, we modify the DFFB model using the physiological knowledge, and as a result, we construct a physiological model that explain a function of the reflex chains. In the simulations, the reflex model automatically generates resonant modes without any explicit neural connection between the models. Moreover, the model adjusts these motor patterns adaptively to changes in the parameters of the body structure. From these results, I will conclude that the crucial source of pattern formation is in the body dynamics,

because the physical interaction between the local stretch reflex controllers has a function to adjust the waveform of the body motions.

Part I

Discovery and Analysis of Brainless Walking

Chapter 2

Discovery of Brainless Walking

This chapter shows an extremely simple robot, called the brainless robot, in order to identify a sufficient condition for generating the animal gaits. The major contribution of this chapter is to show that an active walking with autonomous gait adjustment is possible without a sensor, microprocessor, or explicit controller. The brainless robot is capable of generating typical quadruped gaits and selects one of them automatically despite being composed of only a purely physical mechanism. The key of the gait generation is the electrical passivity of a low-torque DC motor. The low-torque DC motor that has the passive dynamics interact with the ground surface, and as a result, the motor adjusts its own phase and makes it as an implicit controller. Experiments show some fundamental characteristics of the robot and its gaits with different input voltage.

In this chapter, first, we introduce some traditional approaches that exploit its body and environment dynamics for robot locomotion. Second, we introduce the brainless robot that has no sensor, microprocessor, or explicit controller. The brainless robot generates various gaits by exploiting the electrical passivity of low-torque DC motors. Finally, we conduct some experiments that show the robot exhibits various animal gaits and adaptive transition (walk to gallop) according to the input voltages.

2.1 Background: Embodied Approach for Robot Locomotion

Animal gaits are generated as a result of the entangled interaction between the dynamics of brain–nerve (controller), body, and uncertain environment. Such controller–body–environment dynamics is quite complicated to understand which element in animals contribute to the gait generation, thus the reductionism break and obscure the essential phenomenon that should be observed. As opposed to the reductionism, attempts to understand the animal locomotor system without reducing to its constituent elements has been in robotics. This attempts based on the holism is called the *embodied robotics* that pay attentions on the interaction between the robot body and environment. The contributions of the physical dynamics for generating adaptive behaviors are gradually revealed in recent embodied approaches [49]. Therefore, first, we show a few historical background to discuss this topic.

2.1.1 Limitation of classical AI and new approach for robotics

The first historical keyword is the *behavior-based approach*. The concept of *behavior-based* was firstly proposed in the context of AI (artificial intelligence). We tend to believe that the advanced computing in our brain function is crucial to achieve the intelligent and adaptive behavior. Therefore, Classical AIs and robots (e.g., *Shakey* [50], the world-famous robot) were also designed that mimics our thinking process. Shakey has an ability to construct internal representation of his surroundings, and it explores the outside world based on an algorithm, called the *sense–model–plan–act* framework. In this framework, first, the robot constructs a model for the outside world using symbolic representation from camera information, and next, calculates the next action plan using the symbol-processing approach. However, the shakey could only explore in a well-designed static world, and its computational processing caused a non-negligible delay in the operation.

Such difficulty, the uncertainty of the outside world that the shakey faced, is also exists in modern robotics. In general control design, we frequently take the model-based approach that represents the system dynamics and uncertainty in the system. Additionally, we assume that the fundamental structure of the system is not varying in process. However, in the real world, the system dynamics of a robot is rapidly changed by the interaction between the robot body and uncertain environment, thus a complete modeling of the outside world is nearly impossible. These problem is typically seen in recent robots, due to its large degree of freedom [51, 52, 53] and with flexible continuum structures [54]. The complex nonlinearity and body elasticity causes various constraint conditions due to the friction, slip, and discontinuous state switching, and their body shape is constantly deformed by the external environment. To deal with these uncertainty, a new paradigm without relying on the internal representation of the outside world was needed.

To deal with these uncertainty of the robot body and outside world, R. Brooks proposed a new paradigm, called the *behavior-based approach* [55, 56]. He mentioned the limitation of the classical AI with the internal representation of the outside world and pointed out the vailed ability in physical dynamics of robot bodies. Specifically, he showed some simple examples in which the body–environment interaction is able to replace some functions of the classical AI. He designed a six-legged robot *Genghis* by combining simple and decentralized controllers that react the outside world. Despite having no internal models of the dynamic outside world, his six-legged robot demonstrated some adaptive behavior. As a result of this great quantum leap, the nature of the research questions was changed into “how to make use of the entangled interaction between a robot body and the outside world?”.

2.1.2 Implicit controller underlying body–environment interaction

When we designer make a robot, the most of controller design would be based on the model-based approach. However, as we mentioned above, a complete modeling of the robot body and uncertain environment is nearly impossible, thus the paradigm of the model-based approach is able to deal with just a part of essential dynamics of the body–environment interaction. A new paradigm to address this issue is the *dynamics-based control* that was proposed

by K. Osuka [57]. The dynamics-based control is defined as a control strategy that utilize the characteristic dynamics of the controlled object, and when the dynamics is emerged from interaction between multiple elements (e.g., the robot body and environment), this control is called the *implicit control*. The "implicit" means that the control law is not described explicitly in a robot. When multiple robots and the environment are interacting, new dynamics will appear there, and in some cases, the dynamics may functions as a controller.

A related example of the implicit control is the *passive dynamic walker* that was proposed by T. McGeer [58]. He constructed a quite simple machine by only pure mechanism and demonstrated bipedal walking gait using the dynamics intrinsic to the robot body and the environment (ground constraint and gravity). After this work, variations of passive dynamic walkers were investigated by S. Collins [59]. A theoretical study [60] by Y. Sugimoto showed that the pure body–environment interaction makes it as an implicit closed-loop controller, and it contributes to the stability for the gait patterns. In terms of the gait transition, experiments with passive quadruped walkers [61, 62] and a passive biped walker [63] exhibited various gaits adaptively. These results suggested that the dynamics of the robot body is crucial to generate its legged locomotion. As a recent advancement of this approach, Osuka's group developed a centipede-like robot, called the *i-CentiPot* [64]. Despite the i-CentiPot has also no explicit controller or cranial nerves, it automatically searches its trajectory in which the robot is able to easily go through the natural environment with a lot of obstacles.

2.1.3 Locomotion as a vibration

Another paradigm similar to the dynamics-based robotics is the *morphological computation*. The way of thinking behind the morphological computation is that a part of the computations for the robot control can be outsourced to dynamics of the robot body itself. A series of studies by Pfeifer's group [65, 66] performed some active motion generation by exploiting morphology and materials of the robot body. The importance of body compliance were shown by Raibert's robots with springy legs in early years [67], and the roles of compliant leg [68, 69, 70] and torso [71] are still investigated. Besides that, large number of robots with body compliance are still designed, such as monopeds [72, 73], bipeds [74], quadrupeds [75], and hexapods [76].

From the viewpoint of the morphological computation, Reis and Iida [77] investigated the fundamental behavior of a simple robot, which composed of an elastic curved beam. Despite such simplicity, the robot enables an energy-efficient hopping by exploiting the coupled dynamics between the elastic body and ground surface. The simple control strategy underlying this robot, which we call the *vibration-based locomotion*, was the robot shaking its own body. The robot has one DC motor with a small rotating mass on the top of elastic body. When the DC motor rotates continuously, the coupled dynamics of the body and environment was entrained in its resonance mode, and thus, the body motion is automatically synchronized with the uncertain environment. Moreover, simple biped with similar concept [78] that generated various locomotion with a U-shaped curved beam was proposed. These results suggest that the intrinsic dynamics in the robot's morphology and materials is useful to generate efficient locomotion with the body and environment dynamics.

2.1.4 Non-neural interlimb interaction generates gaits

Finally, we introduce a key design concept to construct a distributed closed-loop system for robot locomotion, called the *TEGOTAE-based approach* [47]. The TEGOTAE-based control is a scheme to generate the effective driving force that contributes to robot locomotion. D. Owaki and A. Ishiguro introduced a function that quantify TEGOTAE, called the *TEGOTAE function*, and they explained that "TEGOTAE" is a Japanese concept describing the extent to which a perceived reaction matches an expectation [79]. Although the formulation of the TEGOTAE-based controller can be classified as an oscillator model (a kind of CPGs), the clear difference with the conventional CPGs is its simplicity. They demonstrated the capability of this approach with a quadruped robot [47, 48], called the *OSCILLEX*. The OSCILLEX has four decentralized controller in each limbs, and each controller determines the phase of each leg. Remarkable point of this implementation is that the robot has no inter-neural communication, but has the physical (non-neural) inter-limb interaction. Despite each controller is perfectly decentralized, the robot showed adaptive and versatile gait transitions in nature animals. This result suggests that interlimb physical interaction is playing a large role to generate adaptive gaits than we thought.

2.2 Design Principle

The basic design principle of the brainless robot is also based on the embodied robotics, and the aim of this chapter is to identify a sufficient condition for the animal gait generation by constructing an extremely simple robot. In this thesis, we take the following three design principles:

- Vibration-based locomotion for uncertain dynamics
- Actuator synchronization using local force information
- Brainless control using electrical passivity of DC motor

2.2.1 Vibration based locomotion for uncertain dynamics

Locomotor control in unpredictable environments is a major issue for legged robotics. As seen in previous section, a complete modeling of the robot body and uncertain environment is nearly impossible, due to the ground contact condition between the robot leg and environment is rapidly changed by the friction, slip, and discontinuous state switching. To deal with such uncertainty, and also to deal with the entangled controller–body–environment dynamics, we employ the *vibration-based locomotion* which is proposed by M. Reis and F. Iida [77]. Their simple robot generated a hopping motion as a resonant vibration by rotating one DC motor with a mass, and energy efficiency of this approach was evaluated by the cost of transport in their article. Although this result seems to be trivial in terms of the forced vibration with one actuator, it would be an effective strategy for the animal locomotion. Nature animals have to generate large-amplitude motions with a limited amount of energy, and an

experiment [9] showed that actual horses select energy-efficient gaits according to their locomotion speed. Based on this experiment, a study [80] suggested a similarity between the walking motion of a horse and natural vibration modes of its body model. These findings suggest that animals exploit their own intrinsic body dynamics (some type of vibration modes) to generate motions. This thesis shows a design method to extend this vibration-based approach to general mechanical systems with other forms and multiple actuators.

2.2.2 Actuator synchronization using local force information

To vibrate a robot body with multiple actuators, we need a method to synchronize the multiple-actuators and the dynamics of the robot body and environment. A key concept to achieve this *multiple actuator synchronization* is found in the well-known synchronization phenomenon, the *Huygens synchronization* [81]. The phenomenon, in which two pendulum clocks hanging from a wall synchronize with each other, was first observed by Huygens during the 17th century. Although such synchronization is observed in other oscillators in the field of nonlinear dynamics (e.g., the *Van der Pol oscillator* [82], *Kuramoto oscillator* [42], and *Matsuoka oscillator* [43]), most of oscillators need the electrical communications each other unlike the Huygens synchronization. As a recent advance in this area, a simple oscillator [47, 48] allowed a quadruped robot to generate typical animal gaits, and it is called the TEGOTAE control, as introduced in previous section. The remarkable advancement provided the oscillator was that it could adjust its own phase using only the local force information. This concept using only the local forces does not require a precise model and rigorous computation, because the oscillator adjusts its phase according to the reaction forces from the environment. To synchronize multiple actuators in the vibration-based approach, this thesis employ the control principle which exploits the local force information.

2.2.3 Brainless control using electrical passivity of low-torque DC motor

The key concept behind the brainless robot is to exploit the electrical passivity intrinsic to the low-torque DC motor (Fig. 2.1). When a reaction force from the body and environment is applied to the rotating low-torque motor, a load torque applied to the motor, a disturbance corresponding to the load torque occurs in the motor phase. In conventional robot control, this disturbance is compensated by the servo control because it makes a tracking error. In this method, instead of considering this disturbance as an error but exploit it as a sensory feedback law to adjust the phase differences between multiple motors. Thanks to the motor passivity, the phases of the legs that received excessive load stay at that place and support the load, and conversely if the load decreases, the legs kick the ground. In other words, the low-torque DC motor is a physical device in which the functions of the sensor (detecting the load), microprocessor (adjusting the leg phases), and actuator are all included.

The conventional oscillators need a sensor, microprocessor, and some peripheral circuits for each control modules. In contrast, the brainless control without any explicit controller significantly reduces the implementation cost of conventional oscillators.

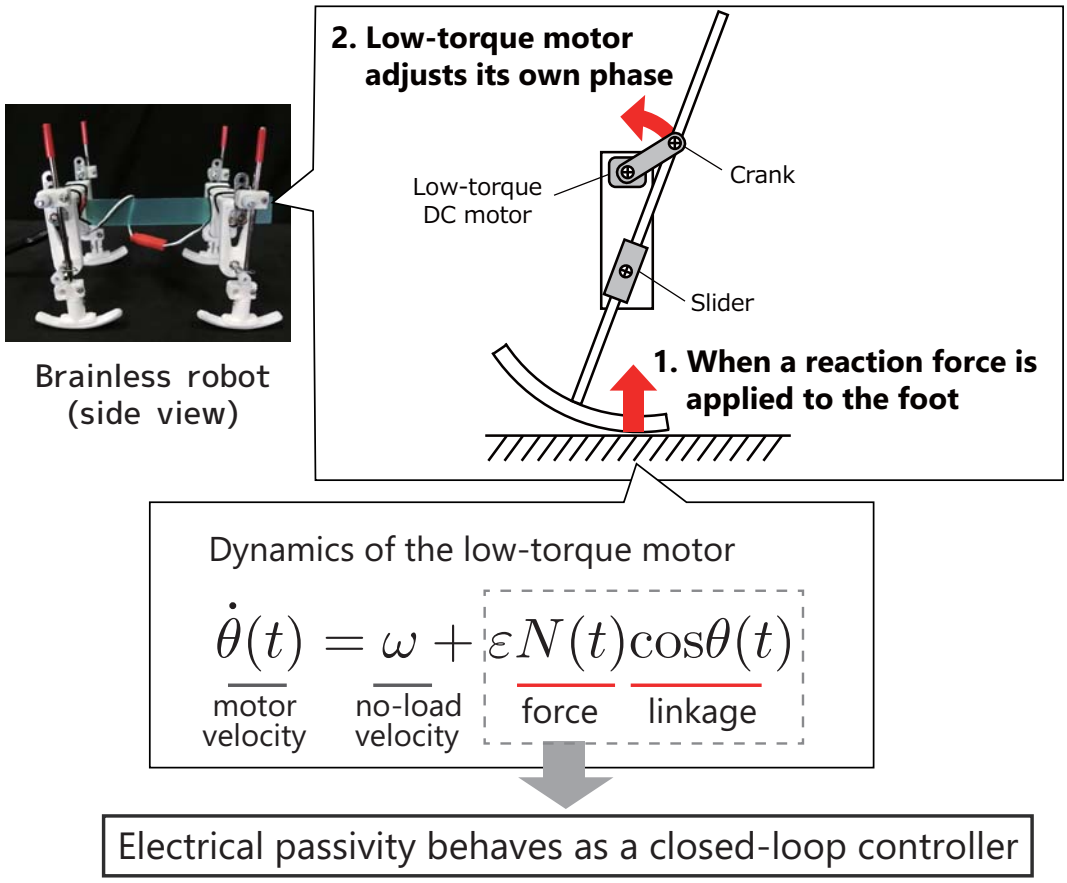

Fig. 2.1 The key concept behind the brainless robot is to exploit the electrical passivity intrinsic to the low-torque DC motor.

2.3 Quadruped Walker “Brainless Ⅱ”

This section describes an extremely simple quadruped robot that exhibits various animal gaits and its transition without a sensor, microprocessor, or explicit controller.

An overview of the quadruped robot, called Brainless Ⅱ, is shown in Fig. 2.2. This robot is composed of fore and hind body modules, and the modules are connected with the flexible spine, as shown in Fig. 2.3. Each module has right and left legs, and each leg has a slider-crank mechanism that is connected to a low-torque DC motor. The total mass of the robot, which includes the two body modules and four legs, is 150 g.

Body Modules

Fig. 2.3(A) illustrates the body modules. Two DC motors (Pololu 75:1 Micro Metal Gearmotor HP) are mounted to each body module (four motors in total), and all the motors are directly connected to a stabilized power source in parallel. When the robot is walking, each DC motor simply rotates continuously under a constant voltage, thus it generates only a simple foot trajectory. However the robot adjusts its own motion by exploiting the motor dynamics without

Fig. 2.2 Overview of Brainless Ⅱ.

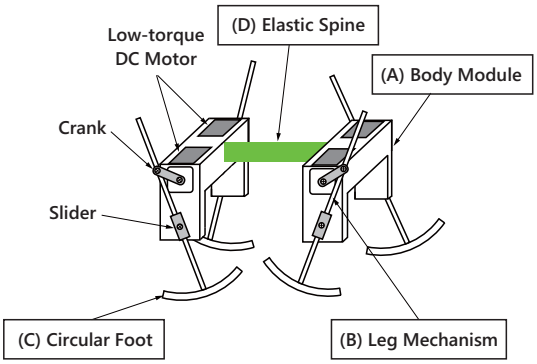

Fig. 2.3 Structure of Brainless Ⅱ. This robot is composed of (A) fore and hind body modules, (B) legs, (C) circular feet, and (D) an flexible spine.

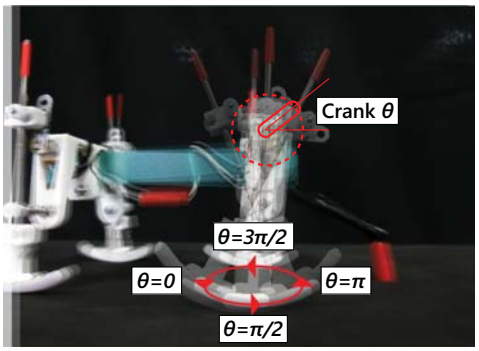

Fig. 2.4 The leg linkage is composed of a crank that connects the motor to the shaft, and a slider that connects the crank to the circular foot. Each leg has one degree of freedom, and the motor in continuous rotation produces a simple elliptic trajectory through the slider-crank linkage.

any closed-loop controller, as described later.

Elastic Spine

The flexible spine plays an important role in quadruped locomotion [83]. In this study, an flexible spine was applied, as shown in Fig. 2.3(D). The spine is a polypropylene strip and is easily deformed by a small external force in the roll direction (Fig. 2.5(a)) and yaw direction (Fig. 2.5(b)). The thickness and width of the spine are 0.75 and 15 mm, respectively. We set the distance between the two body modules to 100 mm.

Leg Linkage

Fig. 2.3(B) illustrates a robot leg. The leg linkage is composed of a crank that connects the motor to the shaft, and a slider that connects the crank to the circular foot. Each leg has one degree of freedom, and the motor in continuous rotation produces a simple elliptic trajectory through the slider-crank linkage. The distance between the left and right legs is 60 mm, and the length of each leg (i.e., the distance between the crank tip and toe tip) is 75 mm. The link-

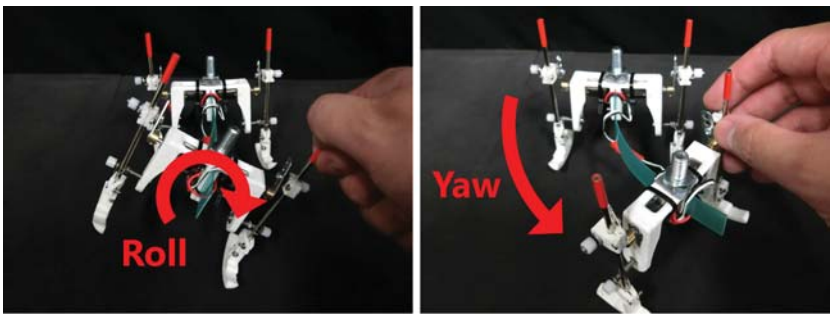

Fig. 2.5 The flexible spine is a polypropylene strip and is easily deformed by a small external force in the (a) roll and (b) yaw directions.

age mechanism of each leg generates an elliptic trajectory of the foot, as shown in Fig. 2.4. The lengths of the major and minor axes of the leg trajectory (Fig. 2.4) are 40 and 28 mm, respectively.

Circular Foot
We introduce a circular foot for smooth switching between the stance and swing phases, as illustratd in Fig. 2.3(C). The shape of the foot was designed as the arc of a circle. The center point of the circle is defined by the same point to the crank tip. The chord of the arc is 45 mm, and the width of the foot is 8 mm.

2.4 Modeling of Leg Mechanism

This robot has any sensor, microprocessor, or explicit controller. The key concept behind the brainless robot is an electrical passivity intrinsic to the low-torque DC motor. When a reaction force from the body and environment is applied to the rotating low-torque motor, followed by a load torque applied to the motor, a disturbance corresponding to the load torque occurs in the motor phase. In this method, we exploit this disturbance as a sensory feedback law to adjust the phase differences between the leg phases.

This section shows a model of the low-torque DC motor and the leg linkage to explain some qualitative features of the brainless robot.

2.4.1 Electrical passivity of low-torque DC motor

The brainless robot exploits the electrical passivity intrinsic to the low-torque DC motor. Let us consider a DC motor that simply rotates continuously under a constant voltage (having no servo control). Moreover, we assume that the motor inertia J, friction D, and inductance L_M are sufficiently small than the motor constant K_M.

When a torque τ is applied to the motor shaft, the mechanical equation of the motion of a DC motor is given by

$$J\ddot{\theta}(t) + D\dot{\theta}(t) = \tau_L(t) + \tau(t), \tag{2.1}$$

where J is the rotor inertia, D is the viscous friction, τ_L is the generated torque by the rotor. The generated torque by the rotor $\tau_L(t)$ is proportional to the current $i(t)$ as

$$\tau_L(t) = K_M i(t), \tag{2.2}$$

where K_M is the motor constant[*1]. Substituting Eq. (2.2) for the mechanical equation of motion (2.1), we get

$$i(t) = \frac{1}{K_M}(J\ddot{\theta}(t) + D\dot{\theta}(t) - \tau(t)). \tag{2.3}$$

The electrical equation of motion of the DC motor is given by

$$V = L_M\dot{i}(t) + Ri(t) + E(t), \tag{2.4}$$

where V is the input voltage to the motor and R is the internal resistance. The counter electromotive voltage $E(t)$ is

$$E(t) = K_M\dot{\theta}(t). \tag{2.5}$$

Substituting Eq. (2.5) for (2.4), we get

$$\dot{\theta}(t) = \frac{1}{K_M}(V - L_M\dot{i}(t) - Ri(t)). \tag{2.6}$$

Using the assumption that the motor inertia J, friction D, and inductance L_M are sufficiently small, and substituting Eq. (2.3) for (2.6), we obtain the motor model as follows:

$$\dot{\theta}(t) = \omega + \bar{\varepsilon}\tau(t), \tag{2.7}$$

where ω denotes the rotational speed of the motor in the no-load state and $\bar{\varepsilon} > 0$ is the sensitivity of the motor to the external torque. Parameters ω and $\bar{\varepsilon}$ are calculated using $\omega = \frac{V}{K_M}$ and $\bar{\varepsilon} = \frac{R}{K_M^2}$. Note that ω is proportional to the input voltage to the motors, and therefore, we can change ω by varying the latter.

2.4.2 Motor and leg linkage functions as closed-loop controller

Next, we construct the linkage model and derive the entire motor–linkage dynamics. In the derivation, we assume that the leg length is sufficiently long than the crank arm.

The low-torque DC motor interacts with the ground surface through the slider-crank linkage (see the geometry in Fig. 2.6). Thanks to the shape of the circular foot, note that the ground contact point is just under the tip of the crank. Using this condition, the axial force in a leg $N'(t)$ is written as:

$$N'(t) = N(t)\sin\phi(t), \tag{2.8}$$

[*1] When the motor has a gear head, the aspect ratio is included in K_M.

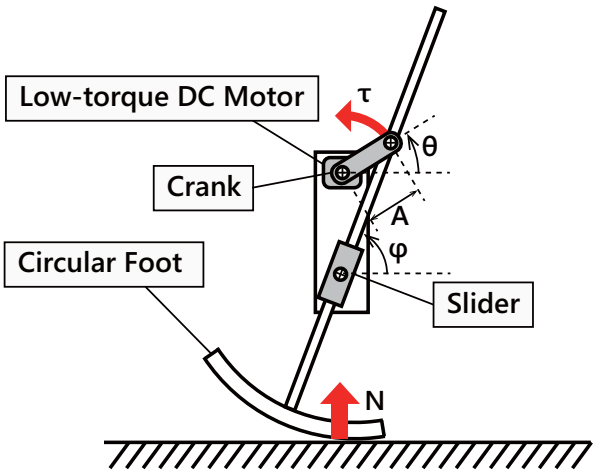

Fig. 2.6 Low-torque DC motor rotates the circular foot through the leg linkage. When a reaction force from the body and environment is applied to the rotating low-torque motor, followed by a load torque applied to the motor, a disturbance corresponding to the load torque occurs in the motor phase. In this method, we exploit this disturbance as a sensory feedback law to adjust the phase differences between the leg phases.

where $N(t)$ is the ground reaction force, ϕ is the leg angle. Here, the positive force $N(t) > 0$ is defined as compressive. The reaction torque from the ground to the motor shaft is calculated by

$$\tau(t) = AN'(t)\sin(\phi(t) - \theta(t)). \tag{2.9}$$

where A is the crank length. By substituting (2.8) for (2.9), and assuming that the leg length is sufficiently long than the crank arm ($\phi(t) \simeq \pi/2$), the motor torque is written as:

$$\tau(t) = AN(t)\cos\theta(t). \tag{2.10}$$

Finally, by substituting (2.10) for (2.7), we get the entire model:

$$\dot{\theta}(t) = \omega + \varepsilon N(t)\cos\theta(t). \tag{2.11}$$

where $\varepsilon = \bar{\varepsilon}A$. From Eq. (2.11), when a reaction force $N(t) > 0$ is applied to the circular foot, the low-torque DC motor adjusts its own phase through the leg linkage. In other words, the passivity of the DC motor for the physical mechanism (2.11) makes it function like a controller. If a large static reaction force $N >> 1$ from the ground is applied, the mechanism (2.11) has a stable equilibrium point $\theta = \pi/2$ and unstable point $\theta = 3\pi/2$. We call this function as a closed-loop controller the *compliant oscillator*.

2.5 Experiments

In this section, we conduct experiments to demonstrate the gait generation ability of the proposed mechanism.

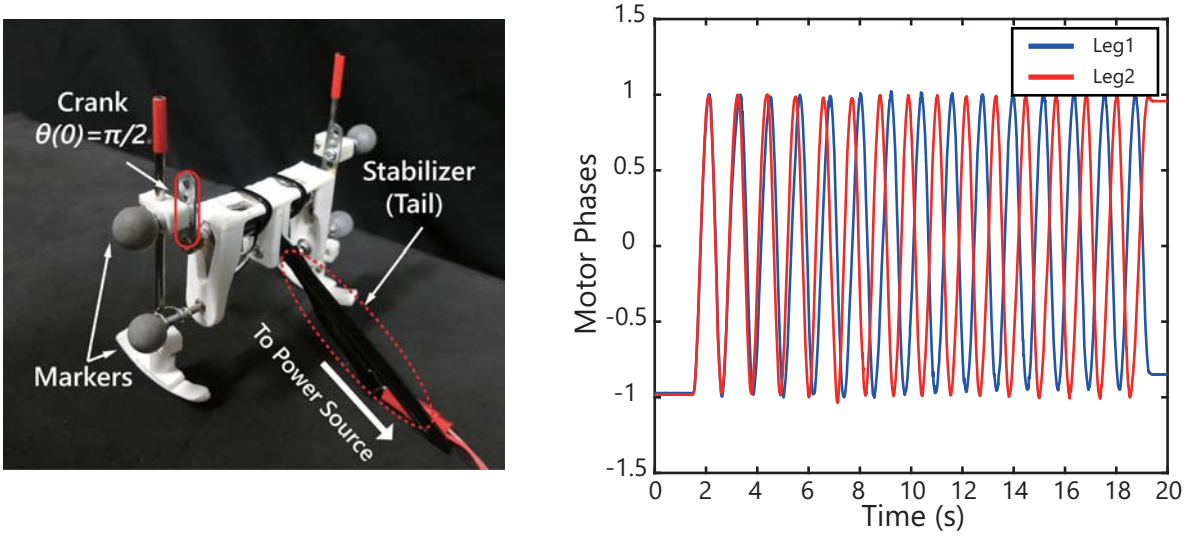

(a) Initial State (b) Experimental Result

Fig. 2.7 Experiment with one body module (biped) to verify the fundamental motion of the leg mechanism with the compliant oscillator. The initial state (a) and motor phases (b) are from the motion capture system. The motor phases converge from the initial state to walking gait (in-phase to anti-phase pattern).

2.5.1 Biped gait

To verify the fundamental motion of the leg mechanism with the compliant oscillator, we conducted an experiment with one body module (biped).

Fig. 2.7(a) shows the initial state of the experiment. The initial phases of the motors were set to $\theta(0) = \pi/2$, and we set a tail made from nylon 66 as a stabilizer that restraint the pitch angle. All of the motors were connected to a stabilized power source in parallel, and the input voltage was 1 V. The phases of the motors were calculated from data with a motion capture system (OptiTrack Prime13, NaturalPoint). Note that the motor phases had some measurement error because of the motion capture system. Therefore, the phases did not reach 1 or -1 in some cases. The phases are calculated by $\cos(\theta + \pi/2)$ because of a geometrical limitation in the calculation. Markers were set on the pivot of the slider, tip of the crank, and top of the motor.

The experimental result is shown in Fig. 2.7(b). The phases of the two motors converged from the initial state to walking gait (in-phase to anti-phase pattern). In other words, the robot put the legs forward in turn, and a roll movement with large amplitude was excited.

2.5.2 Quadruped gaits

This section shows the gaits of the quadruped robot.

Fig. 2.8 shows the experimental setting. Just like with the previous experiment, the motors were connected to a power source in parallel, and the input voltage was changed in 1.5, 2.5, 4

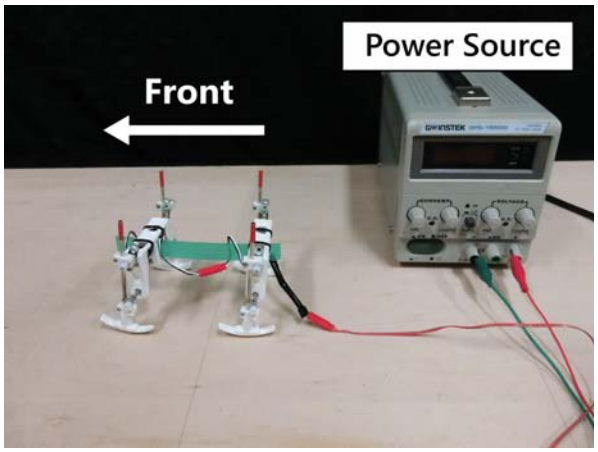

Fig. 2.8 Experimental setting. All of the motors were just connected to a stabilized power source in parallel.

V. The robot motion was calculated from data with a motion capture system, and the Euler rotation sequence is ZXY.

Result with 1.5 **V**
Fig. 2.9 illustrates the results with an input voltage of 1.5 V. From top to bottom, the figure shows the velocity of the center of gravity, roll, pitch, yaw angle, and phases of motors. The roll and yaw are the relative angles of the modules, and the pitch angle is the orientation of the robot. The robot generated low-speed locomotion of around 100 mm/s, and it was clearly unstable because there were transitions between three types of gaits. However, the transitions had a cyclic tendency, and the patterns seem to be repeated in the periods $t \in [5, 10]$, $t \in [10, 15]$, and $t \in [15, 20]$.

Result with 2.5 **V**
Fig. 2.10 illustrates the results with an input voltage of 2.5 V. The top figure shows that the robot generated medium-speed locomotion with large roll and yaw oscillations around 150 mm/s. The robot generated stable locomotion, and the gait converged to a solution with a diagonal-sequence (D-S) walk in which the feet moved in the order:

$$\mathrm{LF} \rightarrow \mathrm{LH} \rightarrow \mathrm{RF} \rightarrow \mathrm{RH}. \tag{2.12}$$

Result with 4 **V**
Fig. 2.11 illustrates the results with an input voltage of 4V. The top figure shows the robot generated medium-speed locomotion with a large pitch oscillation around 200 mm/s, and around $t = 5$ s, the robot was out of the measurable range and fell down at around 6 s. Although the robot generated stable locomotion, the gait converged to another solution of a

transverse gallop, where the feet moved in the order:

$$\text{LF} \rightarrow \text{RH} \rightarrow \text{LH} \rightarrow \text{RF}. \tag{2.13}$$

2.6 Discussion

To achieve the animal gait generation and transition, we developed a quadruped robot that has an extremely simple structure. The fore and hind modules are connected with the flexible spine, and each module has right and left legs. Each leg has a slider-crank mechanism that is connected to a low-torque DC motor. By exploiting the electrical passivity of the low-torque DC motors, in the experiments, the robot generated and selected the typical quadruped gaits despite having no sensor, microprocessor, or explicit controller (using only purely physical mechanisms).

The fundamental behavior of the leg mechanism in Fig. 2.7 was confirmed that the motor phases tended to converge to the anti-phase pattern at low voltage. As shown in Fig. 2.9, gaits and its transition occurred at 1.5 V, and the types of gaits were roughly three. Although these three gaits were clearly unsteady, the pair of left–right legs tended to be in-phase or anti-phase. The tendency was similar to the fundamental characteristics of the single module shown in Fig. 2.7. In terms of the order of transitions, a fixed rule was observed for an order in which a gait changed. This cyclic transition was similar with a beat phenomenon in the field of the mechanical vibration. This result suggests that the robot has three local minimum (tri-stable, but a weak stability), and three modes had closely spaced frequencies, and as a result, these modes mixed at low-speed locomotion.

As shown in Fig. 2.10, the motor phases converged to the D-S walk gait at 2.5 V. The D-S walk is typically observed in monkeys. During the gait, the large roll and yaw oscillation was observed between the body modules. This suggests that the flexible spine, which can easily move in the roll and yaw, contributed to the medium-speed locomotion with the D-S walk.

Fig. 2.11 shows that the locomotion speed increased at 4 V, and the gait was changed from the D-S walk to the transverse gallop. The transverse gallop is typically observed in horses. In contrast to the D-S walk, although the roll and yaw oscillation decreased, and a large pitch oscillation was observed. These two gaits at 2.5 and 4 V seem to correspond to the first and second gaits in Fig. 2.9 at 1.5 V. As increasing the input voltage, the robot selected a suitable gait from the unsteady gaits that are intrinsic to its own body.

During the design process for the robot, an increase of the body weight tended to stabilize the gaits. The body mass would improved the amplitude of motion and contributed to avoid unexpected contact of the swing leg. In the previous version of the robot (lizard-like Brainless I), no similar phenomenon was observed. This suggests that the high center of gravity, which is typical in quadruped mammals, contributed to the secure retraction of the swing leg.

From above discussion, the selected gaits were characterized by the body flexibility, body mass, and height of the center of gravity. Therefore, the steady gaits seem to be selected from the modes that are from its own body dynamics. These results suggest that the robot generated some kind of intrinsic mode (e.g., the natural vibration modes) and quadruped animals also employ similar strategies.

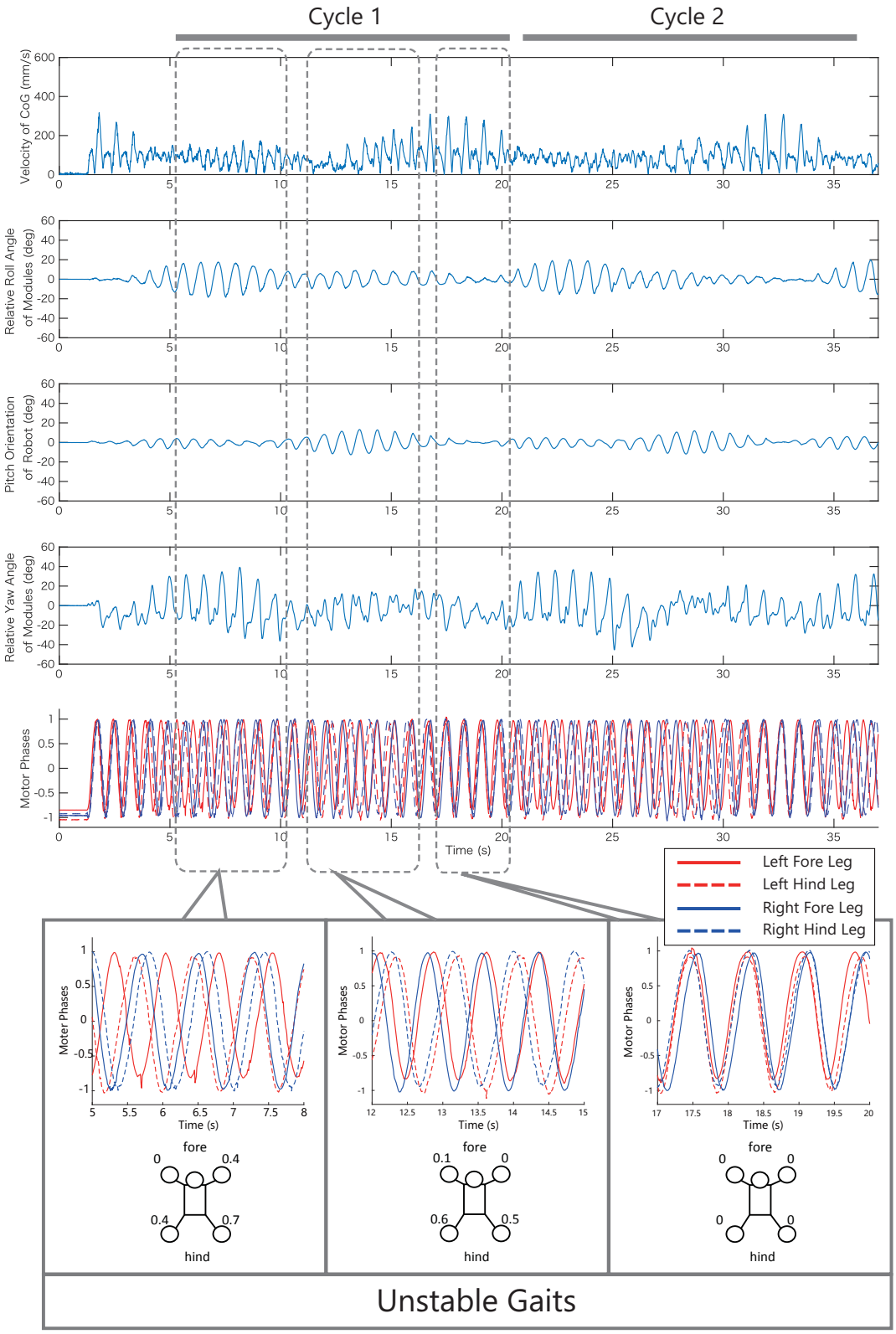

Fig. 2.9 Experimental results with an input voltage of 1.5 V. From top to bottom, velocity of the center of gravity, roll, pitch, yaw angle, motor phases, and gait chart of the quadruped robot. The robot generated unstable gaits.

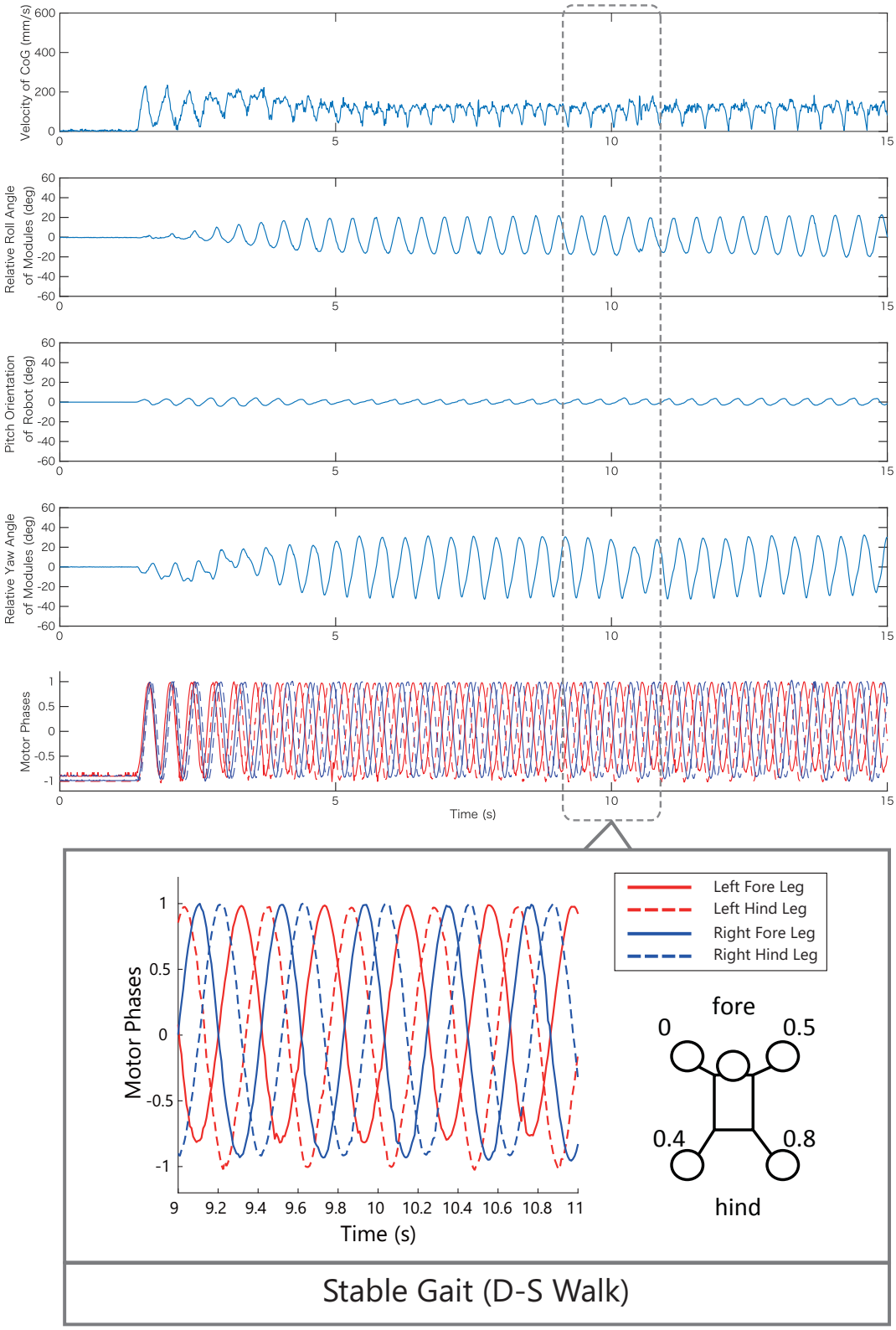

Fig. 2.10 Experimental results with an input voltage of 2.5 V. From top to bottom, velocity of the center of gravity, roll, pitch, yaw angle, motor phases, and gait chart of the quadruped robot. The robot generated a stable gait (D-S walk).

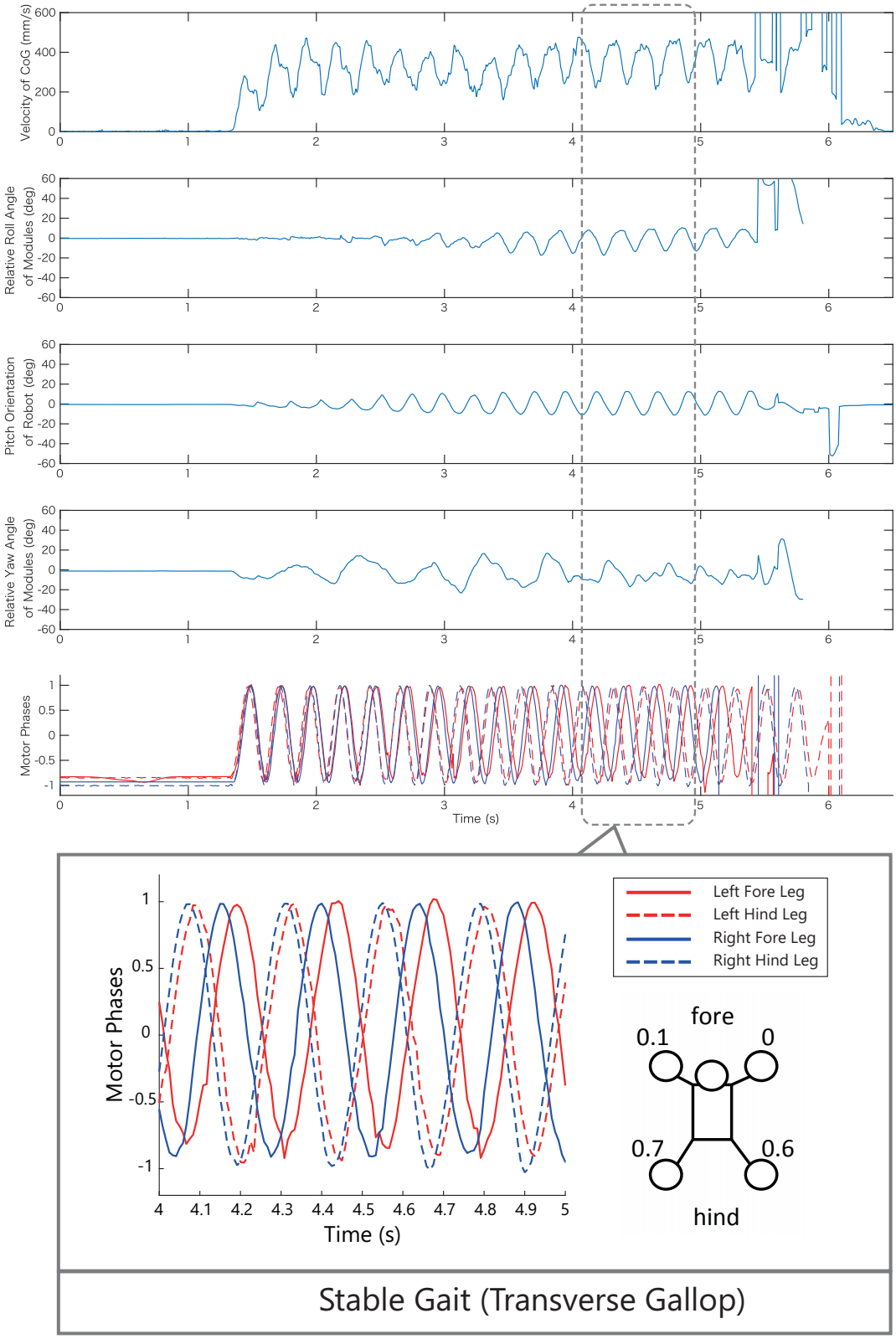

Fig. 2.11 Experimental results with an input voltage of 4 V. From top to bottom, velocity of the center of gravity, roll, pitch, yaw angle, motor phases, and gait chart of the quadruped robot. The robot generated a stable gait (transverse gallop).

Chapter 3

Analysis of Synchronization between Low-torque DC Motors

In Chapter 2, we conducted the experiments with the brainless quadruped robot. This chapter shows some experiments, simulations, and theoretical analysis for more fundamental systems: the spring–mass system and planar quadruped model. A robustness against the initial phase difference and an improvement of the convergence property are reported.

3.1 Compliant Oscillator Module

To apply the compliant oscillator (introduced in Chapter 2) to the fundamental systems, we design a decentralized control module, called the *compliant oscillator module*.

3.1.1 Modeling

Overview of the module is illustrated in Fig. 3.1. The module is composed of a low-torque DC motor and linkage mechanism that is connected to a spring. The linkage is composed of a crank that connects the motor to the shaft, and a slider that connects the crank to the spring. The crank arm is rotated continuously by the DC motor and connected to the linkage that transmits the driving force to the spring. In this implementation, $\phi(t)$ denotes the motor phase, $\tau(t)$ is the reaction torque applied to the motor shaft through the crank arm with link length A, and the positive values are defined as the counter-clockwise direction. N denotes the reaction force from the linkage, and the positive force is defined as compressive force. Note that the definition of the motor phase differs from Fig. 3.1 in Chapter 2 for illustration.

Each module drives natural length $L(t)$ of the spring

$$L(t) = L_0 + A\cos\phi(t), \tag{3.1}$$

where L_0 is the reference length of $L(t)$. The reaction force from the spring is given by

$$N(t) = -kx(t) - c\dot{x}(t), \tag{3.2}$$

where $x(t)$ denotes the displacement of the spring and $k,\ c > 0$ denote the spring and damping

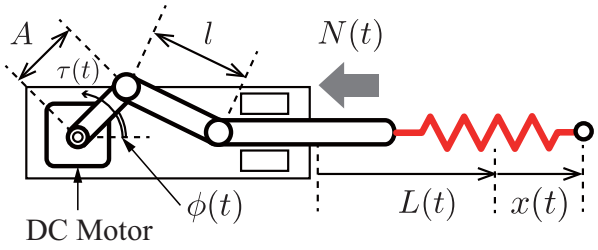

Fig. 3.1 The *compliant oscillator module* is composed of a low-torque DC motor and linkage mechanism connected to a spring.

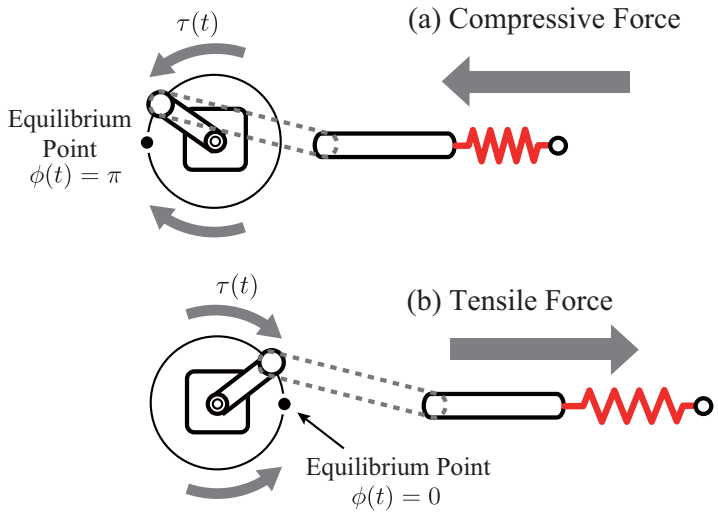

Fig. 3.2 Behavior of the *compliant oscillator*. (a) If a large static reaction force $N >> 1$ is applied, the mechanism has a stable equilibrium point $\theta = \pi$. (b) If a large tensile force $N << -1$ is applied, has a stable equilibrium point $\phi(t) = 0$.

constants. Positive displacement $x(t) > 0$ is defined as the elongation direction.

Next, from Eq. (2.7) in Chapter 2, we revisit the motor model

$$\dot{\phi}(t) = \omega + \bar{\varepsilon}\tau(t), \tag{3.3}$$

where ω denotes the rotational speed of the motor in the no-load state and $\bar{\varepsilon}$ is the control gain. ω and $\bar{\varepsilon}$ are calculated using $\omega = \frac{V}{K_M}$ and $\bar{\varepsilon} = \frac{R}{K_M^2}$, thus ω is proportional to the input voltage to the motors.

If link length l is sufficiently longer than A, motor torque τ is approximated as

$$\tau(t) = AN(t)\sin\phi(t). \tag{3.4}$$

Here, positive force $N(t) > 0$ is considered as the compressive force. Substituting (3.4) for (3.3), we obtain

$$\dot{\phi}(t) = \omega + \bar{\varepsilon}AN(t)\sin\phi(t) \tag{3.5}$$

$$= \omega + \varepsilon N(t)\sin\phi(t), \tag{3.6}$$

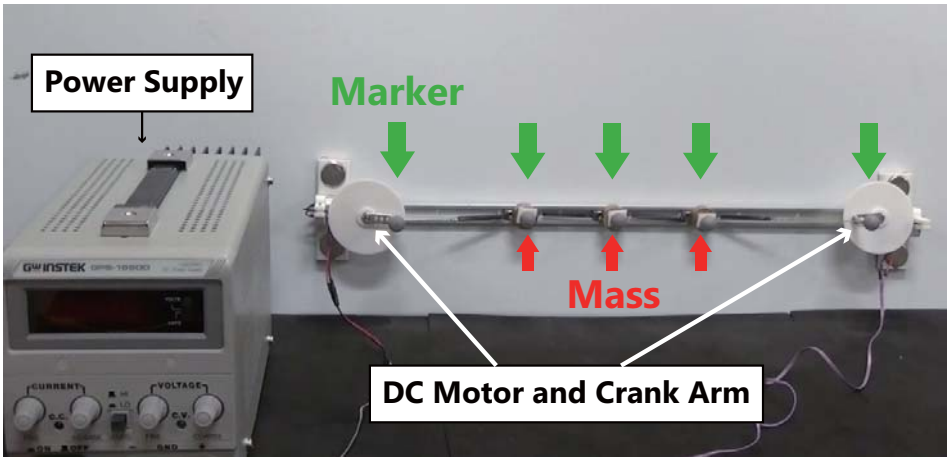

Fig. 3.3 Experimental setting of spring–mass system. Two compliant oscillator modules with low-torque DC motors are fixed on the rail to the left and right. The springs and masses transmit the physical interaction between the motors and adjust the its own phases.

where $\varepsilon = \bar{\varepsilon}A$. Thanks to the electrical passivity of the motor, reaction force N adjusts rotational speed $\dot{\phi}$ as a control law. Thus, the functions of the sensor, controller, and actuator are all included in a low-cost DC motor. If a large static reaction force $N >> 1$ is applied, the mechanism has a stable equilibrium point $\theta = \pi$ (Fig. 3.2(a)), and if a large tensile force $N << -1$ is applied, has a stable equilibrium point $\phi(t) = 0$ (Fig. 3.2(b)).

3.2 Spring–Mass Experiment

In this section, we report a few experiments with a simple spring–mass system to confirm fundamental characteristics of the compliant oscillator module.

3.2.1 Experimental setting

The spring–mass system with the compliant oscillator module is shown in Fig. 3.3. This system is composed of a slide rail, three masses connected by four springs, and two compliant oscillator modules with low-torque DC motors (TAMIYA mini motor gear box (8-speed)) fixed on the rail on the left and right. The distance between the shafts of the two motors is 400 mm, length of each crank is 20 mm, and weight of each mass is 30 g. The springs and masses transmit the physical interaction between the motors and adjust the its own phases.

3.2.2 Results: Spring–mass generated resonance modes

In the experiment, we employed a motion capture system (OptiTrack Prime13, NaturalPoint) to detect the positions of the top of the cranks (motor phases) and masses. The initial phase difference of the two motors is π at each experiment, and the input voltage is increased between 1.0–7.0 V at intervals of 0.5 V.

The experimental results are displayed in Fig. 3.4. The figure shows the time responses of

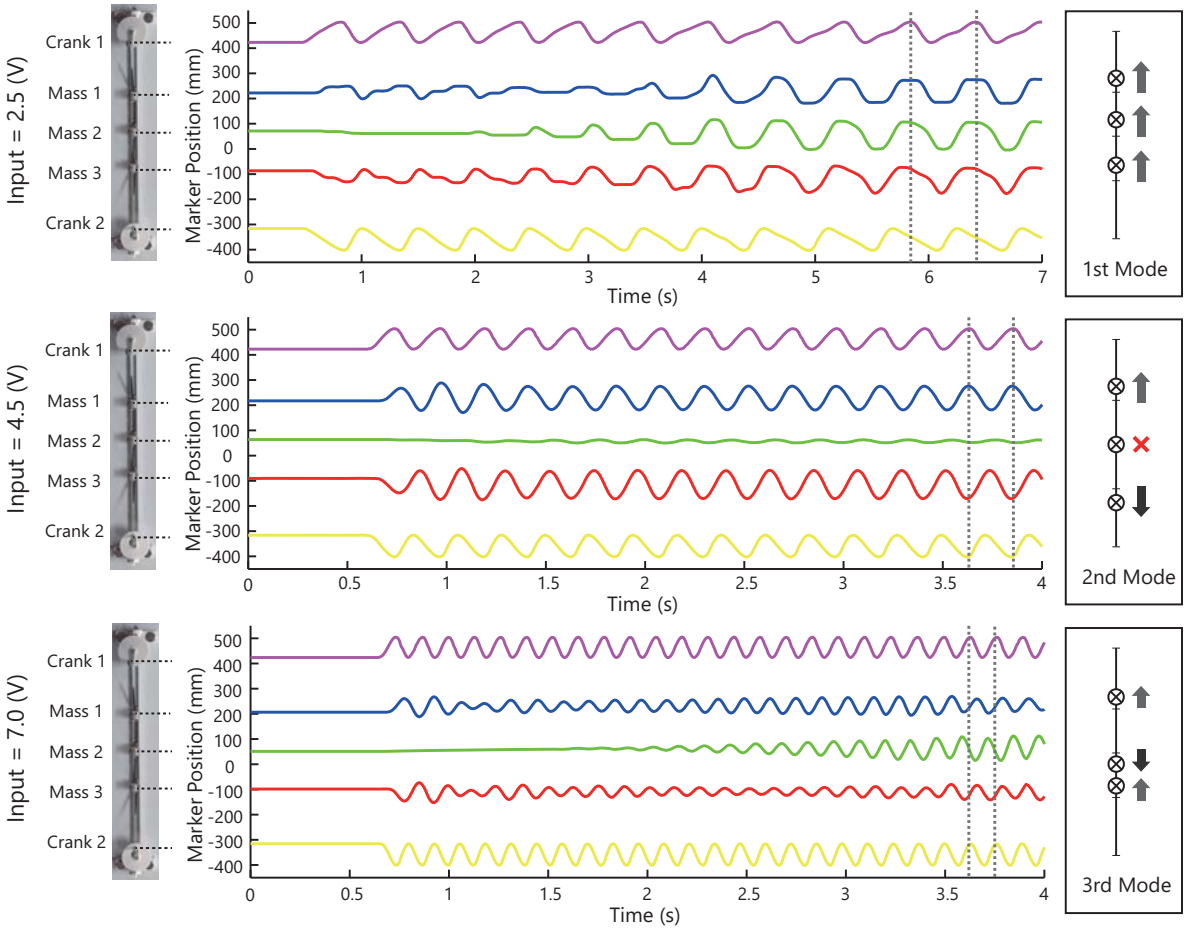

Fig. 3.4 Experimental result. Time responses of the top of the cranks (motor phases) and masses at 2.5, 4.5, and 7.0 V. The system converges to the resonance modes of the spring–mass system as the input voltage increases.

the top of the cranks (the motor phases) and masses at 2.5, 4.5, and 7.0 V. It can be seen that the system converges to different types of limit cycles as the input voltage increases, and the solutions converged to the resonance modes of the spring–mass system as:

$$\mathrm{M}ode1 \rightarrow \mathrm{M}ode2 \rightarrow \mathrm{M}ode3. \tag{3.7}$$

As depicted in the time responses of the cranks, the phases of the cranks are adjusted and synchronized by the reaction force.

3.2.3 Effect of electrical passivity

Figs. 3.5(a)(b)(c) show the plots of the phase and rotational speed of motor1 (angle, radius) = $(\phi,\ \dot{\phi})$ in the polar coordinate. In the figure, the time response are similar to each other. Thanks to the electrical passivity, the rotational speed clearly decreases at $\phi = \pi/2$ and increases in the third quadrant, $\pi < \phi < 3\pi/2$. It means that the rotational speed decreases when the motor is pulled by the mass and increases when the motor pulls the mass, and as a

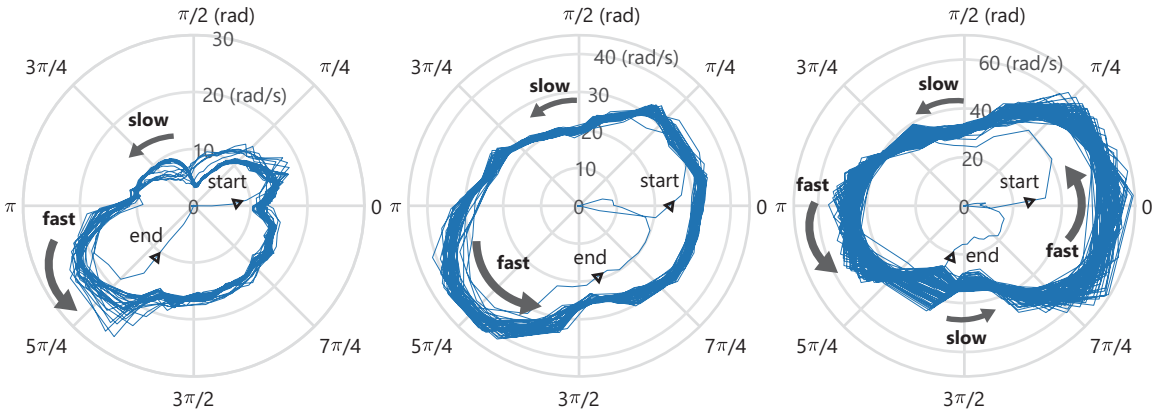

(a) 2.5V (b) 4.5V (c) 7V

Fig. 3.5 Plot of the phase and rotational speed of motor1 (angle, radius) = $(\phi,\ \dot{\phi})$ in the polar coordinate. Thanks to the electrical passivity, the rotational speed is clearly decreased at $\phi = \pi/2$ and increased in the third quadrant, $\pi < \phi < 3\pi/2$.

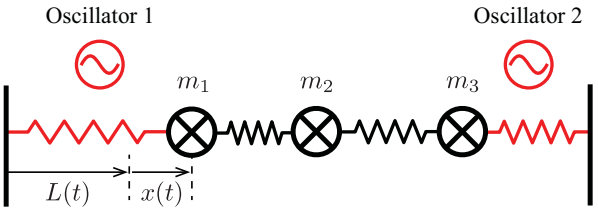

Fig. 3.6 Simulation setting of the spring–mass system. Two compliant oscillator modules are fixed on the wall on the left and right (red spring), and the springs that transmit the physical forces between the modules and masses (black spring).

result the solution converges in a steady limit cycle.

3.3 Spring–Mass Simulation

The experiments were conducted with only a few parameters, thus the effect of the parameters is still unclear due to some limits of the experiments. For more detailed analysis, this section show the simulations of the spring–mass system with various parameters.

3.3.1 Simulation setting

Fig. 3.6 shows the simulation setting. Two compliant oscillator modules are fixed on the wall on the left and right (red spring), and the springs that transmit the physical forces between the modules and masses (black spring). The control input is given by (3.6), and we set the identical parameters for all springs:

$$\varepsilon = 1,\ k = 1,\ c = 0.5,\ L_0 = 1,\ A = 0.3,\ \dot{\phi}(0) = 0, \tag{3.8}$$

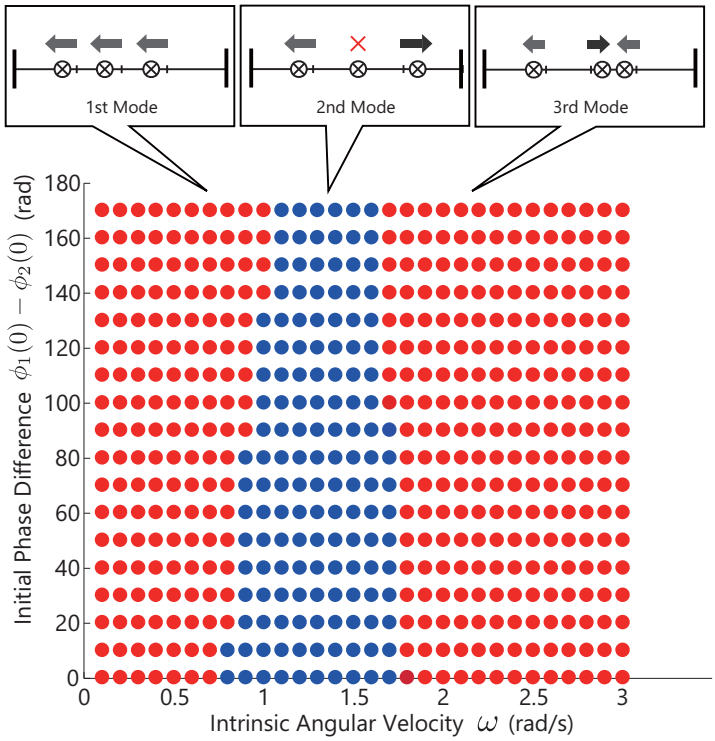

Fig. 3.7 Simulation result of the spring–mass system. The bullet color denotes the phase difference of the converged solutions of the two modules. The blue bullets are the in-phase solutions, and the red bullets are the anti-phase solutions.

3.3.2 Effect of initial phase difference

In this subsection, we present the effect of the initial phase difference of the two actuators on the converged solutions.

The color of the bullets in Fig. 3.7 represents the converged phase difference of the two modules by changing initial phase difference $\phi_1(0) - \phi_2(0)$ and intrinsic angular velocity ω. The bullet color denotes the phase difference of the converged solutions of the two modules. The blue bullets are the in-phase solutions, and the red bullets are the anti-phase solutions. As illustrated in the top figure, the solution converges to one of the resonance modes from any of the initial states, and the phase difference of the converged solutions changes as intrinsic angular velocity ω increases. The first and second transitions occur at around $\omega = 0.8$ and $\omega = 1.7$.

3.3.3 Effect of electrical passivity

Next, we show the effect of the electrical passivity of the low-torque motor to the convergence property. In the simulations, we changed the motor parameter, and small parameter implies low passivity, and $\varepsilon = 0$ implies a high-torque motor without passivity. The phase difference and angular velocity were set as $\phi_1(0) - \phi_2(0) = \pi/3$ and $\omega = 1.5$.

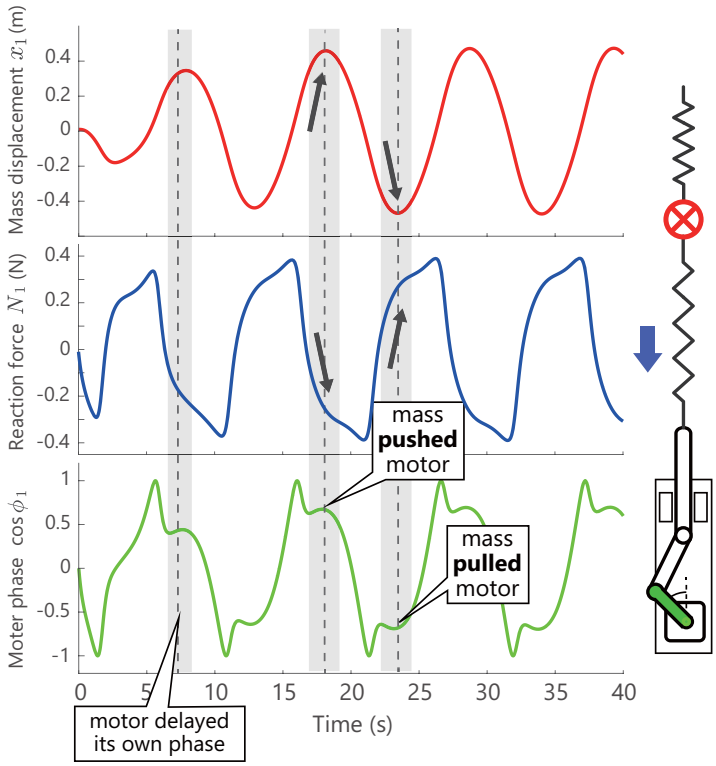

Fig. 3.8 Time response of the phase of motor1, mass1, and the spring force with $\varepsilon = 10$ (very low-torque motor). The motor adjusts its own phase when there exists an unmatching force and mass displacement at $t \in [4, 6]$.

Fig. 3.8 shows the phases of motor1, mass1, and the spring force with $\varepsilon = 10$ (very low-torque motor). It is shown that the motor adjusts its own phase when there exists a unmatching force between the motor and mass at $t \in [4, 6]$. The basic property of the motor phase is the same as in Figs. 3.5(a)(b)(c). Moreover, Fig. 3.9 illustrates the power consumption of the motor, the spring force between the motor and mass, and the rotational speed of the motor in a very low-torque motor with $\varepsilon = 10$. When the motor consume the electrical energy (when the motor torque do work), it functions as that the motor delays its own phase when there exists a large positive or negative spring force between at $t \in [17, 20]$ and $t \in [22, 25]$.

Figs. 3.10 (a)(b)(c) illustrate phase trajectories $(x(t),\ \dot{x}(t))$ in 20 cycles of mass m_1 by changing the motor parameter as $\varepsilon = 0,\ 5,\ 10$. Figs. 3.10 (a)(b)(c) show the trajectory at $\varepsilon = 0$ (high-torque motor), $\varepsilon = 5$ (proposal: low-torque motor), and $\varepsilon = 10$ (proposal: more lower-torque motor). The red plots on the trajectory denote the points when motor phase ϕ_1 passes through $\phi_1 = 0$. Fig. 3.10 (a) exhibits that the red points and trajectory are dispersed and the convergence speed is slow. In Fig. 3.10 (b), the red points converge at an equilibrium point and the trajectory is rapidly stabilized. In Fig. 3.10 (c), the red points converge in one cycle, and the phase converges more rapidly as motor parameter ε increases. The simulations here show that the electrical passivity of the DC motor improves the convergence property.

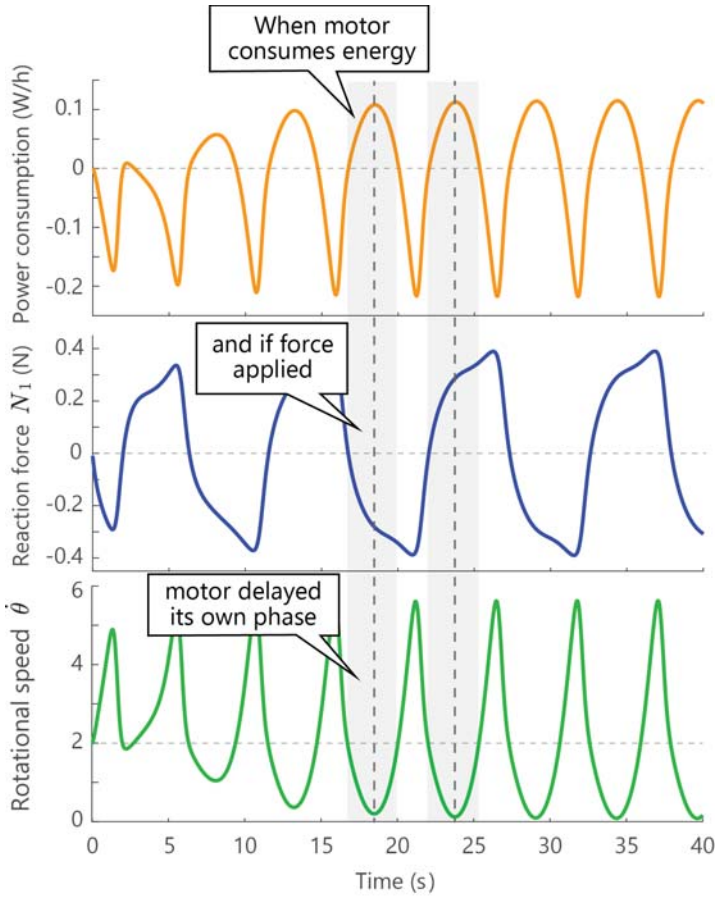

Fig. 3.9 Time response of the power consumption of the motor, the spring force between the motor and mass, and the rotational speed of the motor in a very low-torque motor with $\varepsilon = 10$. When the motor consume the electrical energy (when the motor torque do work), it functions as that the motor delays its own phase when there exists a large positive or negative spring force at $t \in [17, 20]$ and $t \in [22, 25]$.

3.4 Planar Quadruped Robot Simulation

This model is based on the sagittal plane model [1], which can be considered as a quadruped robot model in side view. Fig. 3.11 shows the simulation setting. Although the robot is quadruped, we assume that the motions of the left legs is mirrored to the right ones. Based on the figure, we apply the control modules to each leg, and the ground reaction force is applied to the modules through the springy legs.

$$M\ddot{x}_g = -h(N_1) - h(N_2) - Mg \tag{3.9}$$

$$I\ddot{\theta} = \frac{d}{2}\{h(N_1) - h(N_2)\}\cos\theta, \tag{3.10}$$

where x_g is the position of the center of gravity that is defined by $x_g = (x_1 + x_2)/2$, g is the gravity constant, M, I denote the body mass and moment of inertia. L is the body length,

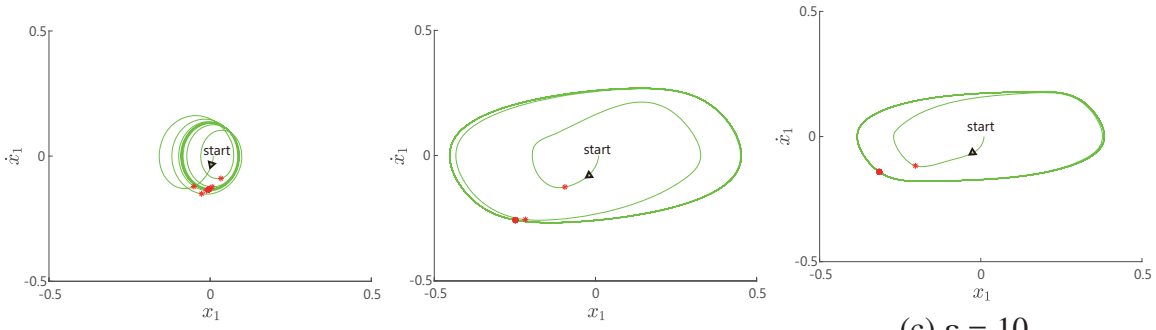

(a) $\varepsilon = 0$
high-torque motor

(b) $\varepsilon = 5$
low-torque motor (proposal)

(c) $\varepsilon = 10$
more lower-torque motor (proposal)

Fig. 3.10 The phase trajectories $(x(t),\ \dot{x}(t))$ in 20 cycles of mass m_1 with motor parameters $\varepsilon = 1,\ 5,\ 10$. (a) The red points and trajectory are dispersed, and the convergence speed is slow. (b) The red points converge at an equilibrium point and the trajectory is rapidly stabilized. (c) The red point converges in one cycle, and the phase converges more rapidly as motor parameter ε increases.

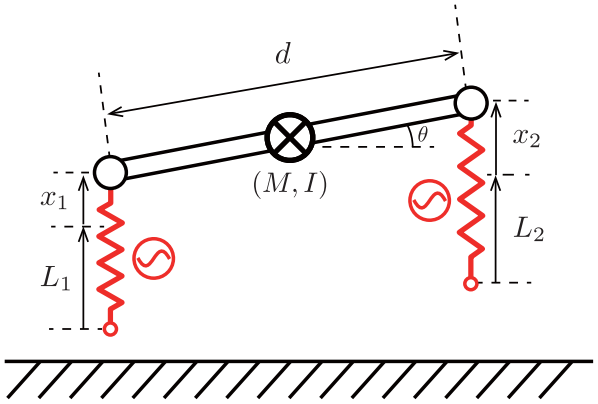

Fig. 3.11 The planar quadruped robot model [1]. The motions of the left side of the model is mirrored to right. Two control module are applied to the fore and hind legs.

and $N_1,\ N_2$ are the reaction forces in the fore and hind legs. We assume that the robot body is a uniform rod, and the mass of the feet is sufficiently small. The flight phase of the legs is defined by the switching function $h(*)$ as follows:

$$h(*) = \begin{cases} 0 & (* < 0) \\ * & (* \geq 0) \end{cases} . \tag{3.11}$$

Here, ground reaction forces N_i in each leg i to be zero when the corresponding leg leaves the ground.

We set the following same parameters for all the models:

$$\begin{aligned} &\varepsilon = 1,\ k = 1000,\ c = 10,\ L_0 = 0.1,\ A = 0.03, \\ &d = 0.2,\ M = 0.25, \dot{\phi}(0) = 0. \end{aligned} \tag{3.12}$$

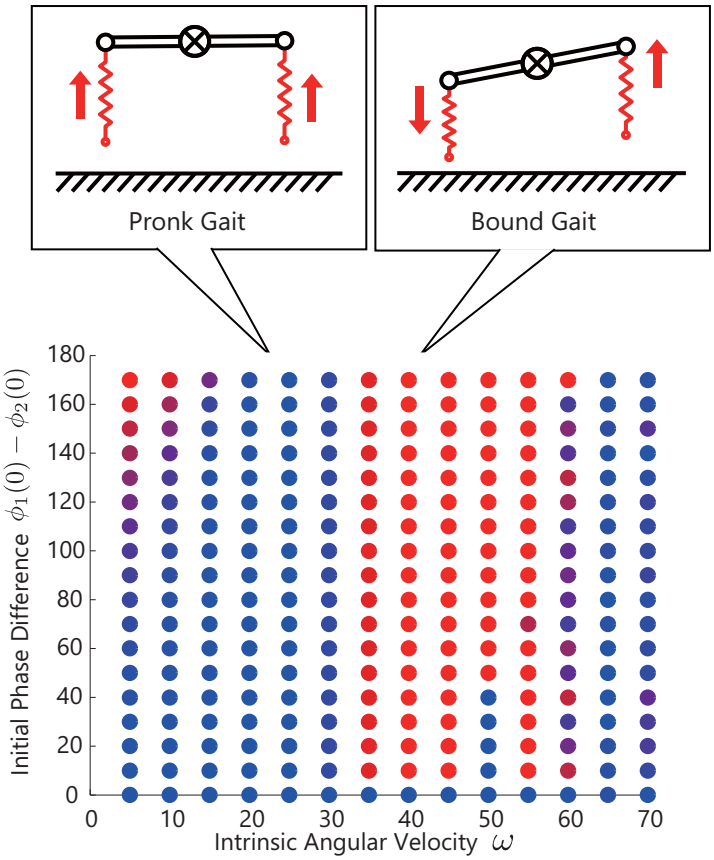

Fig. 3.12 Simulation result of the quadruped model. The bullet color denotes the phase difference of the converged solutions of the two modules. The blue and red bullets are the in-phase and anti-phase solutions.

Fig. 3.12 shows the simulation result by changing initial phase difference $\phi_1(0) - \phi_2(0)$ of the two modules and intrinsic angular velocity ω. The bullet color denotes the phase difference of the converged solutions of the two modules, and the blue bullets are the in-phase solutions, and the red bullets are the anti-phase solutions. In this figure, the transition occurs at around $\omega = 35$, and two types of motion patterns are generated in the animals as

$$\mathrm{P}ronk \rightarrow \mathrm{B}ound, \tag{3.13}$$

as illustrated in the top of the figure. However, around over $\omega = 50$, the phase difference does not converge because the feedback is relatively smaller than ω. This simulation shows an example that the proposed control module can also generate resonance motions in a nonlinear legged robot system.

3.5 Theoretical Analysis

In this section, we propose some theoretical results for the compliant oscillator (3.6). The major contribution of this section is that the dynamics of the compliant oscillator (3.6) may

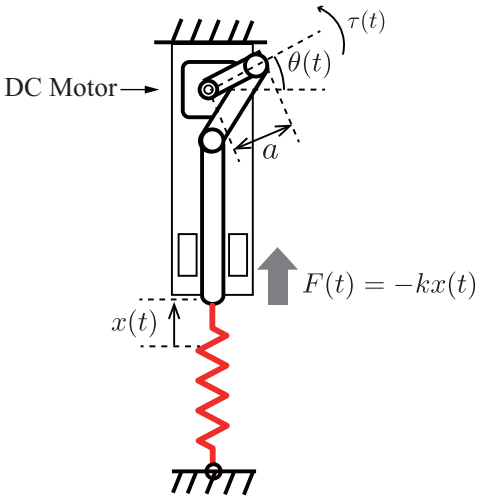

Fig. 3.13 The compliant oscillator for a theoretical analysis

be interpreted as a closed-loop controller that make the system to down the slope of an energy potential.

3.5.1 Modeling

For a theoretical analysis, we simplify the compliant oscillator model as shown in Fig. 3.13. This system is composed of a low-torque DC motor (which has the electrical passivity) and a slider–crank linkage. A spring is fixed on the tip of the slider, and the other tip of the spring and the motor are fixed on the environment. When the motor rotates the crank, the slider generates up–down cycles and drive the spring.

The displacement of the slider tip $x(t)$ is written using the motor phase $\phi(t)$ and the crank length a as:

$$x(t) = a \sin \phi(t), \tag{3.14}$$

and the spring force F is written as:

$$F(t) = -kx(t), \tag{3.15}$$

where the positive force $F > 0$ is defined as a force pushing the slider.

Next, remind the equation (3.6), the dynamics of the low-torque DC motor is

$$\dot{\phi}(t) = \omega + \varepsilon F(t) \cos \phi(t). \tag{3.16}$$

3.5.2 An interpretation using spring energy

The following lemma suggests that the dynamics of the compliant oscillator (3.6) may be interpreted as a closed-loop controller that make the system to down the slope of a potential of spring energy.

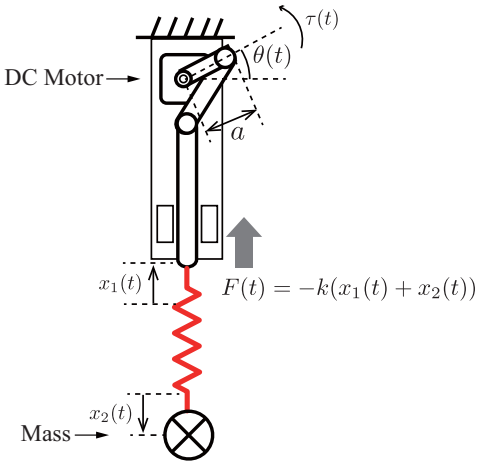

Fig. 3.14 The compliant oscillator with a mass for a theoretical analysis

Lemma 1 Let us consider the system (3.14),(3.15),(3.16) that is illustrated in Fig. 3.13, the dynamics of the compliant oscillator (3.16) is written as:

$$\dot{\phi}(t) = \omega - \frac{\varepsilon}{a}\frac{\partial I_{\text{spring}}(t)}{\partial \phi(t)}. \tag{3.17}$$

Proof 1 Substituting the slider displacement (3.14) and spring force (3.15) for the motor dynamics (3.16), we get

$$\dot{\phi}(t) = \omega - \varepsilon k x(t) \cos\phi(t) \tag{3.18}$$

$$= \omega - \frac{\varepsilon}{a} k x(t) \frac{\partial x(t)}{\partial \phi(t)}, \tag{3.19}$$

where using the spring energy $I_{\text{spring}} = \frac{1}{2}kx(t)^2$, the dynamics of the compliant oscillator can be written as:

$$\dot{\phi}(t) = \omega - \frac{\varepsilon}{a}\frac{\partial I_{\text{spring}}(t)}{\partial \phi(t)}, \tag{3.20}$$

□

From the second term of the right side of (3.17), momentary, the motor phase ϕ might be adjusted as the system down the slope of a potential of spring energy I_{spring}. This result may be interpreted that the compliant oscillator (3.6) decrease the spring energy I_{spring} of the mechanical system. However, in general nonlinear system, note that this result do not always provide the minimum of the spring energy.

3.5.3 An interpretation using Hamiltonian

Next, we consider a dynamic behavior of the compliant oscillator (3.6) with a mass.

The model is shown in Fig. 3.14. Assuming that the viscosity of the system is sufficiently small, the equation of motion for the mass m and its displacement x_2 is written as:

$$m\ddot{x}_2(t) = F(t), \tag{3.21}$$

where the positive displacements $x_1,\ x_2 > 0$ is defined as elongation direction of the spring. The spring force F is written as:

$$F(t) = -k(x_1(t) + x_2(t)), \tag{3.22}$$

where the positive force $F > 0$ is defined as a force pushing the slider.

The following theorem suggests that the dynamics of the compliant oscillator (3.6) may be interpreted as a closed-loop controller that make the system to down the slope of a potential of Hamiltonian.

Theorem 1 Let us consider the system (3.14),(3.21),(3.22),(3.16) that is illustrated in Fig. 3.14, the dynamics of the compliant oscillator (3.6) is written as:

$$\dot{\phi}(t) = \omega - \frac{\varepsilon}{a}\frac{\partial I_{\text{spring}}(t)}{\partial \phi(t)} - \frac{\varepsilon}{a}\frac{\partial I_{\text{mass}}(t)}{\partial \phi(t)} \tag{3.23}$$

$$= \omega - \frac{\varepsilon}{a}\frac{\partial \mathcal{H}(t)}{\partial \phi(t)}, \tag{3.24}$$

where $I_{\text{spring}} = \frac{1}{2}k(x_1(t) + x_2(t))^2$ is the spring energy, $I_{\text{mass}} = \frac{1}{2}m\dot{x}_2(t)^2$ is the inertial energy, $\mathcal{H} = I_{\text{spring}} + I_{\text{mass}}$ is the Hamiltonian for the spring and mass.

Proof 2 Substituting the slider displacement (3.14) and the equation of motion (3.21) for the motor dynamics (3.16), we get

$$\dot{\phi}(t) = \omega + \{\frac{\varepsilon}{a}F(t)\frac{\partial x_2(t)}{\partial \phi(t)} + \varepsilon F(t)\cos\phi(t))\} - \frac{\varepsilon}{a}F(t)\frac{\partial x_2(t)}{\partial \phi(t)} \tag{3.25}$$

$$= \omega + \frac{\varepsilon}{a}F(t)\{\frac{\partial(x_1(t) + x_2(t))}{\partial \phi(t)}\} - \frac{\varepsilon}{a}m\ddot{x}_2(t)\frac{\partial x_2(t)}{\partial \phi(t)}. \tag{3.26}$$

Deforming this equation and substituting the spring force (3.22), the motor dynamics is written as:

$$\dot{\phi}(t) = \omega + \frac{\varepsilon}{a}F(t)\frac{\partial(x_1(t) + x_2(t))}{\partial \phi(t)} \tag{3.27}$$

$$- \frac{\varepsilon}{a}m\frac{\partial \dot{x}_2(t)}{\partial t}\frac{\partial x_2(t)}{\partial \dot{x}_2(t)}\frac{\partial \dot{x}_2(t)}{\partial \phi(t)} \tag{3.28}$$

$$= \omega + \frac{\varepsilon}{a}F(t)\frac{\partial(x_1(t) + x_2(t))}{\partial \phi(t)} - \frac{\varepsilon}{a}m\dot{x}_2(t)\frac{\partial \dot{x}_2(t)}{\partial \phi(t)} \tag{3.29}$$

$$= \omega - \frac{\varepsilon}{a}\frac{\partial I_{\text{spring}}(t)}{\partial \phi(t)} - \frac{\varepsilon}{a}\frac{\partial I_{\text{mass}}(t)}{\partial \phi(t)} \tag{3.30}$$

$$= \omega - \frac{\varepsilon}{a}\frac{\partial \mathcal{H}(t)}{\partial \phi(t)}. \tag{3.31}$$

where $I_{\text{spring}} = \frac{1}{2}k(x_1(t) + x_2(t))^2$ is the spring energy, $I_{\text{mass}} = \frac{1}{2}m\dot{x}_2(t)^2$ is the inertial energy, $\mathcal{H} = I_{\text{spring}} + I_{\text{mass}}$ is the Hamiltonian for the spring and mass. □

From the second term of the right side of (3.17), momentary, the motor phase ϕ might be adjusted as the system down the slope of a potential of spring energy I_{spring}. This result may be interpreted that the compliant oscillator (3.6) decrease the Hamiltonian $\mathcal{H}$ of the mechanical system.

Note that this result is able to apply to the coupled spring–mass system with N masses and springs. When the spring–mass is the coupled system, the motor dynamics is written as follows:

$$\dot{\phi}(t) = \omega - \frac{\varepsilon}{a}\sum_{i=1}^{N}\frac{\partial I_{\text{spring,i}}(t)}{\partial \phi(t)} - \frac{\varepsilon}{a}\sum_{i=1}^{N}\frac{\partial I_{\text{mass,i}}(t)}{\partial \phi(t)}. \tag{3.32}$$

Moreover, the result is able to apply to the case when the system has the viscosity.

Theorem 2 When we consider the viscosity in the system (3.14),(3.21),(3.22),(3.16) that is illustrated in Fig. 3.14, the motor dynamics is illustrated as:

$$\dot{\phi}(t) = \omega - \frac{\varepsilon}{a}\frac{\partial \mathcal{H}(t)}{\partial \phi(t)} - \frac{\varepsilon}{a}\frac{\partial \mathcal{D}(t)}{\partial \dot{\phi}(t)}. \tag{3.33}$$

where $\mathcal{H} = I_{\text{spring}} + I_{\text{mass}}$ is the Hamiltonian for the spring and mass, $\mathcal{D} = \frac{1}{2}c(\dot{x}_2(t))^2$ is the dissipation energy.

Proof 3 Substituting the slider displacement (3.14) and the equation of motion (3.21) for the motor dynamics (3.16), we get

$$\begin{aligned}\dot{\phi}(t) =& \omega + \{\frac{\varepsilon}{a}F(t)\frac{\partial x_2(t)}{\partial \phi(t)} + \varepsilon F(t)\cos\phi(t))\} \\ &- \frac{\varepsilon}{a}\{F(t)\frac{\partial x_2(t)}{\partial \phi(t)} - c\dot{x}_2\frac{\partial x_2(t)}{\partial \phi(t)}\} - \frac{\varepsilon}{a}c\dot{x}_2\frac{\partial x_2(t)}{\partial \phi(t)},\end{aligned} \tag{3.34}$$

and each terms cen be deformed as follows:

$$\begin{aligned}\dot{\phi}(t) =& \omega - \frac{\varepsilon}{a}\frac{\partial I_{\text{spring}}(t)}{\partial \phi(t)} - \frac{\varepsilon}{a}\frac{\partial I_{\text{mass}}(t)}{\partial \phi(t)} - \frac{\varepsilon}{a}\frac{\partial \mathcal{D}(t)}{\partial \dot{\phi}(t)} \\ =& \omega - \frac{\varepsilon}{a}\frac{\partial \mathcal{H}(t)}{\partial \phi(t)} - \frac{\varepsilon}{a}\frac{\partial \mathcal{D}(t)}{\partial \dot{\phi}(t)}.\end{aligned} \tag{3.35}$$

where $I_{\text{spring}} = \frac{1}{2}k(x_1(t) + x_2(t))^2$ is the spring energy, $I_{\text{mass}} = \frac{1}{2}m\dot{x}_2(t)^2$ is the inertial energy, $\mathcal{H} = I_{\text{spring}} + I_{\text{mass}}$ is the Hamiltonian for the spring and mass, $\mathcal{D} = \frac{1}{2}c(\dot{x}_2(t))^2$ is the dissipation energy.

This result suggests that the electrical passivity of the low-torque DC motor may also decrease the dissipation energy, momentary.

3.6 Supplementary Lemmas

Following theoretical results are the supplementary lemmas for the system Fig. 3.14.

3.6.1 Relation between the energy consumption and motor speed

The following lemma shows that the energy consumption P is proportional to the difference between the rotational velocity $\dot{\phi}(t)$ and no-load velocity ω of the motor.

Lemma 2 Let us consider the system Fig. 3.14, then the relation between the energy consumption P and rotational speed of the motor $\dot{\phi}$ is

$$P(t) = -\frac{a}{\varepsilon}\omega(\dot{\phi}(t) - \omega). \tag{3.36}$$

Proof 4 The energy consumption P of the system Fig. 3.14 is written as:

$$P(t) = i(t)V(t) \tag{3.37}$$

$$= (\frac{R}{K_M^2}\tau(t)^2 - \dot{\phi}(t)\tau(t)). \tag{3.38}$$

where the first term of the right side is the dissipation energy per unit time, and the second term is the work per unit time of the motor. Substituting Eq. (3.4) related to the torque τ and the motor dynamics (3.16), we obtain following relationship

$$P(t) = \varepsilon(aF(t)\cos\phi(t))^2 - \dot{\phi}(t)aF(t)\cos\phi(t) \tag{3.39}$$

$$= -\omega aF(t)\cos\phi(t) \tag{3.40}$$

$$= -\frac{a}{\varepsilon}\omega(\dot{\phi}(t) - \omega). \tag{3.41}$$

From this equation, the relation between the energy consumption P and rotational speed of the motor $\dot{\phi}$. □

3.6.2 Solution of the motor phase

In the following lemma, we attempted to derive the motor phase assuming a periodicity of the solution.

Lemma 3 Assuming that Fig. 3.14 has a steady limit cycle with a period of $\frac{2\pi}{\omega}$, then the dynamics of motor phase $\phi(t)$ is written as:

$$\dot{\phi}(t) = \omega - \varepsilon ak(1 + \frac{1}{mk\omega^2 - 1})\sin\phi(t)\cos\phi(t). \tag{3.42}$$

The motor phase $\phi(t)$ is derived as:

$$\phi(t) = \tag{3.43}$$

$$\tan^{-1}\left(\frac{X - \sqrt{4\omega^2 - X^2}\tan(\frac{1}{2}(C\sqrt{4\omega^2 - X^2} - t\sqrt{4\omega^2 - X^2}))}{2\omega}\right). \tag{3.44}$$

where $X = \varepsilon ka(1 + \frac{1}{mk\omega^2 - 1})$ and C are constants.

Proof 5 Assuming that Fig. 3.14 has a steady limit cycle with a period of $\frac{2\pi}{\omega}$, then a periodic steady state x_2 is

$$x_2(t) = E_0 + \sum_{k=1}^{\infty}(E_{ck}\cos k\omega t + E_{sk}\sin k\omega t), \tag{3.45}$$

where $E_0,\ E_{ck},\ E_{sk}$ are constants. Note that the bias term is to be $E_0 = 0$ by the symmetry of the limit cycle. Using (3.45), from the equation of motion (3.21), the following relation is derived

$$x_2(t) = (\frac{1}{mk\omega^2 - 1})x_1(t). \tag{3.46}$$

Substituting (3.46) for the spring force (3.15), and using the equation for x_1 (3.14), we get

$$F(t) = -ak(1 + \frac{1}{mk\omega^2 - 1})\sin\phi(t), \tag{3.47}$$

Finally, substituting (3.47) for the motor dynamics (3.16), we get an equation for the motor phase $\phi(t)$

$$\dot{\phi}(t) = \omega - \varepsilon ak(1 + \frac{1}{mk\omega^2 - 1})\sin\phi(t)\cos\phi(t). \tag{3.48}$$

Deriving (3.48), the motor phase $\phi(t)$ is explicitly derived as:

$$\phi(t) = \tan^{-1}\left(\frac{X - \sqrt{4\omega^2 - X^2}\tan(\frac{1}{2}(C\sqrt{4\omega^2 - X^2} - t\sqrt{4\omega^2 - X^2}))}{2\omega}\right). \tag{3.49}$$

where $X = \varepsilon ka(1 + \frac{1}{mk\omega^2 - 1})$ and C are constants. □

3.7 Discussion

This chapter shows some experiments, simulations, and theoretical analysis for the fundamental systems: the spring–mass system and planar quadruped model.

First, we introduced a decentralized control module, called the compliant oscillator module. The experiments in Fig. 3.4 showed that the system converged to the resonance modes as the input voltage was increased. The effect of the electrical passivity was verified in Fig. 3.5, and the motor speed decreased when the motor pulled the mass and increased when the motor was pulled by the mass. From this results, the compliant oscillator module adjusted its own phases when there existed an unmatching force to its own motion, and as a result, the motion converged to the resonance modes.

In the simulations, a robustness against the initial phase difference and the convergence property with different motor parameter were reported. In Fig. 3.7, the system converged to one of the resonance modes from any of the initial states.

In the theoretical analysis of the compliant oscillator module, an interpretation for the function of low-torque DC motor is obtained. The function of electrical passivity of the low-torque DC motor is interpreted as an implicit controller to down the slope of the Hamiltonian

potential for the system and dissipation energy, momentary. In other words, the compliant oscillator may decrease the Hamiltonian and energy loss of the mechanical system. However, note that this result do not always provide the minimum of the energy potential in general nonlinear system.

3.8 Future Works

This control method based on the compliant oscillator module has some clear advantages that differs from the conventional decentralized controllers.

3.8.1 Model-less control for terrible nonlinear and uncertain systems

The compliant oscillator module generates resonance modes of a system and synchronize themselves using only the local force feedback. In other words, each module needs no global information of the mechanical system, thus the module may generate resonance modes of uncertain or unpredictable systems. As a result, if the body and environment dynamics is changed by some troubles, the electrical passivity of motors instantly adjusts the motions and adapt to these uncertainty. A future work of this research is to apply this method to other systems with a complex morphology, terrible nonlinearity, and uncertainly, such as the field robots and soft robots.

3.8.2 Thousand actuators in a robot

In a general implementation of this type of decentralized controller, each control module needs a sensor (to obtain x and $\dot{x}$), a microprocessor, and some peripheral circuits (to calculate $\dot{\phi}$ and send signals to the motors). Additionally, such a system typically needs a certain precise and high-torque servo motor to achieve the target state (3.1), and thus, the robot designer needs a huge number of cost to implement these systems. Mass production of the decentralized control module had a limitation, and it was a bottleneck in the field of distributed cooperative control. However, this method significantly reduces the implementation cost of conventional decentralized controllers because the functions of the sensor, controller, and actuator are all provided by the low-cost DC motor. Therefore, this method has a potential to embed thousands of control modules (each module has the functions of sensors, actuators, and controllers) in one robot system, similar to animal muscles or neurons.

3.8.3 Fundamental basis for next generation robot design

The proposed control method is powerless and inaccurate, but can generates physically natural motion that suit for the robot body and environment. Although this method does not suit for static and heavy workload (e.g., position control or object manipulation), it will be a new approach for robot design by using this method as a fundamental basis of the robot motor control and adding just a little explicit controllers, such as the motor command from the brain, for the heavy workload tasks. To achieve such next-generation robot design, we have to investigate some known and unknown limitation of the method correctly and give a

design methodology to integrate the proposed "weak" controller and powerful controller.

Here, there are three known limitations, and the improvement for these disadvantages is also the future works.

1. The motor torque is low

   In a real system, an excessively low-torque motor would easily become stuck owing to some disturbances (e.g., friction). Moreover, this controller does not suit for static and heavy workload tasks (e.g., position control or object manipulation). Module design that generates sufficient forces at a proper timing for the static tasks is a future work.

2. The mechanism and theoretical conditions are not proved

   Although some figures and theorems suggested the mechanism and theoretical conditions for generating resonance modes, these are still not unclear, yet. Therefore, the limitation of the proposed method (applicability for a system with terrible nonlinearity or uncertainly) is also unclear.

3. Applicable range is unclear

   The proposed control method may be applicable to wide range of systems that has uncertainty. However, related to the above limitation, the applicable range and condition is still unclear: e.g., what kind of morphology, nonlinearity, and uncertainly is allowed?. The theoretical analysis and accumulation of case studies are the future work.

Part II

Reflex Chains Generate Motor Patterns

Chapter 4

Direct Force Feedback Model

4.1 From Brainless Walking to DFFB (Direct Force Feedback) Model

In Chapter 3, the result Fig. 3.8 showed that the low-torque motor adjusts its own phase when there exists a large force and mass displacement. Moreover in Fig. 3.9, when the motor consumes the electrical energy (when the motor torque do work), it functions as that the motor delays its own phase when there exists a large positive or negative spring force.

From these result, in this chapter, we attempt to extract the dominant dynamics in which the motor delays the phase when spring force $|N| > 0$ is applied. The proposed model with the extracted control strategy is called the *DFFB (Direct Force Feedback) model*.

4.2 DFFB (Direct Force Feedback) Model

This chapter introduces a simple controller by extracting the dominant dynamics in which the motor delays the phase when spring force $|N| > 0$ is applied.

Fig. 4.1 shows the overview of the proposed control module, called the DFFB model. The proposed controller is written as:

$$\dot{\phi}_i(t) = \omega - \varepsilon|N_i(t)|, \tag{4.1}$$

where $\phi_i(t)$ is the phase of the i th controller, $\omega > 0$ is the intrinsic angular velocity, $\varepsilon > 0$ is sensory gain, $N_i(t)$ is the internal force in the actuator. To prevent reverse rotation of the phase $\phi_i(t)$, we determine the sensory gain so as to satisfy a condition $\varepsilon > \omega/N_{\max}$ with an expected upper limit of the internal force $N_{\max}$. In this paper, the expected upper limit of the internal force $N_{\max}$ was estimated through trial and error.

Each linear actuator i is modeled as a spring–damper, thus the internal force in the actuator are given by

$$N_i(t) = -k_i(x_i(t) - L_i(t)) - c_i(\dot{x}_i(t) - \dot{L}_i(t)), \tag{4.2}$$

where $x_i(t)$ denote the actuator length, and k_i and c_i denote the viscoelastic constants. Each

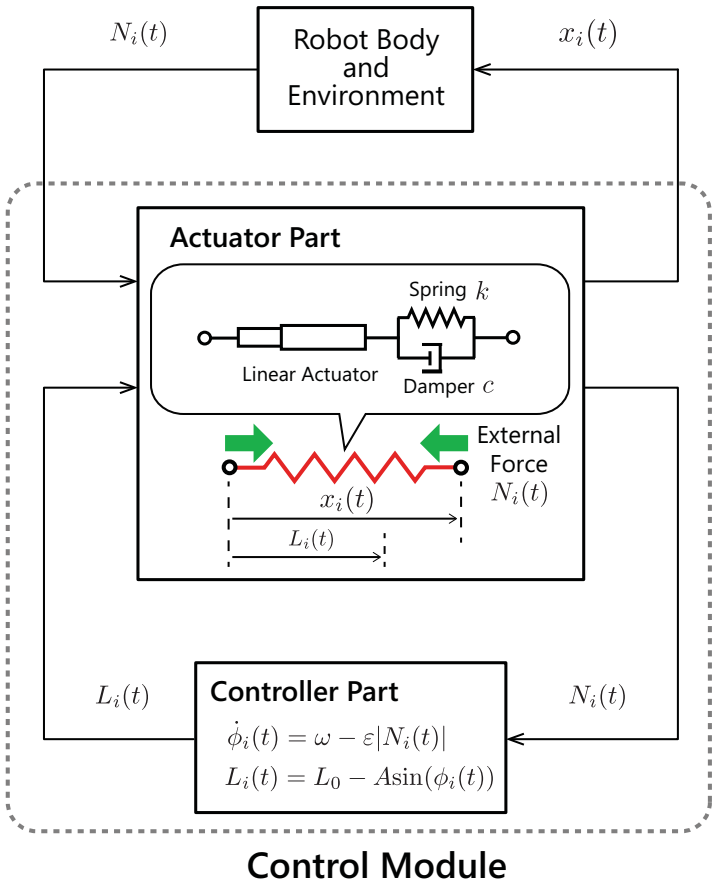

Fig. 4.1 Overview of the proposed control module, called the DFFB model. Each module is composed of an actuator part and a controller part. The actuator is modeled as a linear one with a spring–damper. When an external force is applied to the control module from the robot body and environment, the module detects internal force in the spring–damper, and it adjusts the natural length of the actuator part.

control module i drives the natural length $L_i(t)$ of the actuator

$$L_i(t) = L_0 - A\sin(\phi_i(t)). \tag{4.3}$$

Fig. 4.2 illustrates the dynamics of the proposed control module. In a constant frequency ω, when the controller does not detect forces $N_i(t) = 0$, it oscillates the body by driving the linear actuator. And when the module detects a non-zero internal force $N_i(t) \neq 0$ in the spring–damper, the feedback term $-\varepsilon|N_i(t)|$ is activated, and it slows down the oscillation.

4.3 Spring–Mass Simulation

We conduct some simulations to investigate fundamental characteristics of the proposed control module.

The simulation setting is illustrated in Fig. 4.3. The system is composed by three masses and four spring–dampers, thus it has three vibration modes corresponds to each resonance

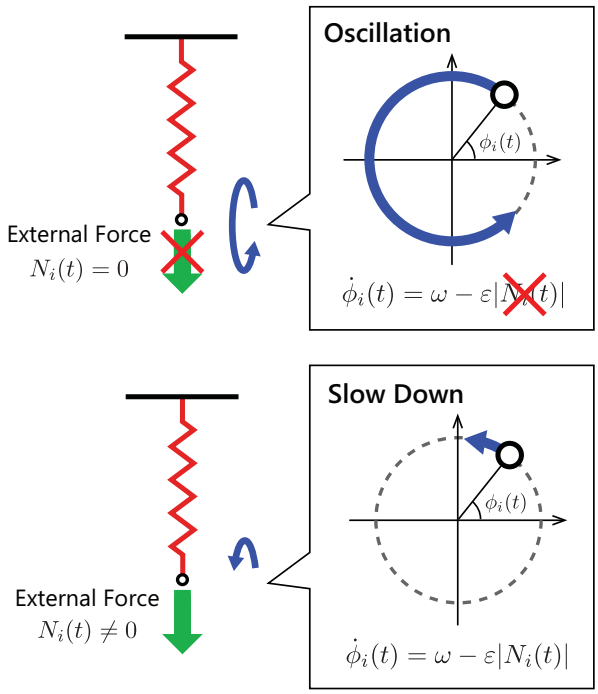

Fig. 4.2 Behavior of the proposed control module. When the module does not detect forces, in a constant frequency, it oscillates the body by driving the linear actuator. And when the module detects a non-zero internal force in the spring–damper, it slows down the oscillation.

frequency. In this simulation, we show an adaptability to changes in the vibration frequency and the body parameter. We compare the resonance frequencies the simulated and analytically derived ones.

4.3.1 Resonance Frequency Analysis

The resonance frequencies of the spring–mass system can be estimated analytically. We assume that the all spring constants, the natural length, and the mass weights are identical ($k_1 = k_2 = k_3 = k_4 = k$, $L_1 = L_2 = L_3 = L_4 = L_0$, $m_1 = m_2 = m_3 = m$), and the damper effect is sufficiently small. Let a new state $z_i(t) = x_i(t) - L_0$, then the model in Figure 4.3 is written as follows:

$$\begin{bmatrix} \ddot{z}_1(t) \\ \ddot{z}_2(t) \\ \ddot{z}_3(t) \end{bmatrix} = \begin{bmatrix} -2k/m & k/m & 0 \\ k/m & -2k/m & k/m \\ 0 & k/m & -2k/m \end{bmatrix} \begin{bmatrix} z_1(t) \\ z_2(t) \\ z_3(t) \end{bmatrix}. \tag{4.4}$$

By using eigenvalue analysis of the state matrix (4.4), the resonant frequencies of the mechanical dynamics $\omega_1 \leq \omega_2 \leq \omega_3$ can be calculated as:

$$\omega_1 = \sqrt{\frac{(2-\sqrt{2})k}{m}},\ \omega_2 = \sqrt{\frac{2k}{m}},\ \omega_3 = \sqrt{\frac{(2+\sqrt{2})k}{m}}. \tag{4.5}$$

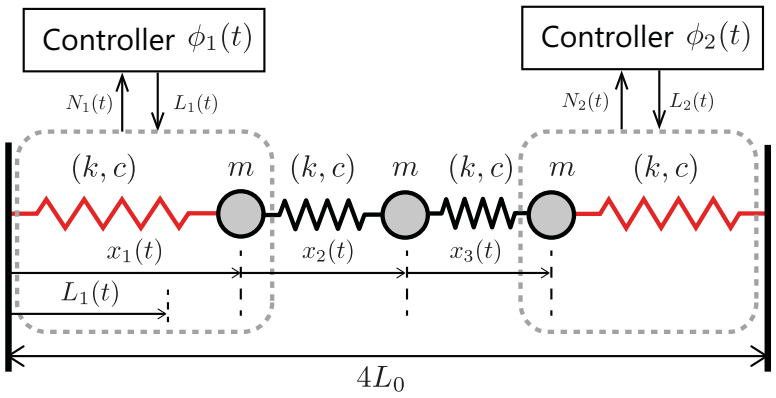

Fig. 4.3 Simulation setting of the spring–mass system. Two control modules are fixed on the wall on the left and right (red spring), and the springs that transmit the physical forces between the modules and masses (black spring).

4.3.2 Results

We conducted some simulations with three different spring constants $k = 1,\ 2$ N/m. In each parameters, simulations are performed iteratively by changing the initial phase difference $\phi_1(0) - \phi_2(0)$ and the intrinsic angular velocity ω rad/s. The control input is given by (4.1) and we set the following parameters for all spring–dampers and actuators identically:

$$\varepsilon = 2,\ c = 0.1 \text{ Ns/m},\ L_0 = 1 \text{ m},\ A = 0.1 \text{ m},\ m = 1 \text{ kg}. \tag{4.6}$$

We set the initial states of each controller

$$\phi_1(0) = 0 \text{ rad},\ \dot{\phi}_1(0) = 0,\ \dot{\phi}_2(0) = 0 \text{ rad/s}, \tag{4.7}$$

and change $\phi_2(0)$ in $[0,\ \pi]$ rad,and ω in $[0,\ 5]$ rad/s.

Fig. 4.4(a)(b) shows the simulation results with different spring constants $k = 1,\ 2$. The bullet color denotes the phase difference of converged solutions of two control modules. The blue bullets are the in-phase solutions, and the red bullets are the anti-phase solutions. The triangles at the top of graph indicates the resonance frequencies $\omega_1,\ \omega_2,\ \omega_3$ which is analytically derived. From these figures, the phase differences of converged solutions change as the intrinsic angular velocity ω increases. In Fig. 4.4(a) with $k = 1$, the first transition occurs at around $\omega = 1.2$, and the second is $\omega = 1.8$, and in Fig. 4.4(b) with $k = 2$, the first is $\omega = 1.8$, and the second is $\omega = 2.8$. Each solution converged to the resonance modes and achieves transitions between the modes as illustrated in the upper of Fig. 4.4(a)(b):

$$\text{1st Mode} \rightarrow \text{2nd Mode} \rightarrow \text{3rd Mode}. \tag{4.8}$$

4.3.3 Comparisons between analysis and simulation

Table. 4.1 shows the comparisons between the simulated and analytically derived resonance frequencies. From the tables, the three modes in Fig. 4.4(a)(b) were excited around the ana-

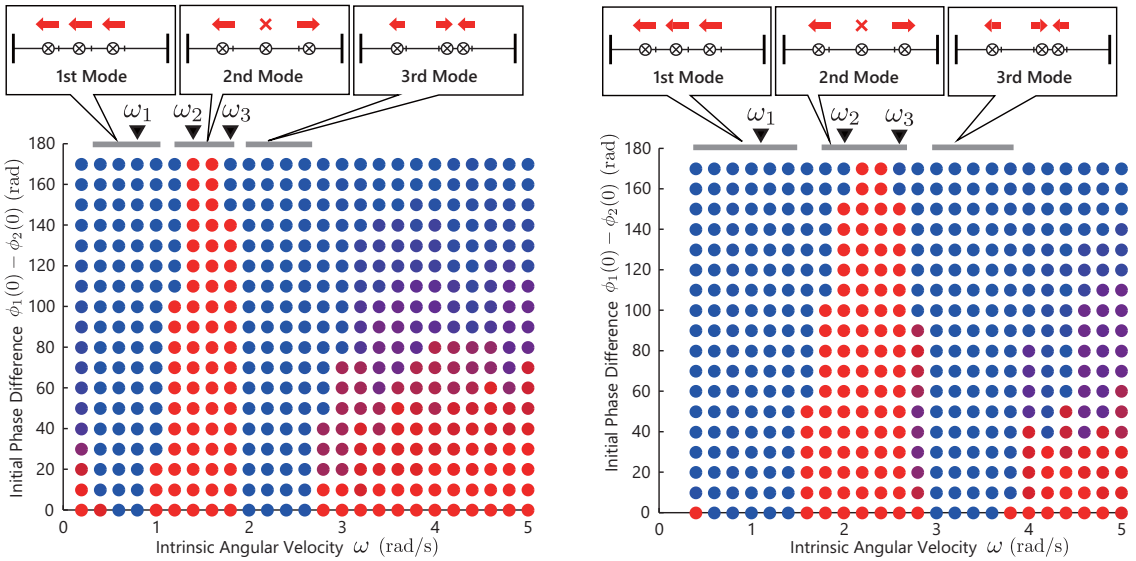

(a) $k = 1$ (b) $k = 2$

Fig. 4.4 Simulation result of the spring–mass system. The bullet color denotes the phase difference of the converged solutions of the two modules. The blue and red bullets shows the in-phase and anti-phase solutions. The triangles at the top of graph indicates the resonance frequencies $\omega_1,\ \omega_2,\ \omega_3$ which is analytically derived.

Table 4.1 Comparisons between the analysis and simulation

(a) $k = 1$

	1st mode	2nd mode	3rd mode
Analysis	$\omega_1 = 0.77$	$\omega_2 = 1.41$	$\omega_3 = 1.85$
Simulation	$\omega_1 = [0.6,\ 0.8]$	$\omega_2 = [1.4,\ 1.6]$	$\omega_3 = [2,\ 2.6]$

(b) $k = 2$

	1st Mode	2nd Mode	3rd Mode
Analysis	$\omega_1 = 1.08$	$\omega_2 = 2$	$\omega_3 = 2.61$
Simulation	$\omega_1 = [0.4,\ 1.4]$	$\omega_2 = [2.2,\ 2.4]$	$\omega_3 = [3,\ 3.6]$

lytically derived frequencies $\omega_1,\ \omega_2,\ \omega_3$. This result shows that the proposed module (4.1) automatically selects and generates a resonance mode which is most easily excited, because the module functions to adjust the phases when there exists an unmatching force.

However, in Fig. 4.4(a)(b), with very low or high frequencies, the solutions depend on the initial values due to the too small sensor values. With low frequencies, the internal forces for feedback were small due to the too slow movement of the masses. And with high frequencies, the internal forces were also small due to the low amplitude motion due to the gain characteristics of the mechanical system. Moreover, particularly in the 3rd mode in Table. 4.1(a)(b), the analytical and simulated results are with disagreement. It is assumed that these disagreement are due to the assumptions in the analysis.

4.4 Planar Quadruped Robot Simulation

This section shows some simulations with a planar quadruped robot model to evaluate the proposed controller.

The robot model is the simplified planar model for a quadruped robot [1], which has two known vibration mode. We show that the robot model with two proposed control modules can excites and selects these modes automatically.

4.4.1 Model formulation

The model of the quadruped robot is same as the model that was introduced in Chapter 3 Fig. 3.11.

Two modules are attached in the fore and hind legs as follows:

$$\dot{\phi}_{\mathrm{F}}(t) = \omega - \varepsilon|N_{\mathrm{F}}(t)|, \tag{4.9}$$

$$\dot{\phi}_{\mathrm{H}}(t) = \omega - \varepsilon|N_{\mathrm{H}}(t)|. \tag{4.10}$$

Each module drives the natural length of fore and hind springy legs $L_{\mathrm{F}}, L_{\mathrm{H}}$ as follows:

$$L_{\mathrm{F}}(t) = L_0 - A\sin(\phi_{\mathrm{F}}(t)), \tag{4.11}$$

$$L_{\mathrm{H}}(t) = L_0 - A\sin(\phi_{\mathrm{H}}(t)). \tag{4.12}$$

4.4.2 Resonance frequency analysis

In this section, we adopt a few assumptions for the resonant frequency analysis.

We assume that the robot feet are fixed on the ground, all of the natural lengths are equal $L_{\mathrm{F}} = L_{\mathrm{H}} = L_0$, and the damper effect is sufficiently small. Assuming that the infinitesimal angle θ, a linearized model around the origin is as:

$$\begin{aligned} N_{\mathrm{F}}(t) \simeq -k((x_g(t) + \frac{d}{2}\theta(t)) - L_0),\ N_{\mathrm{H}}(t) \simeq -k((x_g(t) - \frac{d}{2}\theta(t)) - L_0) \\ \cos\theta(t) \simeq 1,\ \sin\theta(t) \simeq \theta(t). \end{aligned} \tag{4.13}$$

Let a new state $z_g(t) = x_g(t) - L_0$, the model in Figure 4.3 is formulated as follows:

$$M\ddot{z}_g(t) = -k(z_g(t) + \frac{d}{2}\theta(t)) - k(z_g(t) - \frac{d}{2}\theta(t)) - Mg \tag{4.14}$$

$$I\ddot{\theta}(t) = \frac{d}{2}\{k(z_g(t) + \frac{d}{2}\theta(t)) - k(z_g(t) - \frac{d}{2}\theta(t))\}. \tag{4.15}$$

By using eigenvalue analysis of the state matrix (4.14) (4.15), the resonant frequencies can be calculated as

$$\omega_1 = \sqrt{\frac{2k}{M}},\ \omega_2 = \sqrt{\frac{kd^2}{2I}} = \sqrt{\frac{6k}{M}} \tag{4.16}$$

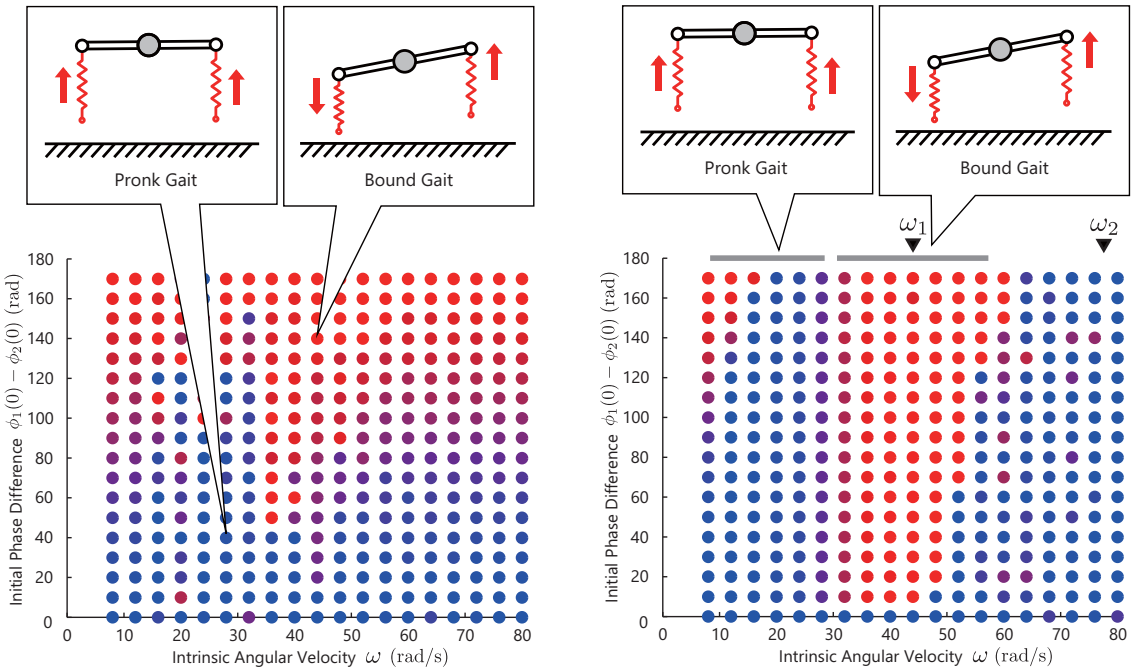

(a) with the spting–damper force feedback $\dot{\phi}_*(t) = \omega - \varepsilon|N_*(t)|$

(a) with only the spting force feedback $\dot{\phi}_*(t) = \omega - \varepsilon|k_*(x_*(t) - L_*(t))|$

Fig. 4.5 Simulation result of the quadruped robot model. The bullet color denotes the phase difference of the converged solutions of the two modules. The blue and red bullets shows the in-phase and anti-phase solutions. The triangles at the top of graph indicates the resonance frequencies ω_1, ω_2 which is analytically derived.

where we assume that the rigid spine is a uniform rod, thus $I = \frac{1}{12}Md^2$. The frequency ω_1 corresponds to the pronk gait, the fore and hind legs are in an in-phase manner, and the ω_2 is the bound gait, the fore and hind legs are in an anti-phase manner.

4.4.3 Results

Finally, we show the simulations with the quadruped robot model.

The simulations are performed iteratively by changing the initial phase difference $\phi_1(0) - \phi_2(0)$ and the intrinsic angular velocity ω. We set the following parameters identical for all spring–dampers and actuators:

$$\varepsilon = 2,\ k = 500\ \mathrm{N/m},\ c = 10\ \mathrm{Ns/m} \tag{4.17}$$

$$L_0 = 0.1\ \mathrm{m},\ A = 0.3\ \mathrm{m},\ d = 0.2\ \mathrm{m}, M = 0.5\ \mathrm{kg}. \tag{4.18}$$

We set the initial states of each controller

$$\phi_1(0) = 0\ \mathrm{rad},\ \dot{\phi}_1(0) = 0,\ \dot{\phi}_2(0) = 0\ \mathrm{rad/s}, \tag{4.19}$$

and change $\phi_2(0)$ in $[0,\ \pi]$ rad, ω in $[0,\ 80]$ rad/s.

Fig. 4.5(a) shows the simulation result. Similar to the above simulations, the color of sphere denotes the phase difference of converged solutions of two modules. The blue sphere

Table 4.2 Comparisons between the analysis and simulation

	1st mode	2nd mode
Analysis	$\omega_1 = 44.7$	$\omega_2 = 77.5$
Simulation	$\omega_1 = [20,\ 24]$	$\omega_2 = [36,\ 44]$

denotes the solutions that the two legs are in an in-phase manner, and the red sphere are the solutions in an anti-phase manner. The triangles at the top of graph indicates the resonance frequencies ω_1, ω_2 that is analytically derived. Each solution converged to the resonance modes as illustrated in the upper figure. In these figures, clearly, the phase differences of converged solutions depend on the initial values.

This result means that the resulting phase difference is sensitive to the initial values (not to the choice of the parameter ω). Now, let us consider selecting the motion pattern by choosing the parameter ω and make it insensitive to the initial values. For this purpose, we modify the control module in the next subsection.

4.4.4 Results with modified controller

Based on above failure, we apply a modification to the modules. In this modification, we alter the sensory information (the spring–damper force in (4.10)) to the spring force as follows:

$$\dot{\phi}_*(t) = \omega - \varepsilon|k_*(x_*(t) - L_*(t))|. \tag{4.20}$$

Although this modification is discovered in chance, some evidence in conventional researches are agree with this result, as written later.

Fig. 4.5(b) shows the result with the modified module. In these figures, the phase differences of converged solutions change as the intrinsic angular velocity ω increases. From the upper figure, the in-phase gait is generated in $\omega = [0,\ 28]$, and the anti-phase is generated in $\omega = [32,\ 50]$. In other words, at around $\omega = 30$, there is the following gait transition occurs as:

$$\text{Pronking} \rightarrow \text{Bounding}. \tag{4.21}$$

Table. 4.2 shows the comparison between the resonance frequencies, which is analytically derived, and the excited frequencies in the simulations. From the table, there is large disagreements between the analytical and simulated frequencies: the simulated one is almost half of the analytical one. These disagreements were due to the modeling error from the assumption that the feet of the robot model are fixed on the ground: the flight phase were not considered in the analysis. A similar disagreement were also reported in [78].

4.4.5 Discussion

By comparing these two results Fig. 4.5(a)(b), in the quadruped robot model (a nonlinear system with the switching between the swing and stance state), the spring force feedback is effective than the spring–damper force feedback for the steady gait generation. Although this modification is discovered in chance, some evidence in conventional researches are agree

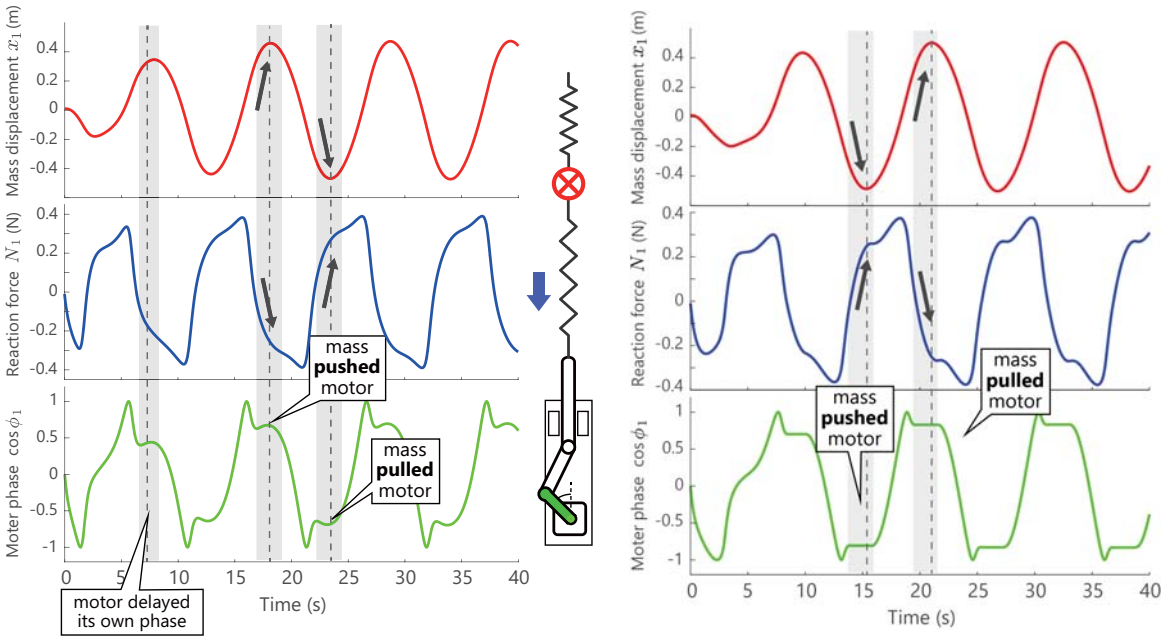

(a) Compliant oscillator model (Fig. 3.8) (b) DFFB model

Fig. 4.6 Comparison between the time response of the compliant oscillator model and DFFB model. The figure shows the phase of motor1, mass1, and the spring force between them in a very low-torque motor with $\varepsilon = 10$. The time responses with two models are similar each other.

with this result. In biology, it is well known that the receptor called the muscle spindle, which contributes the stretch reflex in animals, have two feedback pathway: one sends an information of the muscle displacement, and the other one sends the muscle velocity [84]. A research [85] shows that the sensitivity of the muscle displacement is mainly activated while periodic motions in a walking and running cat. In contrast, the receptor for the muscle velocity is deactivated while the periodic motions.

The major advantages of this module is the simplicity. The control strategy is quite simple: just delays the phase when there exists an unmatching force $|N| > 0$ to the body motions. Compared with a recent controller [47], the proposal (4.1) does not use any information of current phase ϕ_i or function form $\cos(*)$ that designed considering the body structure. This advantage simplifies controller design, e.g., when we design a system with this controller, no need to consider the detailed model of the whole body dynamics.

4.5 Comparison between Motor Model and DFFB Model

Finally, we compare the time responses between the compliant oscillator model (original), which is proposed in Chapter 3, and the DFFB model, which is proposed in this chapter.

Fig. 4.6 (a)(b) shows the time response of the compliant oscillator model and DFFB model. The figure shows the phase of motor1, mass1, and the spring force. The parameters are the same as the simulation Fig. 3.9. From the figure, both the compliant oscillator model and DFFB model delays the phase when spring force $|N| > 0$ is applied, and these response is

similar each other.

This result shows that despite the simplicity of the strategy, the proposed DFFB model reproduced the dominant dynamics of the compliant oscillator model.

Chapter 5

Physiological Model using Stretch Reflex

5.1 From DFFB Model to Physiological Model

In Chapter 4, we extracted the dominant dynamics in which the motor delays the phase when spring force $|N| > 0$ is applied. The extracted control strategy, called the DFFB model, shows some similar features to the compliant oscillator model that can excites and selects the resonant modes adaptively and automatically. Moreover, from Fig. 4.6, the time responses of both two models (the compliant oscillator model and DFFB model) are similar to each other. This result shows that despite the simplicity of the strategy, the proposed DFFB model reproduced the dominant dynamics of the compliant oscillator model.

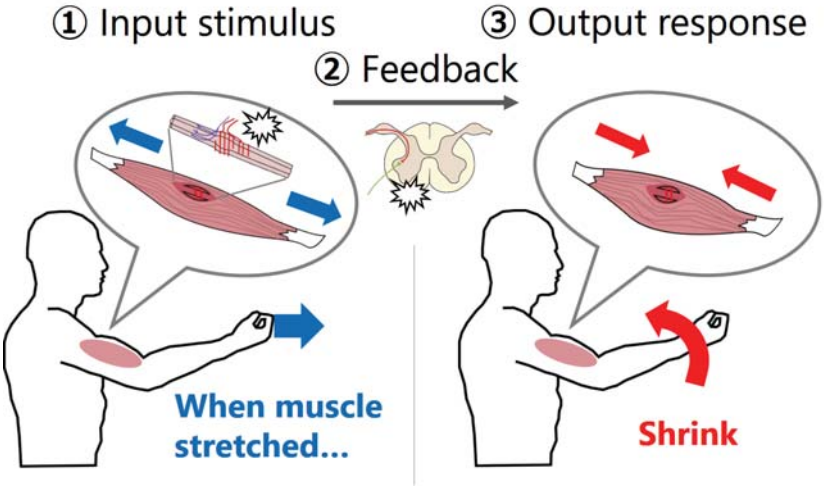

Fig. 5.1 When an animal muscle receives a force from the body or outside world, the stretch reflex functions to maintain its current muscle length.

The other aspect of the DFFB model is a rough model of the stretch reflex strategy of actual animals (Fig. 5.1). When an animal muscle receives a force from the body or outside world, the stretch reflex functions to maintain its current muscle length. As with the stretch reflex,

the DFFB model also maintains the current length of the linear actuator by delaying the oscillation speed when the module detects the reaction force. The results in Fig. 4.5(a)(b) provide a few suggestion for understanding the source of motor patterns of animals. First, the results suggest that the physical interaction of the local stretch reflex strategy is effective to generate the motor patterns as resonance modes. The strategy generating resonance modes might be an advantageous for animals to generate the large amplitude motions and survive in nature with limited resources. Second, for generating the resonance modes in the quadruped model, the muscle displacement information is more important than the muscle velocity information.

The results in the above chapters suggest a hypothesis that the local stretch reflex in animals contributes the motor pattern generation by exploiting the physical interaction through the body dynamics. To verify this hypothesis, in this chapter, we introduce a simple physiological model of the stretch reflex pathways in animals.

5.2 Overview, and Revisit the Issue

5.2.1 Overview

This chapter introduces a simple model as a simple configulation of the motor control system in animals. This model denotes a primitive local controller in animals, called the stretch reflex. Each model is composed of one muscle and one motor neuron, thus each of these has only identical and simple function. Here, a notable point is that the model has no explicit inter-muscular neural connection, but it has physical connection through body dynamics. Surprisingly, despite having no inter-muscular neural interaction (electrically isolated from the other models), each model synchronize themselves using the physical interaction through the body dynamics. Although many studies have focused on the animal reflex [86, 87, 88], the remarkable points of this model is the absence of inter-muscular neural connection and its simplicity (remind, Fig. 1.6). The extremely simple configulation for the animal reflex system provides a sufficient condition for generating the motor patterns.

In this chapter, first, we present the formulation of the stretch reflex model, and a fundamental step response is demonstrated. Second, to investigate the property of the reflex model, we conducted theoretical analysis and simulations. To prove some fundamental property, we present the theoretical analysis for a single muscle model and an antagonistic muscle pair. Additionally, we conduct some simulations with different three types of models: a single muscle model, one link limb model with antagonistic muscle pair, and two link limb model with multiple muscles.

5.2.2 The way to address the issue

As introduced in the first chapter (Chapter 1), to discuss the major issue of this thesis “what is the source of motor patterns?”, we introduce following two terms: the *“rhythm generation”* that provides the temporal rhythmicity, and the *“ pattern formation”* that adjust the waveform of the body motions. For the rhythm generation, we introduce two candidates, called the *self-excitation* and *forced-excitation* method. In the self-excitation method, we exploit the

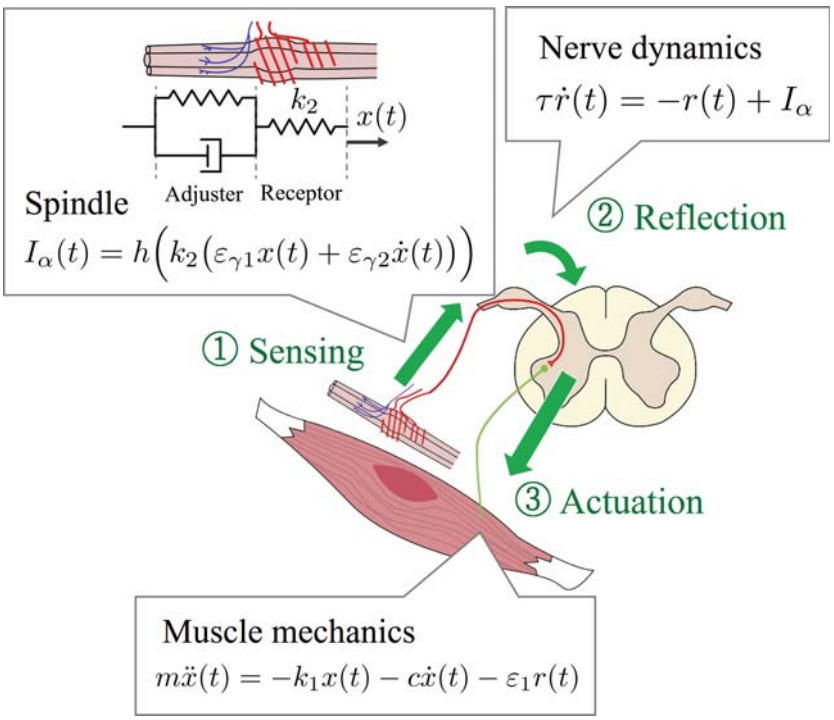

Fig. 5.2 Overview of stretch reflex model. This model is composed of one muscle and one motor neuron.

dynamics intrinsic to the reflex model as a rhythm source. Thanks to the saturation in sensors, when we increase the sensor gain of the reflex model, the muscle generate a steady limit cycle. We exploit this limit cycle as a candidate of the source of animal rhythm. Next, in the forced-excitation method, we apply a periodic external force to the body structure. This method is equivalent to a function in animals in which the motor control signal is generated by the CPGs and the upper central (e.g., the motor cortex).

For the pattern formation, we introduce the physical interaction of the local stretch reflex models. In the simulations, using whichever these two candidates of the rhythm source, the reflex model can automatically generate resonant modes without any explicit neural connection between the models. Moreover, the model adjusts these motor patterns adaptively to changes in the parameters of the body structure.

From these results, I will conclude that a candidate of the source of pattern formation is in the body dynamics, because the physical interaction between the extremely reflex controllers has a function to adjust the waveform of the body motions.

5.3 Overview of the Stretch Reflex Model

In this section, we present the formulation of a stretch reflex model as a simple configuration of the motor controller in animals.

Fig. 5.2 shows an overview of the stretch reflex model, which is composed of two parts: the muscle mechanics and nerve dynamics. The muscle mechanics are expressed by a simplified equation of motion for muscle displacement. The nerve dynamics describe the reflex action

through a motor neuron, which senses and reacts to the muscle displacement and velocity.

The proposed model is written as follows:

$$m\ddot{x}(t) = -k_1 x(t) - c\dot{x}(t) - \varepsilon_1 r(t) \tag{5.1}$$

$$\tau\dot{r}(t) = -r(t) + h\Big(k_2(\varepsilon_{\gamma 1} x(t) + \varepsilon_{\gamma 2}\dot{x}(t))\Big), \tag{5.2}$$

where Eq. (5.1), (5.2) expresses the muscle mechanics and nerve dynamics. States $x(t)$ and $r(t)$ represent the muscle displacement and nerve activity. k_1 and c denote the viscoelastic constants of the muscle mechanics, and k_2 is the sensor gain of the muscle spindle, which is an organ in the animal muscle corresponding to a sensor. τ is the time constant, and $\varepsilon_1,\ \varepsilon_{\gamma 1},\ \varepsilon_{\gamma 2}$ are the control and sensor gains. The sensor gains $\varepsilon_{\gamma 1},\ \varepsilon_{\gamma 2}$ are the sensitivity of the muscle displacement and velocity, which is adjusted by the upper central [89]. As will be discussed below, we can control the limit cycle generation (called, self-excitation, in following sections) by adjusting the sensor gain $\varepsilon_{\gamma 1},\ \varepsilon_{\gamma 2}$. The saturation function $h(*)$ with parameter a is defined as follows:

$$h(*) = \begin{cases} a \cdot \mathrm{sgn}(*) & (|*| > a) \\ * & (|*| \leq a) \end{cases}. \tag{5.3}$$

5.4 Modeling of Stretch Reflex System

The proposed model (5.1), (5.2) is based on the stretch reflex system in animals and consists of the following four elements:

$$I_a(t) = h\Big(k_2(\varepsilon_{\gamma 1} x(t) + \varepsilon_{\gamma 2}\dot{x}(t))\Big) \tag{5.4}$$

$$\tau\dot{r}(t) = -r(t) + I_a(t) \tag{5.5}$$

$$f_a(t) = \varepsilon_1 r(t) \tag{5.6}$$

$$m\ddot{x}(t) = -k_1 x(t) - c\dot{x}(t) - f_a(t). \tag{5.7}$$

Each element model represents the muscle spindle (5.4), the motor neuron (5.5), end effector (5.6), and muscle with body inertia (5.7). In this section, we present the details of the element models.

5.4.1 Muscle spindle

Muscles have mainly two types of sensors, called the muscle spindle and the golgi tendon organ. These receptor are connected to the α motor neuron in the spinal cord through the sensory nerve fibers, which are called the Ia, II, and Ib fibers [89]. Among these, in this thesis, we focus on the muscle spindle that is closely related to the local feedback control in a single muscle.

The muscle spindle has a structure wherein the sensory part and the actuator part are connected in series. The sensory part has a function that provides feedback regarding the muscle length and velocity, and the sensory value is sent to the α motor neuron through the Ia and II

fibers. The muscle spindle has individual sensors the static bag fibers and dynamic bag fibers. The static bag detects both the muscle length and velocity, and the dynamic bag detects only the velocity. The actuator part adjusts the sensitivity of the muscle spindle by signals from the upper central through the γ motor neuron in the spinal cord [89]. The γ motor neuron has two types of pathways, namely, the static γ efferent and dynamic γ efferent [84]. These efferents adjust the sensitivity of the static and dynamic bag fibers in the spindle, respectively. A previous research [85] has shown that the sensitivity of the static bag fibers is mainly activated while cat walking and running.

Considering that the sensory part is modeled as an elastic element [90], we obtain the activity of the $I_a(t)$ fibers as follows:

$$I_a(t) = h(I'_a(t)) = h\Big(k_2(\varepsilon_{\gamma 1} x(t) + \varepsilon_{\gamma 2} \dot{x}(t))\Big), \tag{5.8}$$

where $x(t)$ and k_2 denote the muscle displacement and sensor gain of the sensory part. For simplicity, we assume that the muscle displacement $x(t)$ is same as that of the entire muscle. We added the saturation h of the receptor defined by (5.3), and $\varepsilon_{\gamma 1}$, $\varepsilon_{\gamma 2}$ are the sensitivity of the muscle displacement and velocity adjusted by the upper central through the γ motor neuron.

5.4.2 Nerve dynamics

Neurons have characteristics that outputs a spike when the membrane potential reaches a certain threshold, and thereafter the potential begins to fade. A popular neuron model [91] describes the dynamics of nerve activity $r(t)$ for the α motor neuron and is written by the following differential equation:

$$\tau \dot{r}(t) = -r(t) + \sigma(t), \tag{5.9}$$

where the parameter $\sigma(t)$ denotes the sum of the input signals applied to the α motor neuron. Additionally, we considered $\sigma(t)$ as the fiber activity ($\sigma = I_a(t)$).

5.4.3 Muscle mechanics

The end effector in the muscles is driven by receiving signals from the α motor neuron. Although Hogan [92] has proposed a bilinear model for the relationship between the neuron activity $r(t)$ and the muscle actuation force $f_a(t)$, we assume that these have a proportional relationship as follows:

$$f_a(t) = \varepsilon_1 r(t), \tag{5.10}$$

where ε_1 is the control gain.

The physical mechanics of the muscles are non-linear and frequently modeled using the Hill type model [93]. In this study, for simplicity, we employed a second-order model [94] and considered the muscle property as a linear viscoelastic element with a body inertia[*1].

$$m\ddot{x}(t) = -k_1 x(t) - c\dot{x}(t) - f_a(t). \tag{5.11}$$

[*1] This model is equivalent to the Hill type model without a series elastic element

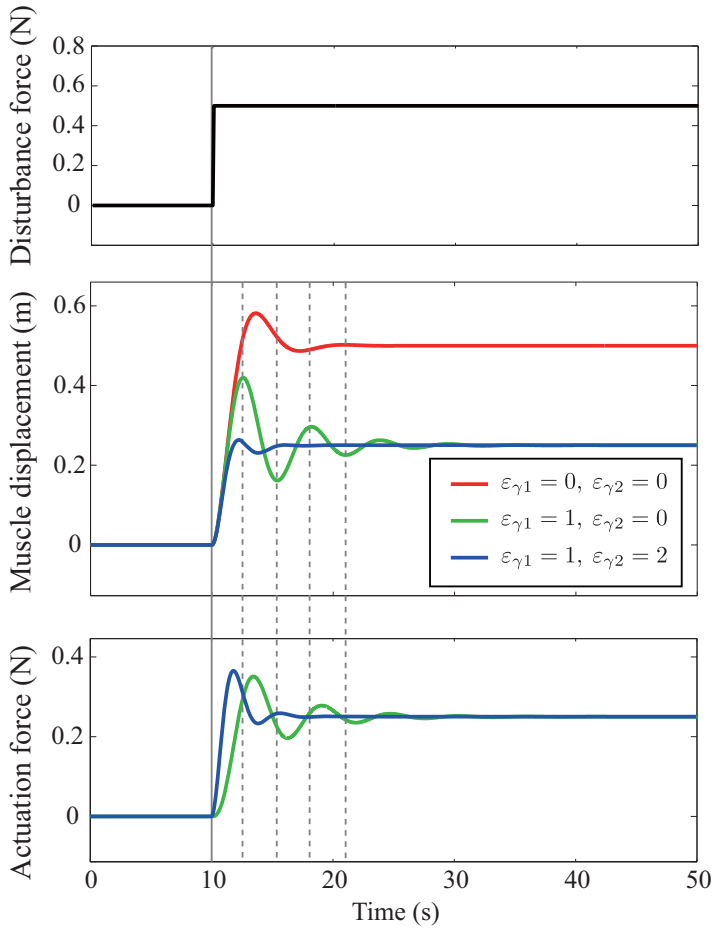

Fig. 5.3 Time response of single muscle to external force disturbance. The top figure shows the stepwise disturbance force, the middle is the muscle displacements with different sensor gains, and the bottom is the corresponding actuation force $\varepsilon_1 r(t)$ of the muscle with the feedback.

Using these approach as we mentioned, we obtain the entire reflex model (5.1), (5.2) by summarizing the element models (5.4)–(5.7).

5.4.4 Step response of single muscle

First, we demonstrate the step response of the single muscle in Fig. 5.2. The parameters, gains, and initial states are as follows:

$$k_1 = 1,\ k_2 = 1\ \mathrm{N/m},\ m = 1\ \mathrm{kg},\ c = 1\ \mathrm{sN/m},\ \varepsilon_1 = 1,\ \tau = 1,\ a = 1 \tag{5.12}$$

$$x(0) = 0\ \mathrm{m},\ \dot{x}(0) = 0\ \mathrm{m/s},\ r(0) = 0,\ \dot{r}(0) = 0, \tag{5.13}$$

and the sensor gain of the muscle displacement and velocity are changed in $(\varepsilon_{\gamma 1},\ \varepsilon_{\gamma 2}) = (0,\ 0),\ (1,\ 0),\ (1,\ 2)$.

Fig. 5.3 shows the time response of the single muscle. In this simulation, we applied a stepwise disturbance force of 0.5 N to the mass of the single muscle. The top figure shows

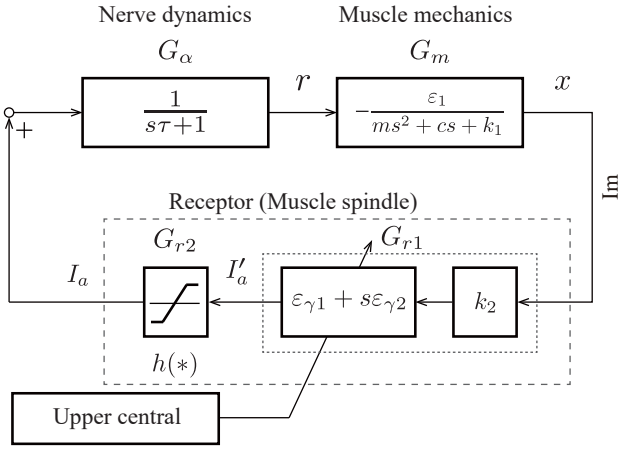

Fig. 5.4 Block diagram of single muscle.

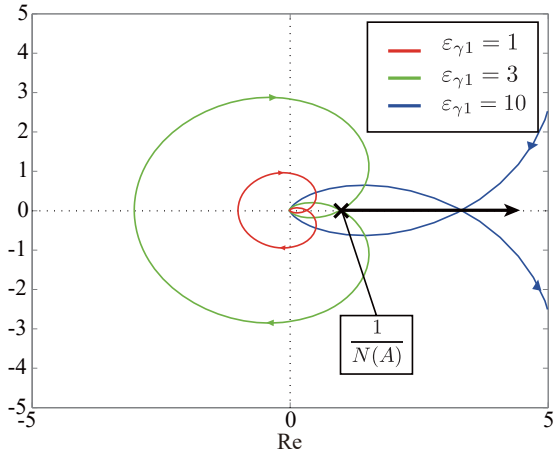

Fig. 5.5 Nyquist diagram of $G_\alpha G_m G_{r1}$ without the muscle velocity information $\varepsilon_{\gamma 2} = 0$.

the stepwise disturbance force, the middle is the muscle displacements with different sensory gains, and the bottom is the corresponding muscle force with the feedback. In the simulation with $(\varepsilon_{\gamma 1},\ \varepsilon_{\gamma 2}) = (1,\ 0),\ (1,\ 2)$ (green and blue lines), it can be seen that the generated actuation force $\varepsilon_1 r(t)$ cancels the displacement caused by the disturbance force. Moreover in the simulation with the muscle velocity information $(\varepsilon_{\gamma 1},\ \varepsilon_{\gamma 2}) = (1,\ 2)$ (blue line), the oscillation in the transient response was suppressed. This result with a small sensory gain suggests that the stretch reflex model reproduces the well-known reflex action in animals, and particularly, the muscle velocity information plays a role to stabilize the muscle response.

In the following sections, we present the characteristics of the proposed model from the viewpoint of control theory.

5.5 Theoretical Analysis of Single Muscle

5.5.1 Stability analysis of single muscle

Fig. 5.4 shows a block diagram of the muscle mechanics and nerve dynamics (5.1), (5.2), where G_m denotes the muscle mechanics (5.1) and nerve dynamics (5.2) consisting of two sub-models: a receptor and a motor neuron; G_{r1} and G_{r2} denote the linear and non-linear part of the receptor; G_α denotes the motor neuron. The transfer functions of each linear part $G_{r1},\ G_\alpha,\ G_m$ are expressed as follows:

$$G_{r1} = k_2(\varepsilon_{\gamma 1} + \varepsilon_{\gamma 2} s),\ G_\alpha = \frac{1}{\tau s + 1},\ G_m = -\frac{\varepsilon_1}{ms^2 + cs + k_1}. \tag{5.14}$$

Thus, we obtain the open loop transfer function of the linear part between I_a and I'_a, as follows:

$$G_\alpha G_m G_{r1} = -\frac{k_2\varepsilon_1(\varepsilon_{\gamma 1} + \varepsilon_{\gamma 2} s)}{\tau m s^3 + (\tau c + m)s^2 + (\tau k_1 + c)s + k_1}. \tag{5.15}$$

The following theorem shows a stability condition for the stretch reflex model.

Theorem 3 Let us consider the system (5.1), (5.2) without the muscle velocity information $\varepsilon_{\gamma 2} = 0$. If and only if the physical constants m, k_1, k_2, c, and the parameters $\tau, \varepsilon_1, \varepsilon_{\gamma 1}$ satisfy the following condition:

$$\frac{k_2 \varepsilon_1 \varepsilon_{\gamma 1} \tau m}{c(\tau^2 k_1 + \tau c + m)} < 1, \tag{5.16}$$

then, the equilibrium is asymptotically stable. Therefore, if the parameters satisfy the following condition:

$$\frac{k_2 \varepsilon_1 \varepsilon_{\gamma 1} \tau m}{c(\tau^2 k_1 + \tau c + m)} \geq 1, \tag{5.17}$$

then, a steady limit cycle is generated, and its frequency is calculated as follows:

$$\sqrt{\frac{\tau k_1 + c}{\tau m}}. \tag{5.18}$$

Proof 6 In this proof, we employ the describing function method. When we input a sine wave with an amplitude A in the saturation block G_{r2}, the describing function $N(A)$ of the saturation can be expressed as follows:

$$N(A) = \frac{2}{\pi}(\sin^{-1}\frac{a}{A} + \frac{a}{A}\sqrt{1 - \frac{a^2}{A^2}}), \tag{5.19}$$

where a is the parameter of the saturation function $h(*)$. The amplitude locus of the saturation is illustrated in Fig. 5.5 as a half line on the real axis starting from point $1/N(A) = 1$.

When we replace the non-linear part G_{r2} with $N(A)$ in Fig. 5.4, we obtain the following condition from the characteristic equation $1 - N(A)G_\alpha G_m G_{r1}(s) = 0$:

$$G_\alpha G_m G_{r1}(j\omega) = \frac{1}{N(A)}. \tag{5.20}$$

If there is a limit cycle with an angular velocity ω and amplitude A, these parameters must satisfy Eq. (5.20). Additionally, if there is no solution for Eq. (5.20), then, there is no limit cycle. Because the intersection point of the Nyquist locus of the system and the real axis is expressed as follows:

$$\frac{k_2 \varepsilon_1 \varepsilon_{\gamma 1} \tau m}{c(\tau^2 k_1 + \tau c + m)}, \tag{5.21}$$

and if and only if the parameters satisfy the following condition:

$$\frac{k_2 \varepsilon_1 \varepsilon_{\gamma 1} \tau m}{c(\tau^2 k_1 + \tau c + m)} < \frac{1}{N(A)} = 1, \tag{5.22}$$

then, the equilibrium is asymptotically stable. Moreover, if the parameters satisfy the following condition:

$$\frac{k_2 \varepsilon_1 \varepsilon_{\gamma 1} \tau m}{c(\tau^2 k_1 + \tau c + m)} \geq \frac{1}{N(A)} = 1, \tag{5.23}$$

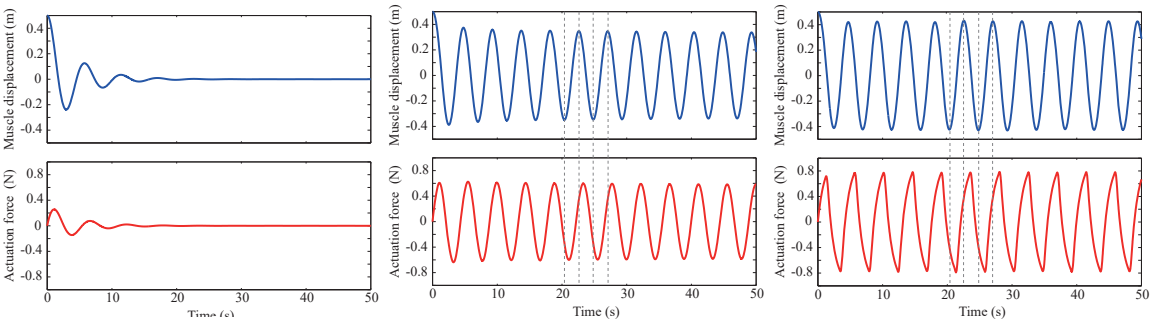

$\varepsilon_{\gamma 1} = 1$ $\varepsilon_{\gamma 1} = 3$ $\varepsilon_{\gamma 1} = 10$

Fig. 5.6 Simulation results of single muscle by changing the sensory gain $\varepsilon_{\gamma 1} \in \{1,\ 3,\ 10\}$. The top figures show the muscle displacement, while the bottom figures show the actuation force that is proportional to the nerve activity.

then, the system converges to a steady limit cycle because the amplitude locus and Nyquist locus have an intersection point. The frequency of the limit cycle is calculated as the angular frequency when the Nyquist locus is at the intersection point $\omega = \sqrt{\frac{\tau k_1 + c}{\tau m}}$. □

Theorem 1 states that the stretch reflex model is stable with a small sensor gain $\varepsilon_{\gamma 1}$. Moreover it can generate a steady limit cycle with a large $\varepsilon_{\gamma 1}$, and that the frequency of the limit cycle is around the resonance frequency of the physical muscle. In this thesis, we call it as a self-excitation phenomenon. A previous study [95] has reported the phenomenon of periodic motion generation that occurs by applying a continuous (non-periodic) electrical stimulation. This phenomenon is similar to the limit cycle generation in the following simulations, wherein it occurs by adjusting the sensor gain $\varepsilon_{\gamma 1}$.

5.5.2 Self-excitation of single muscle

We conducted a simulation to confirm the existence of the steady limit cycle in the single muscle by adjusting the sensor gain $\varepsilon_{\gamma 1}$. From Theorem 1, the stretch reflex model can generate a steady limit cycle with a large sensory gain $\varepsilon_{\gamma 1}$. Here, we exploit this function as a candidate of the rhythm source (we call this method as the self-excitation).

The parameters and gains of each muscle were the same as those in the previous simulation, except for $\varepsilon_{\gamma 1},\ \varepsilon_{\gamma 2}$. We chose the sensory gain of $\varepsilon_{\gamma 1} = 1,\ 3,\ 10$, and there is no muscle velocity feedback $\varepsilon_{\gamma 2} = 0$. The initial states are as follows:

$$x(0) = 0.5 \text{ m},\ \dot{x}(0) = 0 \text{ m/s},\ r(0) = 0,\ \dot{r}(0) = 0. \tag{5.24}$$

Fig. 5.6 shows the time response during $\varepsilon_{\gamma 1} \in \{1,\ 3,\ 10\}$ without the muscle velocity information $\varepsilon_{\gamma 2} = 0$. The top figures show the muscle displacement, and the bottom figures show the actuation force that is proportional to the nerve activity. As can be seen in the figures, the solution converged to the origin at $\varepsilon_{\gamma 1} = 1$, and a limit cycle was generated at $\varepsilon_{\gamma 1} = 3,\ 10$. This result is in good agreement with Theorem 1, and we can observe a bifurcation in Fig. 5.5 because the Nyquist locus and the amplitude locus intersect at $\varepsilon_{\gamma 1} \geq 3$. Moreover, by focusing on the case at $\varepsilon_{\gamma 1} = 10$, when the muscle receives a large force

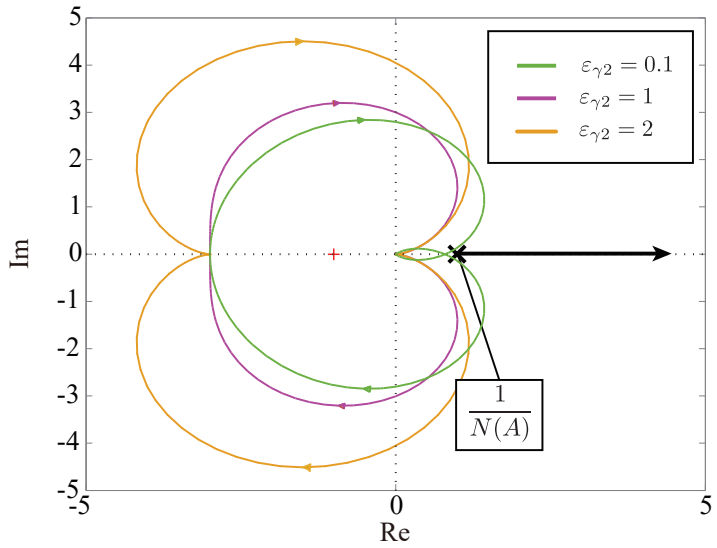

Fig. 5.7 Nyquist diagram of $G_\alpha G_m G_{r1}$ with $\varepsilon_{\gamma 1} = 3$ and different velocity gains.

from the mass, the nerve maintains a large activation and converts kinetic energy to elastic energy. In contrast, when the muscle force begins to decrease, the sign of the actuation force is quickly inverted and the muscle converts elastic energy to kinetic energy.

Next, we show that the muscle velocity feedback suppresses the limit cycle. Fig. 5.7 shows the nyquist diagram of $G_\alpha G_m G_{r1}$ with $\varepsilon_{\gamma 1} = 3$ and different velocity gains $\varepsilon_{\gamma 2} = (0.1,\ 1,\ 2)$. The half line on the real axis starting from point $1/N(A) = 1$ is the amplitude locus of the saturation. As can be seen in the figure, the muscle velocity information prevent to intersect the Nyquist locus and the amplitude locus.

5.6 Antagonistic Muscle Pair

5.6.1 Stability analysis of antagonistic muscles

Our aim in this chapter is to clarify the contribution of the physical inter-muscular interaction through the body dynamics. To analyze the fundamental physical interaction of muscles, in this section, we introduce an antagonistic muscle pair. Fig. 5.8 shows the antagonistic muscle pair. This system is composed of a flexor–extensor muscle pair, and a pendulum. The muscles actuate the rotary joint of the pendulum through a pulley that is fixed on the wall. As mentioned in the introduction, the muscles have no inter-muscular neural interaction (two models are electrically isolated from each other). This model represents the case wherein the inhibitory inter-neurons between the flexor and extensor muscles are disconnected (see the right figure in Fig. 1.8).

The mechanics of the antagonistic muscle are expressed as follows:

$$\bar{m}\ddot{x}(t) = -(k_{1,F} + k_{1,E})x(t) - (c_F + c_E)\dot{x}(t) - \varepsilon_1(r_F(t) - r_E(t)), \tag{5.25}$$

where $\bar{m} = 2I/d$ is a constant determined by the limb inertia $I = ml^2/4$ and the pulley diameter d; $k_{1,F}$, $k_{1,E}$ and c_F, c_E are the viscoelastic constants of each muscle. We defined

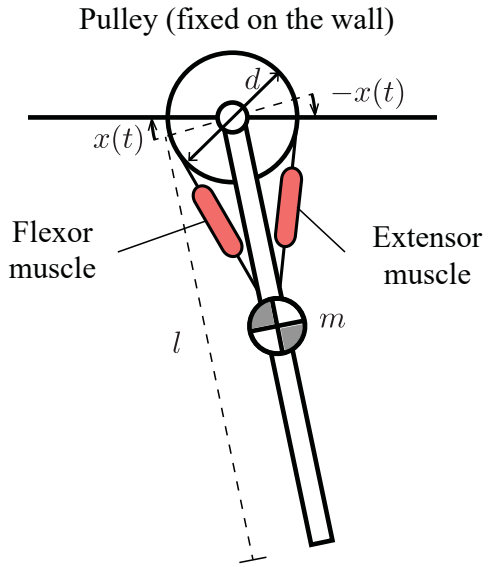

Fig. 5.8 Antagonistic muscle pair. This system is composed of a flexor–extensor muscle pair, and a pendulum. The muscles actuate the rotary joint of the pendulum through a pulley that is fixed on the wall.

the muscle displacements as the state of $x(t) = x_F(t) = -x_E(t)$ under the assumption of $x_F(t) = -x_E(t)$. Additionally, we assumed no slacking for the muscles. Here, x_F and x_E correspond to the displacements of the flexor and extensor muscles.

The nerve dynamics of the flexor and extensor muscles are expressed as follows:

$$\begin{aligned}\tau \dot{r_F}(t) &= -r_F(t) + h\Big(k_{2,F}(\varepsilon_{\gamma 1}x(t) + \varepsilon_{\gamma 2}\dot{x}(t))\Big)\\ \tau \dot{r_E}(t) &= -r_E(t) - h\Big(k_{2,E}(\varepsilon_{\gamma 1}x(t) + \varepsilon_{\gamma 2}\dot{x}(t))\Big),\end{aligned} \tag{5.26}$$

where $k_{2,F},\ k_{2,E}$ is the sensory gain of the muscle spindles in the flexor and extensor muscles. The sign difference of the second term is caused by the definition of muscle coordinates.

The following theorem shows a stability condition for the antagonistic muscle pair.

Theorem 4 Let us consider the system (5.25), (5.26), and assume that $k_2 = k_{2,F} = k_{2,E}$. If and only if the constants $\bar{m},\ k_{1,F},\ k_{1,E},\ k_2,\ c_F,\ c_E$ and the parameters $\tau, \varepsilon_1,\ \varepsilon_{\gamma 1}$ satisfy the following condition:

$$\frac{2k_2\varepsilon_1\varepsilon_{\gamma 1}\tau\bar{m}}{(c_F + c_E)(\tau^2(k_{1,F} + k_{1,E}) + \tau(c_F + c_E) + \bar{m})} < 1, \tag{5.27}$$

then, the equilibrium is asymptotically stable. Therefore, if the parameters satisfy the following condition:

$$\frac{2k_2\varepsilon_1\varepsilon_{\gamma 1}\tau\bar{m}}{(c_F + c_E)(\tau^2(k_{1,F} + k_{1,E}) + \tau(c_F + c_E) + \bar{m})} \geq 1, \tag{5.28}$$

then, a steady limit cycle is generated and its frequency is calculated as follows:

$$\sqrt{\frac{\tau(k_{1,F} + k_{1,E}) + (c_F + c_E)}{\tau\bar{m}}}. \tag{5.29}$$

Proof 7 Let $\bar{r}(t) = r_F(t) - r_E(t)$, $\bar{k}_1 = k_{1,F} + k_{1,E}$, and $\bar{c} = c_F + c_E$; then, the system (5.25), (5.26) is rewritten as follows:

$$\bar{m}\ddot{x}(t) = -\bar{k}_1 x(t) - \bar{c}\dot{x}(t) - \varepsilon_1 \bar{r}(t) \tag{5.30}$$

$$\tau\dot{\bar{r}}(t) = -\bar{r}(t) + 2h\Big(k_{2,E}(\varepsilon_{\gamma 1} x(t) + \varepsilon_{\gamma 2}\dot{x}(t))\Big), \tag{5.31}$$

Similar to (5.14), the transfer functions of each linear part G_{r1}, G_α, G_m are expressed as follows:

$$G_{r1} = \varepsilon_{\gamma 1} k_2,\ G_\alpha = \frac{2}{\tau s + 1},\ G_m = -\frac{\varepsilon_1}{\bar{m}s^2 + \bar{c}s + \bar{k}_1}. \tag{5.32}$$

Let $\bar{k}_2 = 2k_2$, then we obtain the open loop transfer function of the linear part with the same form as (5.15):

$$G_\alpha G_m G_{r1} = -\frac{\bar{k}_2 \varepsilon_1 \varepsilon_{\gamma 1}}{\tau\bar{m}s^3 + (\tau\bar{c} + \bar{m})s^2 + (\tau\bar{k}_1 + \bar{c})s + \bar{k}_1}. \tag{5.33}$$

Therefore, the result is proven in the same manner as Theorem 1. □

5.6.2 Synchronization of antagonistic muscles

Next, we prove the synchronization of the antagonistic muscle pair.

Theorem 5 Let us consider the system (5.25), (5.26), and assume that $k_2 = k_{2,F} = k_{2,E}$. The activities of the antagonistic muscle pair synchronize and satisfy the following condition:

$$r_F(t) = -r_E(t). \tag{5.34}$$

Proof 8 We consider the behavior of the sum of nerve activities for $\tilde{r} = r_F + r_E$. From Eq. (5.26), the sum of two nerve dynamics is expressed as follows:

$$\tau\dot{\tilde{r}}(t) = -\tilde{r}(t). \tag{5.35}$$

This system is clearly exponentially stable, and the sum of nerve activities $\tilde{r} = r_F + r_E$ converges to the origin. □

Theorems 3 state that the antagonistic muscle pair synchronize individually into an anti-phase mode, wherein each muscle shrinks alternately without losses by cancelling the actuation force. Moreover, this synchronization is achieved independently of the form of function $h(*)$ and the body properties. In other words, even if there is the muscle velocity feedback, and if the muscles have asymmetries or errors, the antagonistic muscle pair can generate lossless motions.

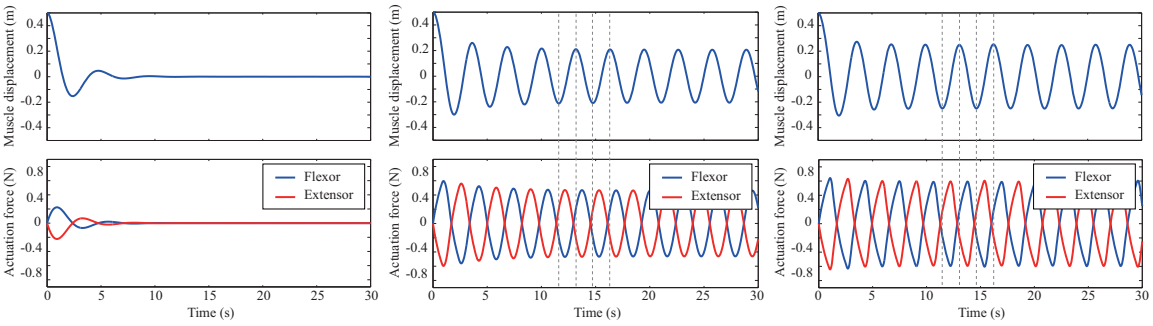

$\varepsilon_{\gamma 1} = 1$ $\varepsilon_{\gamma 1} = 5$ $\varepsilon_{\gamma 1} = 10$

Fig. 5.9 Simulation results of self-excited antagonistic muscle pair obtained by changing the sensory gain $\varepsilon_{\gamma 1} \in \{1,\ 5,\ 10\}$. The top figures show the muscle displacement, and the bottom is the actuation force that is proportional to the nerve activity.

5.6.3 Self-excitation of antagonistic muscle pair

Next, we present the simulation result obtained by the self-excited antagonistic muscle pair without inter-muscular interaction. In this simulation, we do not consider gravity, and choose the parameters, gains, and initial states as follows:

$$k_{1,F} = k_{1,E} = 1,\ k_2 = 1\ \text{N/m},\ m = 1\ \text{kg},\ c_F = c_E = 1\ \text{sN/m} \tag{5.36}$$

$$\varepsilon_1 = 1,\ \varepsilon_{\gamma 2} = 0,\ \tau = 1,\ a = 1,\ l = 1\ \text{m},\ d = 0.5\ \text{m} \tag{5.37}$$

$$x(0) = 0.5\ \text{m},\ \dot{x}(0) = 0\ \text{m/s},\ r_F(0) = r_E(0) = 0,\ \dot{r}_F(0) = \dot{r}_E(0) = 0, \tag{5.38}$$

Additionally, we choose the sensory gain $\varepsilon_{\gamma 1} \in 1,\ 5,\ 10$.

Fig. 5.9 shows the time response with $\varepsilon_{\gamma 1} \in 1,\ 5,\ 10$. The top figures show the muscle displacement, and the bottom is the actuation force that is proportional to the nerve activity. In the figures, the solution converged to the origin at $\varepsilon_{\gamma 1} = 1$, and a limit cycle was generated at $\varepsilon_{\gamma 1} = 5,\ 10$. These results are in agreement with the Theorems 2 and 3 because the limit cycle exists if $\varepsilon_{\gamma 1} \geq 5$, and the actuation forces proportional to nerve activity converge to $r_F(t) = -r_E(t)$.

5.7 Limb with Multiple Muscles

5.7.1 Limb model

Finally, we present the simulation results of the limb model with multiple muscles.

Fig. 5.10 shows the simulation setting of the limb model with multiple muscles. This system consists of two flexor–extensor muscle pairs, and two link limbs. The muscles actuate the limb joint through pulleys that are fixed on the wall and lower limb. The limb model is expressed as follows:

$$M(\theta(t))\ddot{\theta}(t) + H(\theta(t), \dot{\theta}(t)) + D\dot{\theta}(t) = \frac{d}{2}F(t), \tag{5.39}$$

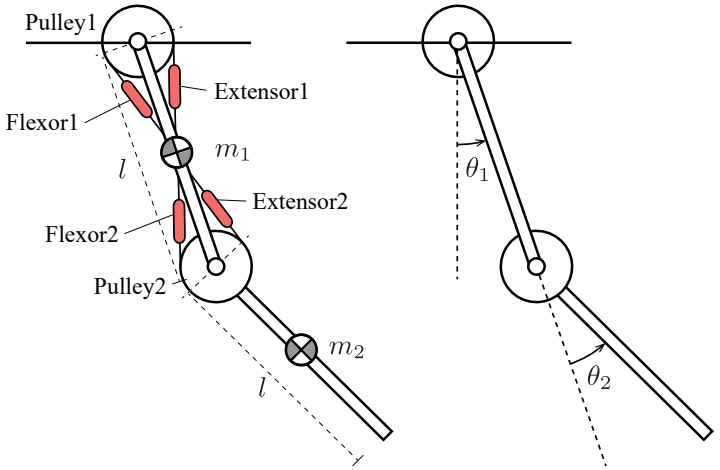

Fig. 5.10 Limb model with multiple muscles. This system is composed of two flexor–extensor muscle pair and two link limbs. The muscles actuate the limb joints through the pulleys fixed on the wall and the lower limb.

and each element is expressed as follows:

$$M(\theta(t)) = \begin{bmatrix} l_1(m_1 + 4m_2) & l_2\cos(\theta_1(t) - \theta_2(t)) \\ l_1\cos(\theta_1(t) - \theta_2(t)) & l_2 \end{bmatrix} \tag{5.40}$$

$$H(\theta(t), \dot{\theta}(t)) = \begin{bmatrix} l_2 m_1 \sin(\theta_1(t) - \theta_2(t))\dot{\theta}_2(t)^2 + 2g(m_1 + 2m_2)\sin\theta_1(t) \\ -l_1\sin(\theta_1(t) - \theta_2(t))\dot{\theta}_1(t)^2 + 2g\sin\theta_2(t) \end{bmatrix} \tag{5.41}$$

$$D = \begin{bmatrix} c_{\theta 1} & 0 \\ 0 & c_{\theta 2} \end{bmatrix} \tag{5.42}$$

$$F(t) = -\begin{bmatrix} k_{1,F1} + k_{1,E1} & 0 \\ 0 & k_{1,F2} + k_{1,E2} \end{bmatrix} x(t) - \begin{bmatrix} c_{F1} + c_{E1} & 0 \\ 0 & c_{F2} + c_{E2} \end{bmatrix} \dot{x}(t) - \begin{bmatrix} \varepsilon_1(r_{F1}(t) - r_{E1}(t)) \\ \varepsilon_1(r_{F2}(t) - r_{E2}(t)) \end{bmatrix}. \tag{5.43}$$

where $x(t) = [x_1(t),\ x_2(t)]^\top$ is the muscle displacement, the new state $\theta(t) = [\theta_1(t),\ \theta_2(t)]^\top$ denotes the angles of each rotary joint, each joint has viscous friction with constant $c_{\theta 1},\ c_{\theta 2}$. $F(t)$ is the muscle force, and r_{Fi} and r_{Ei} represent the activity of the flexor and extensor muscles for joint i, respectively.

5.7.2 Self-excitation of limb model

Next, we present the simulation result obtained by the self-excited limb model without an inter-muscular neural interaction.

The simulations were conducted iteratively by changing the initial phase difference $\theta_1(0) - \theta_2(0) \in [-30,\ 30]$ deg. Moreover, we changed the mass parameter $\bar{m} \in (0,\ 1]$ to show that the muscles can generate various periodic motions adaptively with different body parameters. The masses of the limb were determined from the mass parameter $\bar{m}$ as $m_1 = \bar{m},\ m_2 = 0.6\bar{m}$ kg. The initial phase and phase difference were set as $\theta_1(0) = 30$ deg, $\theta_1(0) - \theta_2(0) \in [-30,\ 30]$ deg, and the viscoelastic constants of all muscles were identical. In this simulation,

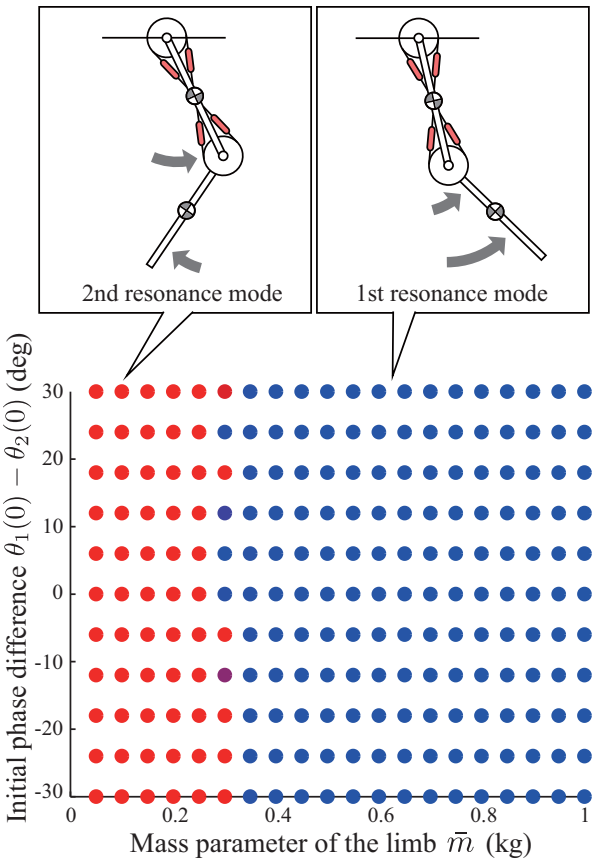

Fig. 5.11 Simulation results using the self-excited limb model by changing the initial phase difference $\theta_1(0) - \theta_2(0) \in [-30,\ 30]$deg and mass parameter $\bar{m} \in (0,\ 1]$. The blue bullet denotes that the two joints converged to a solution in an in-phase manner, and the red bullet denotes anti-phase manner. The top figures illustrate the converged solution.

we considered the gravity with constant g, and selected the other parameters, gains, and initial states, as follows:

$$k_{1,F1} = k_{1,E1} = k_{1,F2} = k_{1,E2} = k_2 = 100\ \mathrm{N/m} \tag{5.44}$$

$$c_F1 = c_E1 = c_F2 = c_E2 = 0.1,\ c_{\theta 1} = c_{\theta 2} = 1\ \mathrm{sN/m},\ \tau = 0.1,\ a = 1 \tag{5.45}$$

$$\varepsilon_1 = 10,\ \varepsilon_{\gamma 1} = 10,\ \varepsilon_{\gamma 2} = 0,\ l = 0.5\ \mathrm{m},\ d = 0.4\ \mathrm{m},\ g = 9.8\ \mathrm{s^2/m} \tag{5.46}$$

$$\dot{\theta}_1(0) = 0\ \mathrm{deg/s},\ r_F(0) = r_E(0) = 0,\ \dot{r}_F(0) = \dot{r}_E(0) = 0. \tag{5.47}$$

Fig. 5.11 presents the simulation results with different mass parameters $\bar{m} \in (0,\ 1]$. The bullet color denotes the phase difference of the converged solution of the two joint angles. The blue bullet denotes that the two joints converged to a solution in an in-phase manner, and the red bullet denotes an anti-phase manner. In these figures, the phase differences of the converged solution change as the mass parameter $\bar{m}$ increases. The transition is appeared at approximately $\bar{m} = 0.3$, and each solution converged to the resonance modes, as shown in the top figures. From Eq. (5.29) in Theorem 2, it is understood that the frequencies of the generated motions decrease as the body mass increases. Although the simulation setting

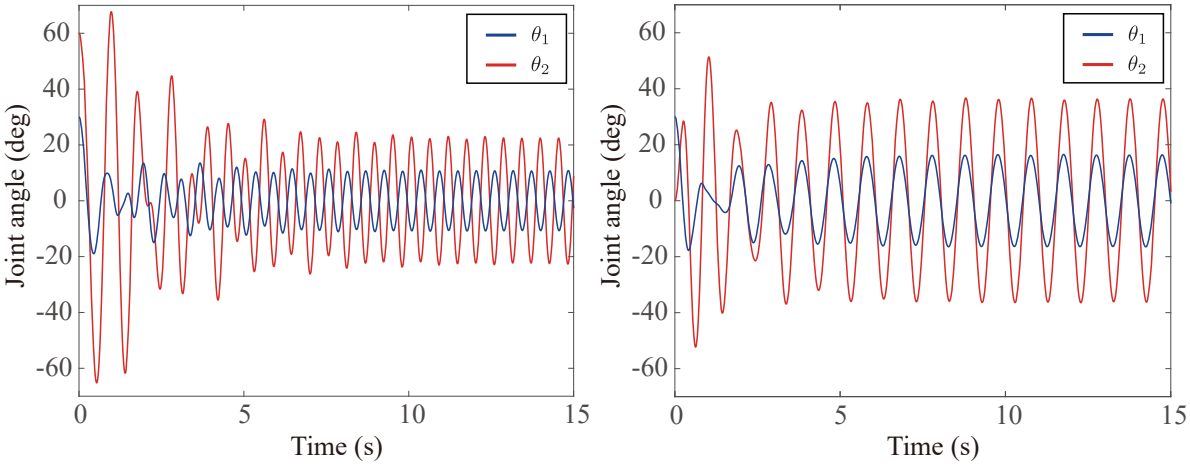

(a) $\theta_1(0) - \theta_2(0) = 30, \bar{m} = 0.2$ (b) $\theta_1(0) - \theta_2(0) = -30, \bar{m} = 0.4$

Fig. 5.12 Time response of limb angles θ_1 and θ_2 with initial phase difference $\theta_1(0) - \theta_2(0) = 30$. The left figure illustrates the limb angles θ_1 and θ_2 with the mass parameter $\bar{m} = 0.2$, and the right figure is the result with the mass parameter $\bar{m} = 0.4$.

were slightly different to those in Theorem 2, a similar tendency still existed. Therefore, as the mass parameter $\bar{m}$ increased, the transition from the 2nd mode to the 1st mode (higher to lower resonance frequency) occurred. The notable point of this result is that the self-excited muscles synchronized themselves and achieved an adaptive motion transition only by inter-muscular interaction through the body dynamics.

Fig. 5.12 (a)(b) shows the time response of the limb angles θ_1 and θ_2 in Fig. 5.11. We present the results with two initial phase difference $\theta_1(0) - \theta_2(0) = 30, \ -30$, and with two different mass parameters $\bar{m} = 0.2, \ 0.4$. The left figure (a) illustrates the result with the mass parameter $\bar{m} = 0.2$, and the right figure (b) is the result with the mass parameter $\bar{m} = 0.4$. In the figures, (a) the angles converged to the 2nd mode in an anti-phase manner and (b) to the 1st mode in an in-phase manner, respectively.

These results suggests that the limit cycles that is generated by the stretch reflex pathway in animals is possible to be a candidate of the rhythms source. Therefore, the local reflex strategy also contributes to the pattern formation by exploiting inter-muscular interaction through the physical body dynamics.

5.7.3 Forced excitation of limb model

Finally, we present the simulation result obtained by the force-excited limb model without inter-muscular interaction. The forced-excitation, in which we apply an periodic external force to the joint angles, is equivalent to a function in animals in which the motor control signal is generated by the other candidate of the rhythm source: the CPGs and the upper central. We aim to investigate the pattern formation ability of the synchronization using the body dynamics with the CPGs and the upper central.

The simulations were conducted iteratively by changing the initial phase difference $\theta_1(0) - \theta_2(0) \in [-30, \ 30]$ deg. Moreover, we changed the frequency of the periodic external force $\omega \in (0, \ 30]$. to show that the muscles can adapt with the periodic external forces with various

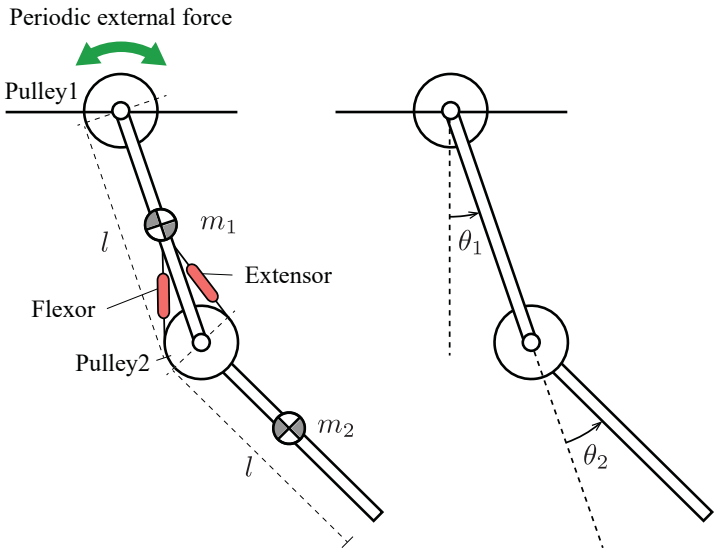

Fig. 5.13 Force-excited limb model with an periodic external force. The periodic force is applied to the upper joint, and the flexor and extensor muscle pair is fixed on the bottom joint.

frequencies. The initial phase and phase difference were set as $\theta_1(0) = 30$ deg, $\theta_1(0) - \theta_2(0) \in [-30,\ 30]$ deg, and the viscoelastic constants of all muscles were identical. The periodic external force is applied as $10\sin(\omega t)$. In this simulation, we considered the gravitational acceleration g, and selected the other parameters, gains, and initial states, as follows:

$$m_1 = 0.2,\ m_2 = 0.12,\ k_{1,F} = k_{1,E} = k_2 = 100\ \mathrm{N/m}, \tag{5.48}$$

$$c_F = c_E = 0.1,\ c_{\theta 1} = c_{\theta 2} = 1\ \mathrm{sN/m},\ \tau = 0.01,\ a = 1 \tag{5.49}$$

$$\varepsilon_1 = 10,\ \varepsilon_{\gamma 1} = 10,\ \varepsilon_{\gamma 2} = 0,\ l = 0.5\ \mathrm{m},\ d = 0.4\ \mathrm{m},\ g = 9.8\ \mathrm{s^2/m} \tag{5.50}$$

$$\dot{\theta}_1(0) = 0\ \mathrm{deg/s},\ r_F(0) = r_E(0) = 0,\ \dot{r}_F(0) = \dot{r}_E(0) = 0. \tag{5.51}$$

Additionally, we choose the sensory gain in $(\varepsilon_{\gamma 1},\ \varepsilon_{\gamma 1}) = (1,\ 0),\ (0,\ 1),\ (1,\ 1)$.

Fig. 5.14, 5.15, and 5.16 presents the simulation results with the different sensory gain in $(\varepsilon_{\gamma 1},\ \varepsilon_{\gamma 1}) = (1,\ 0),\ (0,\ 1),\ (1,\ 1)$. The color of the sphere denotes the phase difference of the converged solution of the two joint angles. The blue sphere denotes that the two joints converged to a solution in an in-phase manner, while the red sphere denotes that the joints converged to a solution in an anti-phase manner.

In the Fig. 5.14, the phase differences of the converged solution change as increasing the frequency of the periodic force ω. The transition took place at approximately $\omega = 10$, and each solution converged to the resonance modes as shown in the top figures. This result shows the reflex controller in the muscle pair adjusted its own motions and generated suitable gaits for body dynamics adaptively to the external force. However, in the Fig. 5.15 and 5.16, the phase differences of the converged solution did not change as the frequency of the periodic force ω increases. This result shows the muscle reflex keeps the joint angle θ_2 to the excited joint θ_1 due to the muscle velocity feedback $\varepsilon_{\gamma 2}$ stabilized the bottom joint θ_2.

Fig. 5.17, 5.18, and 5.19 show the time response of the limb angles θ_1 and θ_2 in Fig. 5.14

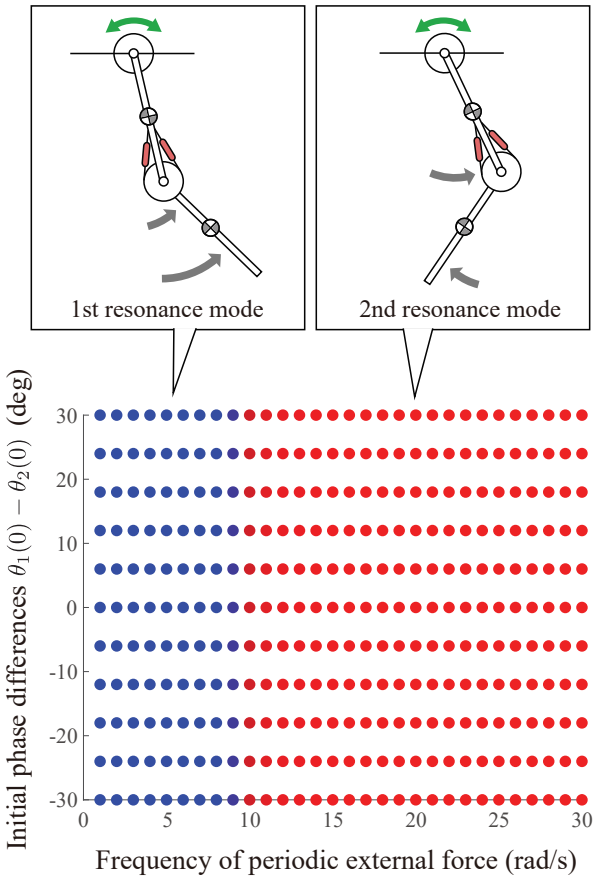

Fig. 5.14 Simulation results using the force-excited limb model with only the muscle displacement feedback $\varepsilon_{\gamma 1} = 1$, $\varepsilon_{\gamma 2} = 0$. We changed the initial phase difference $\theta_1(0) - \theta_2(0) \in [-30,\ 30]$deg and the frequency of the periodic external force $\omega \in (0,\ 30]$. The blue sphere denotes that the two joints converged to a solution in an in-phase manner, while the red sphere denotes that the joints converged to a solution in anti-phase manner. The top figures present the converged solution.

with various sensor gains. The initial phase difference and the frequency of the external force are $\theta_1(0) - \theta_2(0) = 30$, and the left and right figure show the result with $\omega = 8,\ 12$. Fig. 5.17 (a)(b) shows the results with only the muscle displacement feedback $\varepsilon_{\gamma 1} = 1$, $\varepsilon_{\gamma 2} = 0$. In the figures, (a) the angles converged to the 1st mode in an in-phase manner and (b) to the 2nd mode in an anti-phase manner, respectively. From the figures, the stretch reflex with the muscle displacement feedback $\varepsilon_{\gamma 1} = 1$ adjusted and amplified the waveform of the limb motion that is caused by the forced-excitation, and as a result, the system converged to the resonance modes. Fig. 5.18 (a)(b) shows the results with only the muscle velocity feedback $\varepsilon_{\gamma 1} = 0$, $\varepsilon_{\gamma 2} = 1$. In the figures, (a) (b) the angles converged to the 1st mode in an in-phase manner. From the figures, the stretch reflex with the muscle velocity feedback $\varepsilon_{\gamma 2} = 1$ synchronize the limb angle with the external force and decrease the amplitude of oscillation. The results in Fig. 5.19 (a)(b) are almost same, and it suggest that the muscle velocity feedback $\varepsilon_{\gamma 2} = 1$ is more dominant than the displacement feedback.

From these results, also with the forced-excitation by the CPG and upper central (the sec-

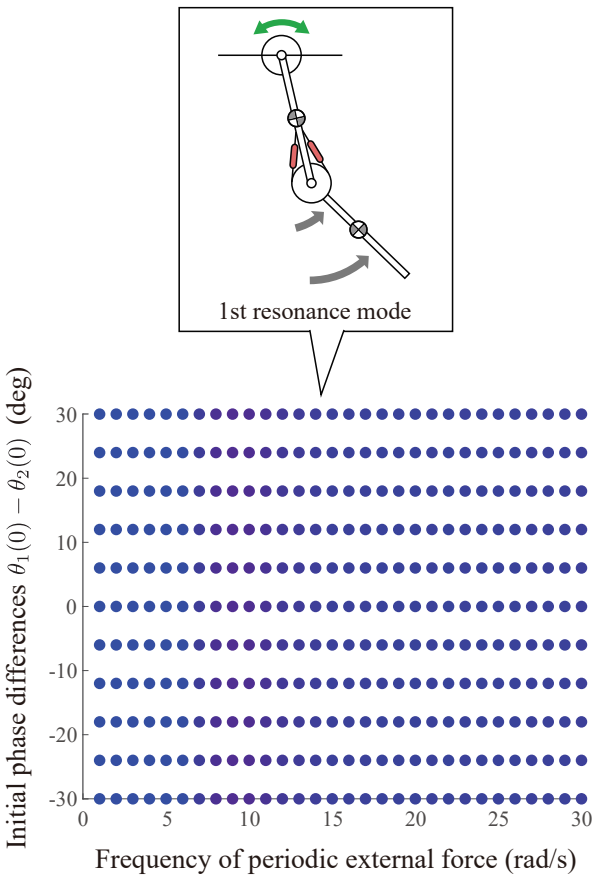

Fig. 5.15 Simulation results using the force-excited limb model with only the muscle velocity feedback $\varepsilon_{\gamma 1} = 0,\ \varepsilon_{\gamma 2} = 1$. We changed the initial phase difference $\theta_1(0) - \theta_2(0) \in [-30,\ 30]$deg and the frequency of the periodic external force $\omega \in (0,\ 30]$. The blue sphere denotes that the two joints converged to a solution in an in-phase manner, while the red sphere denotes that the joints converged to a solution in anti-phase manner. The top figures present the converged solution.

ond candidate of the rhythm source), the local reflex strategy also contributes to the pattern formation by exploiting inter-muscular interaction through the physical body dynamics. Moreover, the reflex controller can easily suppress and stabilize the corresponding joint by increasing the sensor gain for the muscle velocity.

5.8 Discussion

The theoretical results in Theorem 1 and Theorem 2, and the simulation results Fig. 5.6, 5.9, 5.11 shows that the large sensor gain causes the limit cycles in resonance frequency. These self-excited limit cycles that is generated by the dynamics of the stretch reflex is the first candidate of the rhythm generator. With the self-excitation, the local reflex strategy contributes to the pattern formation by exploiting inter-muscular interaction through the physical body dynamics.

As a second candidate of the source of rhythm generation, we employed the forced-

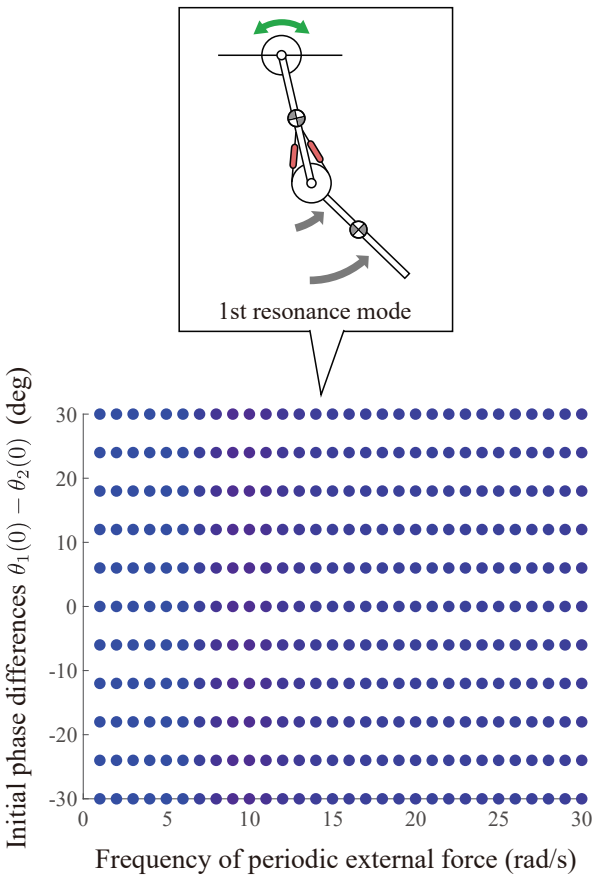

Fig. 5.16 Simulation results using the force-excited limb model with both the muscle displacement and velocity feedback $\varepsilon_{\gamma 1} = 1$, $\varepsilon_{\gamma 2} = 1$. We changed the initial phase difference $\theta_1(0) - \theta_2(0) \in [-30,\ 30]$deg and the frequency of the periodic external force $\omega \in (0,\ 30]$. The blue sphere denotes that the two joints converged to a solution in an in-phase manner, while the red sphere denotes that the joints converged to a solution in anti-phase manner. The top figures present the converged solution.

excitation by the external periodic forces. The forced-excitation is equivalent to a function in animals in which the motor control signal is generated by the other candidate of the rhythm source: the CPGs and the upper central. Fig. 5.14, 5.15, 5.16, 5.17, 5.18, and 5.19 presented the simulation results with the muscle displacement and velocity information through two kinds of feedback pathway, the static and dynamic γ. From these results, also with the forced-excitation, the local reflex strategy also contributes to the pattern formation by exploiting inter-muscular interaction through the physical body dynamics.

Moreover, these results showed that animals adjust their motor patterns by changing the sensory gain of the muscle displacement $\varepsilon_{\gamma 1}$ and velocity $\varepsilon_{\gamma 2}$, such as increase $\varepsilon_{\gamma 1}$ when a large amplitude motion is needed, or increase $\varepsilon_{\gamma 2}$ when a careful and powerful motion or a stable position control is needed. Such gain adjustment is in agreement with measurements of cat motions [85]. When the cat relax, both the activity of the static γ neuron (mainly, increase the muscle displacement gain) and dynamic γ (increase the velocity gain) keep low level. However, the activity of the static γ increase when the cat walking and running, the

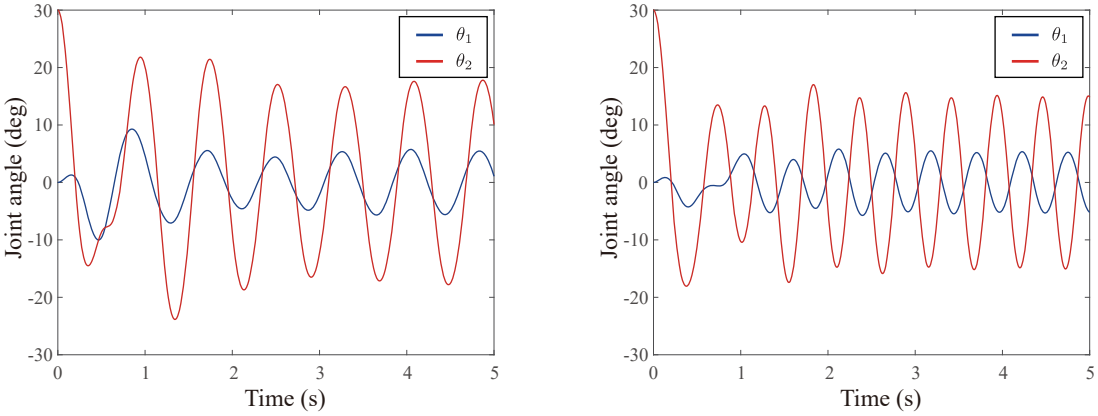

(a) $\omega = 8$ (b) $\omega = 12$

Fig. 5.17 Time response of limb angles θ_1 and θ_2 with only the muscle displacement feedback $\varepsilon_{\gamma 1} = 1,\ \varepsilon_{\gamma 2} = 0$. The initial phase difference and the frequency of the external force are $\theta_1(0) - \theta_2(0) = 30$. The left and right figure show the result with $\omega = 8,\ 12$.

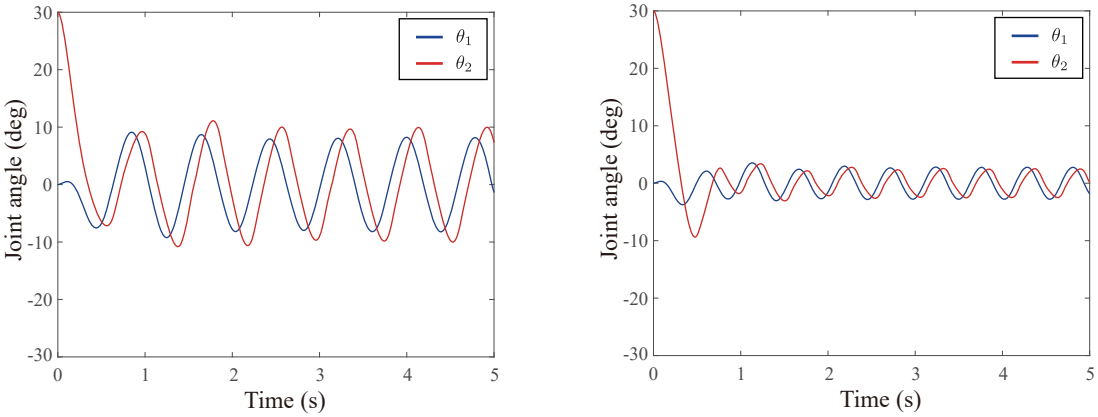

(a) $\omega = 8$ (b) $\omega = 12$

Fig. 5.18 Time response of limb angles θ_1 and θ_2 with only the muscle velocity feedback $\varepsilon_{\gamma 1} = 0,\ \varepsilon_{\gamma 2} = 1$. The initial phase difference and the frequency of the external force are $\theta_1(0) - \theta_2(0) = 30$. The left and right figure show the result with $\omega = 8,\ 12$.

dynamic γ increase when the forced motions, such as when lifting the cat body. Both the static and dynamic γ increase when in the difficult tasks, such as the cat walking on a balance beam.

As shown in the result, the stretch reflex strategy without an electrical inter-muscular communication provides a function of the pattern formation adaptively to the body dynamics. The pattern is the resonant modes, which is most easily excited motion through body dynamics and advantageous to generate various large amplitude motion. The other function–the rhythm generator, which is needed for the motor patterns of animals, is considered to be the self-excitation phenomenon of muscles, the central nervous networks (CPG and upper central), or both. Although it is unclear that which (or both) of these is the source of rhythm generation, using whichever two candidates of the rhythm source, the reflex model provides the function of the pattern formation. From this result, we concluded that the source of

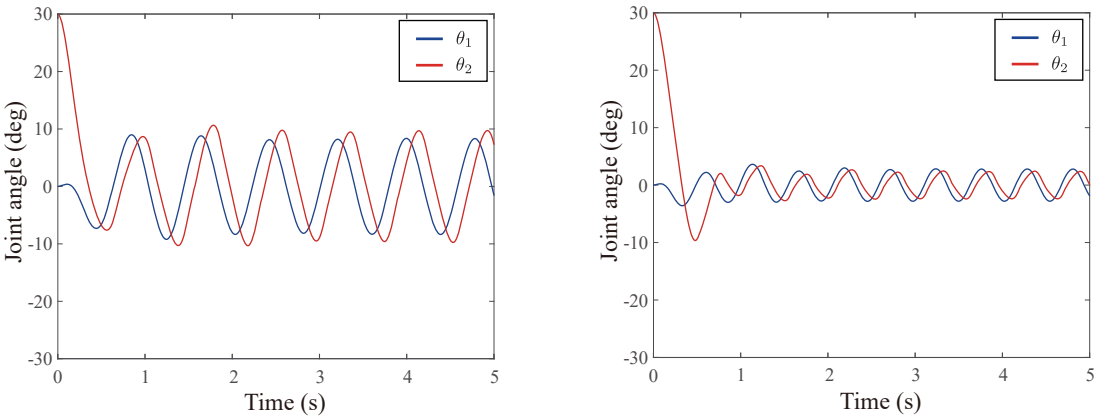

(a) $\omega = 8$ (b) $\omega = 12$

Fig. 5.19 Time response of limb angles θ_1 and θ_2 with both the muscle displacement and velocity feedback $\varepsilon_{\gamma 1} = 1$, $\varepsilon_{\gamma 2} = 1$. The initial phase difference and the frequency of the external force are $\theta_1(0) - \theta_2(0) = 30$. The left and right figure show the result with $\omega = 8,\ 12$.

pattern generation is in the physical interaction between primitive stretch reflex controllers through body dynamics, because the physically natural modes appear even in the quite simple configuration having no electrical inter-muscular communication.

5.9 Future work

In this thesis, the local reflex chains through the physical body dynamics generated various physically natural and large amplitude motions, and the brainless robot that has the roughly equivalent (implicit) controller automatically generated typical animal gaits. The extremely simple configuration for the animal motor functions provides a sufficient condition for the motor pattern generation of animals. The results in this study suggested that the physically coupled reflex chain is a strong candidate for the fundamental basis for the pattern formation in animals.

However, some works are remains for supporting the result. The simulated limb model has no interaction between the ground surface, thus a walking simulation and experiments are needed. To show more reliable result, some experiments using actual animals or biomimetic robot models that duplicate animal musculoskeletal system and motor functions. Moreover, the source of rhythm generation is still unclear, and particularly, more detailed explanation for the self-excitation phenomenon using physiological evidences is a future work.

Chapter 6

Conclusion

This thesis investigated underlying mechanisms that enable the motor patterns (typically observed as gaits) in nature animals by using an extremely simple legged robot and physiological reflex model. As a result, we showed a candidate of the fundamental basis for motor control of legged robots and animals.

6.1 Part I

In Part I, we developed a quadruped robot that provides a clue to the issue: a sufficient condition for generating the animal gaits. The brainless walking robot having no explicit controller showed typical animal gaits (walk and gallop), and the different types of brainless robots (snake-like and earthworm-like robots) generate various animal motions that suits their own body dynamics and constraint condition from the environments. The key of the adaptivity was an electrical passivity of low-torque DC motors, and these passivity adjusts each motor phase by exploiting the physical force interaction through the body and environment dynamics.

To evaluate this control method, some experiments, simulations and theoretical analysis were conducted for the brainless robot and two fundamental systems (a spring-mass system and a planar quadruped model). The experiments and simulations showed a key feature that the electrical passivity of the motors generates resonant modes of the system. This feature allowed the robot to generate various large amplitude motions even with uncertain body structures and environments. The theoretical results provide an interpretation for the function that is interpreted as an implicit controller to down the slope of the Hamiltonian potential for the system and dissipation energy, momentary. In other words, the compliant oscillator may decrease the Hamiltonian and energy loss of the mechanical system, but more theorems for nonlinear systems are needed to prove that ability.

The proposed method has three clear advantages that differs from the conventional decentralized controllers. First, since the method needs no sensor, microprocessor, certain precise and high-torque motor, nor explicit controller, therefore, it significantly reduces the implementation cost of conventional decentralized controllers. Second, this method needs no global information of the mechanical system and uses only the local force feedback. Therefore, the module may generate resonance modes of uncertain or unpredictable systems. As a

result, if the body and environment dynamics is changed by some troubles, the electrical passivity instantly adjusted the motions and adapt these uncertainty. Third, the proposed control method is powerless and inaccurate, but can generates physically natural motion that suit for the robot body and environment. Although this method does not suit for static and powerful tasks (e.g., position control or object manipulation), it will be a new approach for robot design by using this method as a fundamental basis of the robot motor control and adding just a little explicit controllers for the powerful tasks, as with the motor command from the brain.

6.2 Part II

The major contribution of Part II is to show that a candidate of the source of animal motor patterns is in the body dynamics, and the extremely simple reflex controllers play a role to adjust the waveforms of the body motions. This model denotes a primitive local control in animals, called the stretch reflex, and it is based on the analytical results of the brainless walking, which is introduced in Part I.

First, we constructed a model based on a dominant dynamics of the brainless walking, called the DFFB (Direct Force Feedback) model. The DFFB model provides almost the same time response and resonant modes as the low-torque DC motor model, and next, we constructed a physiological model by focusing on an analogy between the DFFB model and stretch reflex in animals. To discuss the major issue of this thesis "what is the source of motor patterns?", we introduced two terms, the *"rhythm generation"* that provides periodic rhythms, and the *" pattern formation"* that adjust the waveform of the body motions. For the rhythm generation, we introduce two candidates, called the *self-excitation* and *forced-excitation* method, and we mainly investigate the function of pattern formation in the animal reflexes.

In the simulations, the reflex model automatically generates resonant modes without any explicit neural connection between the models using whichever two candidates of the rhythm generation. Moreover, the model adjusts these motor patterns adaptively to changes in the parameters of the body structure. The extremely simple configuration for the animal reflex system provides a sufficient condition for generating the motor patterns. From these results, I will conclude that the physically coupled stretch reflexes are a strong candidate for the fundamental basis for the pattern formation in animals.

A

Appendix A

A.1 Brainless Earthworm-like Robot

Based on the successes of the brainless quadruped robot, we developed an earthworm-like robot that has a different body structure from the other brainless robots. In this chapter, we develop an extremely simple earthworm-like robot as a minimal configuration of the earthworm-like wave generation.

Numerous earthworm-inspired robots have been developed previously with various drive systems, electric motors [96, 97], solenoid [98], SMA [99, 100, 101, 102, 103, 104], DEA [105], magnetic field [106], and pneumatic [107]. For these artificial earthworms, some controllers for adaptive control [108, 109], gait generation [110, 111, 112] have been proposed. However, these previous robots and controllers employed predesigned phase differences or heuristic and complicated algorithms to generate gaits. Therefore, the source of the wave locomotion of earthworms is still unclear. An decentralized adaptive controller in an earthworm simulation was proposed in articles [113, 114], and we achieve a similar control law mechanistically by exploiting the electrical passivity intrinsic to motors.

The major contribution of this work is showing that autonomous peristaltic gait generation is possible without any explicit controller. Actual earthworms generate the contraction–expansion waves from head to tail, and the contracted segment inflates to generate friction from the ground [2]. To reproduce an earthworm-like body function, the proposed robot is composed of multiple body segments that are mutually coupled by a linear joint that contracts and expands its own body. Inflation of the body segments are reproduced by a flexible bottom plate that connects two adjacent segments. Each linear joint is connected to a low-torque DC motor through a slider-crank linkage, and produces periodic contraction–expansion motions under a constant voltage. Each motor, which drives the corresponding linear joint, adjusts its own phase according to the load torque applied from the other segments and ground surface. As a result, phase differences between linear joints and motors converge, and the robot generates peristaltic locomotion automatically.

A.2 Earthworm-like Robot without a Brain

A.2.1 Structure of the earthworm-like robot

Fig. A.1 Overview of the brainless earthworm-like robot.

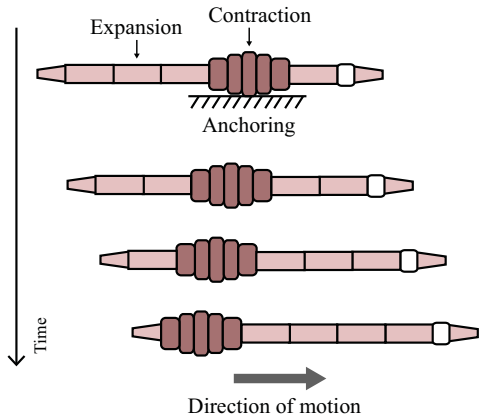

Fig. A.2 Schematic of an earthworm. Real earthworms generate contraction–expansion waves from head to tail, and the contracted segment inflates to generate friction from the ground [2].

In this chapter, we develop a brainless earthworm-like robot that autonomously generates a peristaltic wave without a sensor, controller, or microprocessor. The proposed robot is composed of six body segments, and each segment has one low-torque DC motor (Pololu 75:1 Micro Metal Gearmotor HP). Fig. A.1 shows the overview of the earthworm-like robot. The total weight of the robot is 409 g. The deformation length of each joint is 20 mm, and the total length during contraction and expansion are 430 mm and 510 mm, respectively. The total height during contraction and expansion are 125 mm and 120 mm, respectively.

Real earthworms generate contraction–expansion waves from head to tail, and the contracted segment inflates to generate friction from the ground [2] (Fig. A.2). To reproduce an earthworm-like structure, each segment is mutually coupled by a linear joint that contracts and expands its own body. Each linear joint is connected to a low-torque DC motor through a slider-crank linkage mechanism (Fig. A.3). This linkage is composed of a crank that connects the motor to the shaft, and a slider that connects the crank to the linear joint. The crank in continuous rotation produces periodic contraction–expansion motion. Inflation of the body segment is reproduced by a flexible polypropylene plate that connects two adjacent segments, and we attached anti-slip sheets (PVC foam sheets) to the bottom surfaces of the plate. In Fig. A.4, when the crank is rotated by the motor (red arrow), it produces periodic contraction–expansion waves under a constant voltage (blue arrow); at the same time, the bottom surface is pushed up and pulled down (green arrow).

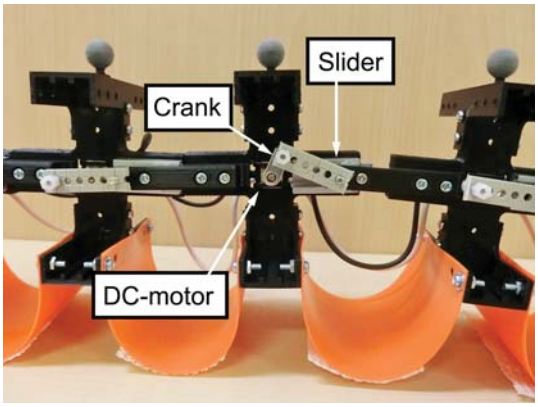

Fig. A.3 Structure of the contraction and expansion linkage mechanism that is composed of the slider and crank.

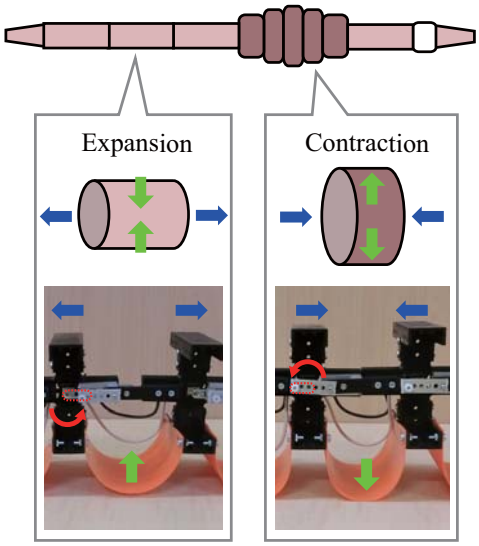

Fig. A.4 Movement of the earthworm-like robot. When the crank is rotated by the motor (red arrow), it produces periodic contraction–expansion waves under a constant voltage (blue arrow); at the same time, the bottom surface is pushed up and pulled down (green arrow).

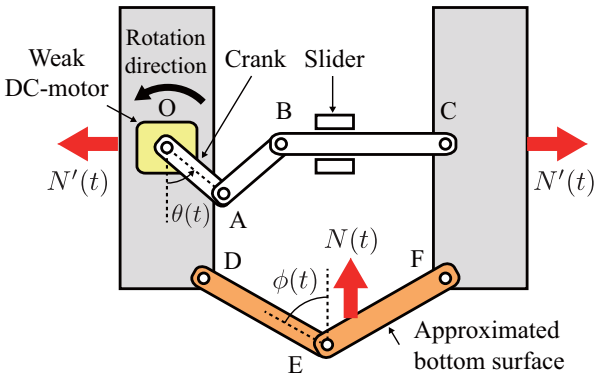

Fig. A.5 Model of the contraction and expansion mechanism.

A.2.2 Modeling of the contraction and expansion mechanism with a low-torque DC-motor

This robot has no sensor, controller, or microprocessor. The key concept behind this brainless earthworm-like robot is to exploit the passivity intrinsic to the low-torque DC motor in each linear joint as a control law. Each motor rotates continuously under a constant voltage from a stabilized power source, and adjusts its own phase by exploiting the dynamics intrinsic to the motor itself.

Fig. A.5 shows a model of the contraction and expansion mechanism. First, we assume that the flexible plate at the bottom can be approximated as a linkage in Fig. A.5 (link OABC, orange link), and that the link lengths $\overline{\mathrm{OA}}$ and $\overline{\mathrm{AB}}$, $\overline{\mathrm{DE}}$ and $\overline{\mathrm{EF}}$ are equal, respectively.

When the ground reaction force $N(t)$ is applied to the bottom link, a force $N'(t)$ to expand the body segment is generated as follows:

$$N'(t) = \frac{N(t)}{2}\tan\phi(t), \tag{A.1}$$

where $0 < \phi(t) < \pi/2$ is the angle of the bottom linkage. The force $N'(t)$ is transmitted through the linkage OABC and causes a disturbance torque τ that is applied to the motor shaft

$$\tau(t) = 2\overline{\mathrm{AO}}N'(t)\cos\theta. \tag{A.2}$$

Finally, by substituting Eq. (A.1) and Eq. (A.2) for Eq. (3.3), we get the entire model:

$$\dot{\theta}(t) = \omega + a(t)N(t)\cos\theta, \tag{A.3}$$

where $a(t) = \varepsilon\overline{\mathrm{AO}}\tan\phi(t)$ is a function that changes the transmission rate of the ground reaction force. From Eq. (A.3), when a ground reaction force $N(t) > 0$ is applied to the bottom surface, the low-torque DC motor adjusts its own phase through the linkage mechanism. In other words, the passivity of the DC motor for the purely physical mechanism Eq. (A.3) makes it function like a state feedback controller. The dynamics of Eq. (A.3) from the pure mechanical linkage is very similar to the controllers that generates quadruped gaits [47, 48], earthworm gaits [113], and caterpillar gaits [114].

A.3 Experiment

In this section, we conduct fundamental experiments to investigate the generated motor patterns.

Fig. A.6 shows the experimental setup. All of the motors were connected to a power source in parallel. The initial state of all linear joints was set to contract (all of the motor phases are $\theta = 3\pi/2$ in Fig. A.5). The trial was conducted once for each input voltage of 2 V and 3 V. The states of the robot was captured by a motion capture system, and the markers were attached above the each motor shaft.

Fig. A.7 and Fig. A.8 show the locomotion of the robot with 2 V. In the figures, after approximately 15 s, the linear joints generated wave from right to left, and as a result, the robot moved to the right (retrograde wave). Fig. A.9 shows the spatiotemporal plots of the motor phase with 2 V. From the figure, a steady peristaltic gait was generated as

$$\mathrm{M}otor1 \rightarrow \mathrm{M}otor2 \rightarrow \mathrm{M}otor3 \rightarrow \mathrm{M}otor1 \rightarrow \mathrm{M}otor2 \rightarrow ... \tag{A.4}$$

This manner of wave was the same as the gait of real earthworms. This result was caused by the interaction between the body segments and the ground contact conditions through the physical body dynamics. The movement of each motor was suppressed by the left and right

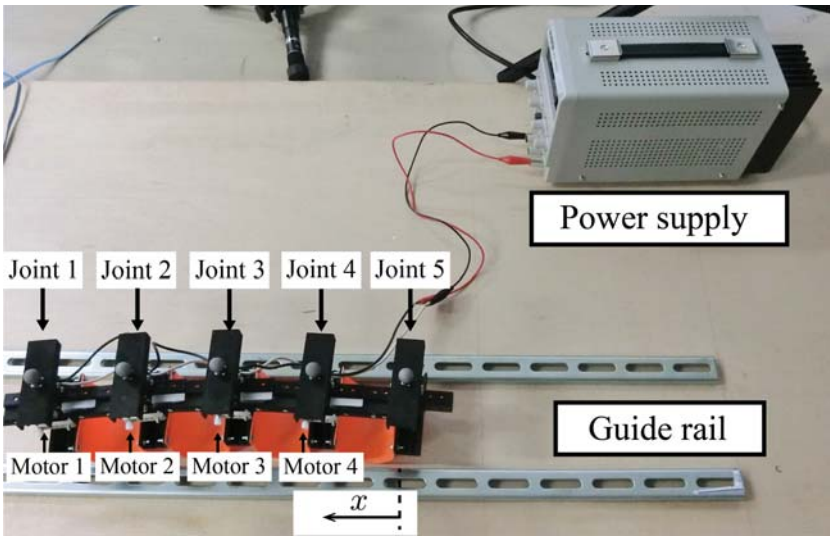

Fig. A.6 Experimental setup.

adjacent segments, and the ground reaction and friction forces. For these reasons, only the end segment moves first, and it seems that a chain expansion motion starting from the end segment occurred. However, there was a slow drift of the motor4 phase at $t = [15, 40]s$. This result assumed that the motor4 cannot receive a sufficient ground reaction forces owing to the lack of rigidity of the linear joint. The robot structure will be improved in future work.

Fig. A.10 and Fig. A.11 show the locomotion of the robot with 3 V. In the figure, the motors generated a steady in-phase pattern from beginning to end; as a result, the robot moves to the left. Fig. A.12 shows the spatiotemporal plots the motor phase with 3 V. The movement, in which all the motors contracted and expanded at the same time, was the 1st resonance mode of the robot body. It is assumed that this movement was caused by the inertial force between the body modules becoming greater than the frictional force.

A.4 Conclusion

In this chapter, we reported an extremely simple earthworm-like robot as a minimal configuration of the earthworm-like wave generation. This robot generated the peristaltic gait of actual earthworms autonomously without a sensor, controller, or microprocessor. The results suggest the contribution of the forces interacting between the body segments. Moreover, the robot generated different locomotion that adaptively corresponds to the input voltage. We expect that comparison of these two different phenomena will provide critical clues to understanding the contributions of friction and inertial force to peristaltic gait.

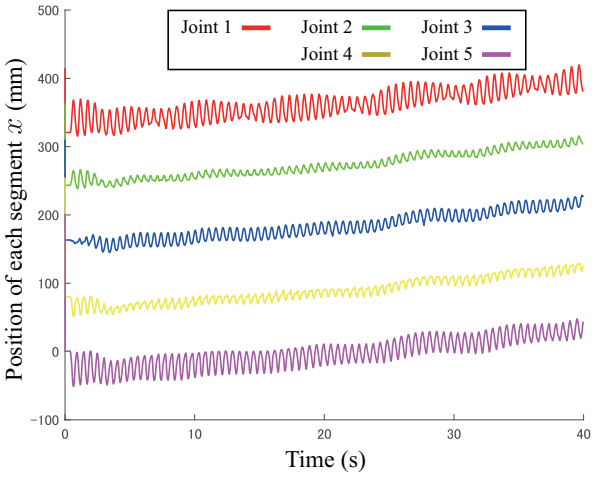

Fig. A.7 Experimental result with 2 V: horizontal displacement of the each joint.

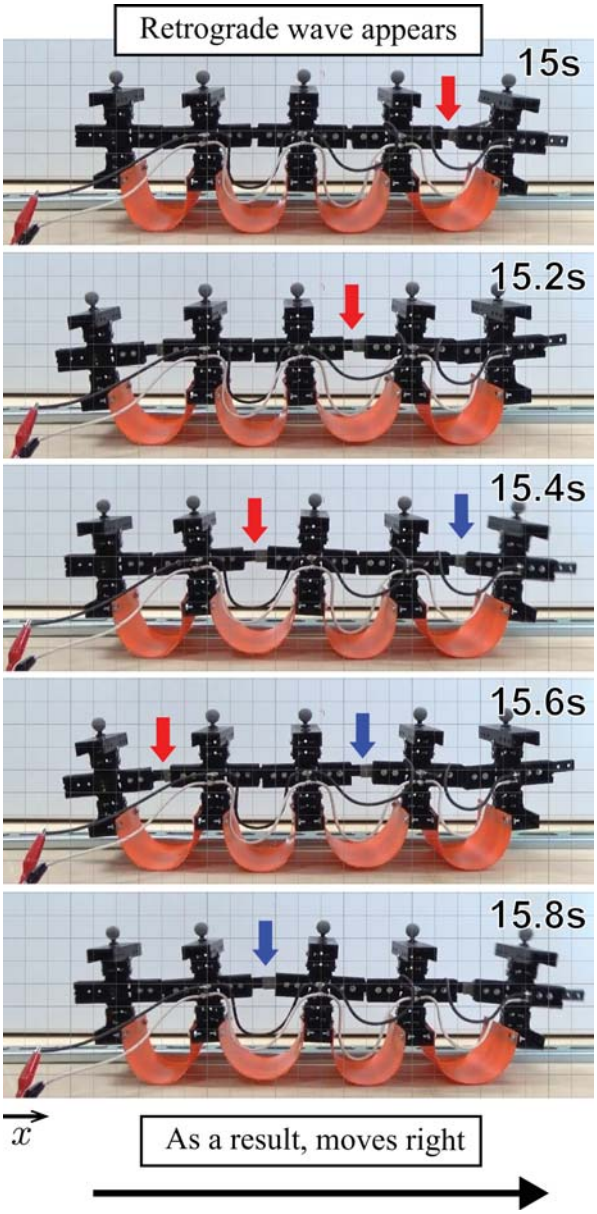

Fig. A.8 Snapshot of the locomotion with 2 V. The red and blue arrows denote extended joints. The robot generates retrograde wave (from right to left); as a result, the robot moves to the right.

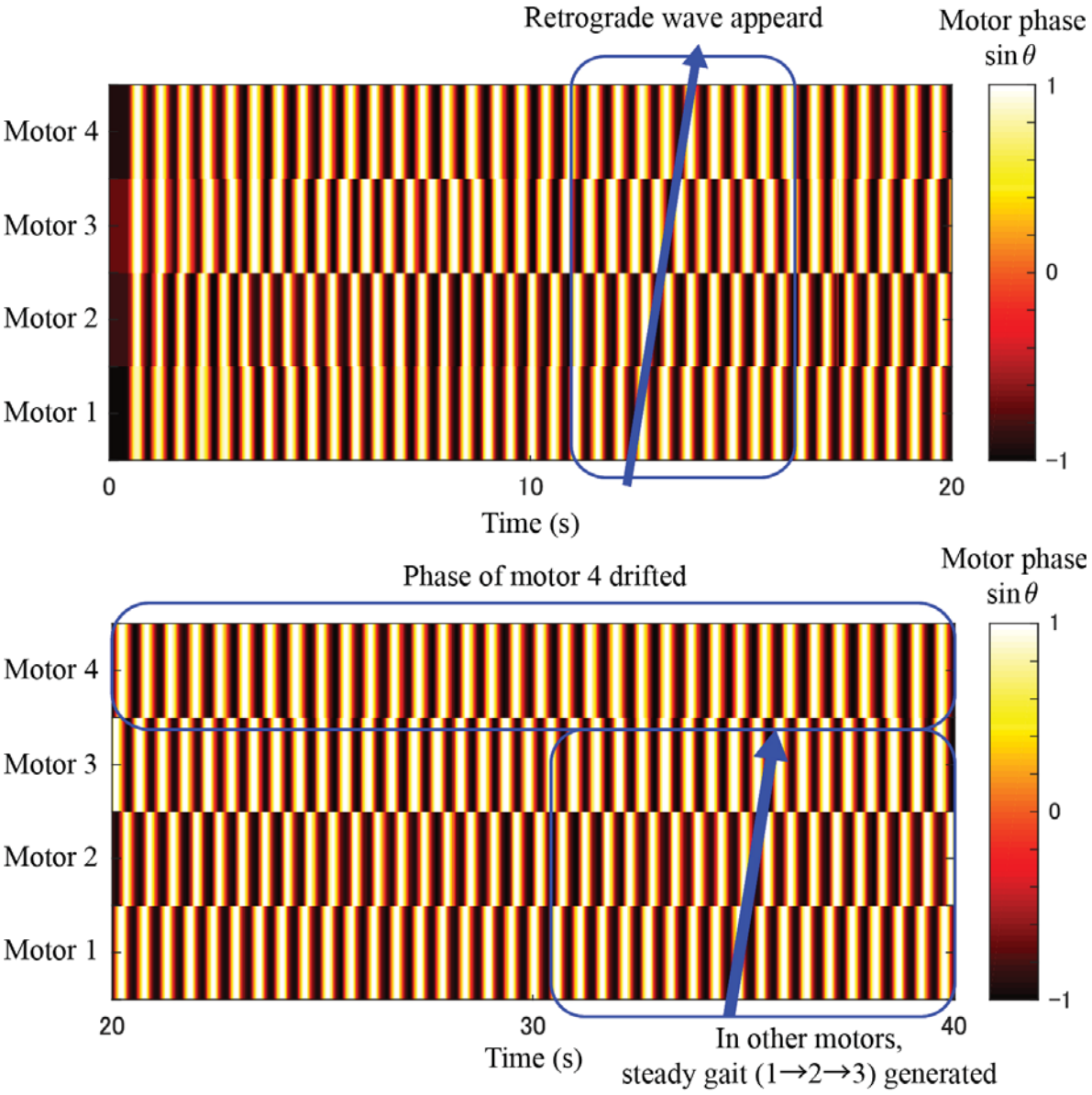

Fig. A.9 Spatiotemporal plot of the motor phase with 2 V. From the figure, in motor1, motor2, and motor3, a steady peristaltic gait is generated. However, there is a slow drift of the motor4 phase at $t = [15, 40]s$.

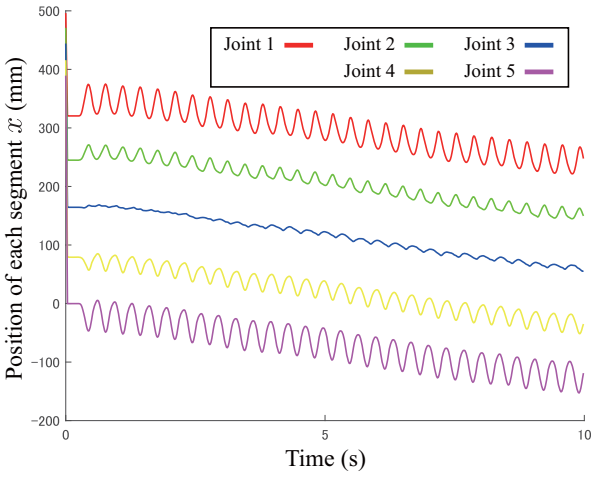

Fig. A.10 Experimental result with 3 V: horizontal displacement of the each joint.

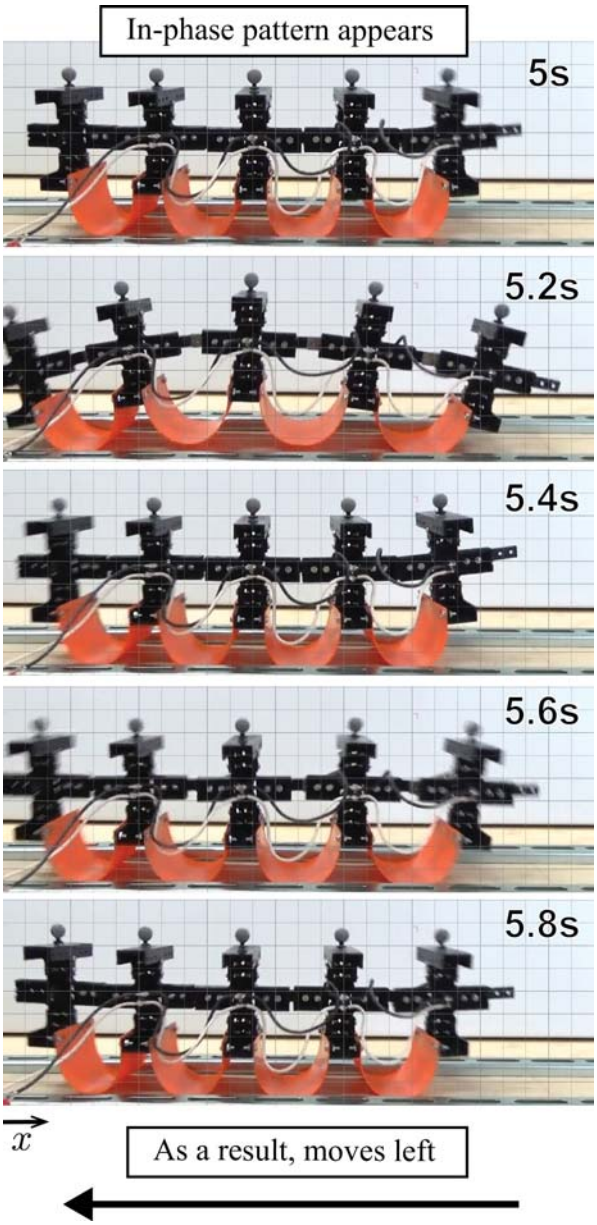

Fig. A.11 Snapshot of the locomotion with 3 V. The robot generates in-phase pattern; as a result, the robot moves to the left.

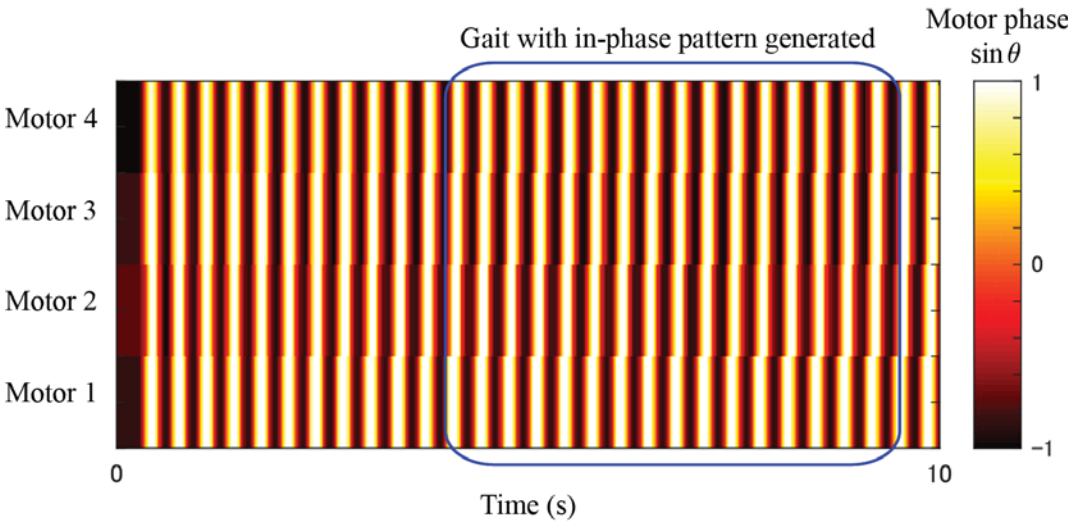

Fig. A.12 Spatiotemporal plot of the motor phase with 3 V. The movement, in which all the motors contract and expand at the same time, is the 1st resonance mode of the robot body.

B

Appendix B

B.1 Brainless Snake-like Robot

Based on the successes of the brainless quadruped robot, we developed a snake-like robot that has a different body structure from the other brainless robots. In this chapter, we developed an extremely simple snake-like robot as a minimal configuration of the snake-like wave generation and its environmental adaptability.

B.1.1 Structure of the snake-like robot

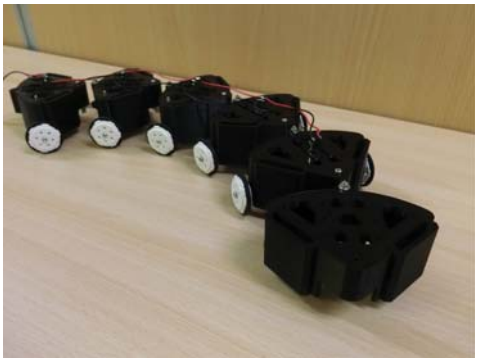

Fig. B.1 Overview of the brainless snake-like robot.

In this chapter, we develop a brainless snake-like robot (Fig. B.1) that generates motion patterns adaptively and autonomously without a sensor, controller, or microprocessor.

Fig. B.2 shows the structure of the proposed robot. The total weight of the robot is around 430 g, and the total length is around 500 mm. The proposed robot is composed of six body segments with passive wheels, and each segment has one low-torque DC motor (Pololu 75:1 Micro Metal Gearmotor HP). Each segment is mutually connected by revolute joint, and each joint is connected to a low-torque DC motor through a slider-crank mechanism. The distance between the revolute joints is around 90 mm, and the crank length is around 12 mm.

Fig. B.3 shows the link mechanism in the robot. This linkage is composed of a crank connected to the motor shaft and a slider connected the crank to the revolute joint. The crank in continuous rotation swings the slider and produces a periodic joint motions.

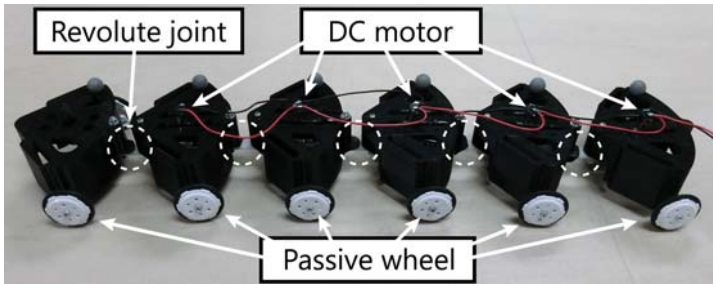

Fig. B.2 Structure of the brainless snake-like robot.

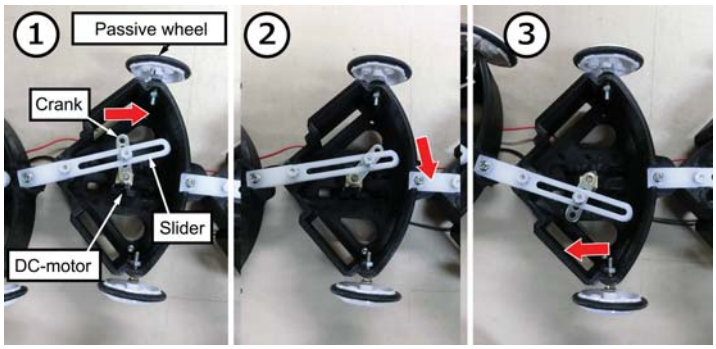

Fig. B.3 Structure of the slider-crank mechanism.

B.2 Experiment

In this section, we conduct locomotion experiments on different environments (flat ground, water, and sand) and investigate generated motion patterns.

The initial state of all joint was set to be on a straight line. All of the motors were connected to a power source in parallel, and the input voltage was changed in 2 to 4 V at 1 V intervals.

B.2.1 Environmental adaptability on flat ground

First, we confirm environmental adaptability of the proposed snake-like robot on the flat ground.

In this environment, we conducted two experiments with different ground contact conditions. Fig. B.4 (a)(b) show each contact condition. In the first condition, all the passive wheels touch the ground, and in the second, the wheels of one end segment are removed (the end segment is floating).

Fig. B.4 (c) shows the experimental result when all the passive wheels touch the ground with 3 V. In Fig. B.4 (c) with all wheels, the robot moves toward the lower side while adjusting the motor phases. However, after around 10 seconds, the joint angles falls into an stationary wave in anti-phase manner (adjacent joints move in an opposite direction), and the robot stays in there.

Fig. B.4 (d) shows the experimental results when the wheels of one end segment are removed with 3 V. In Fig. B.4 (d) without wheels of one end segment, the robot moves forward

(a) Ground contact condition 1 with dynamical fore–hind symmetry: all the passive wheels touch the ground

(b) Ground contact condition 2 with dynamical fore–hind asymmetry: the wheels of one end segment are removed

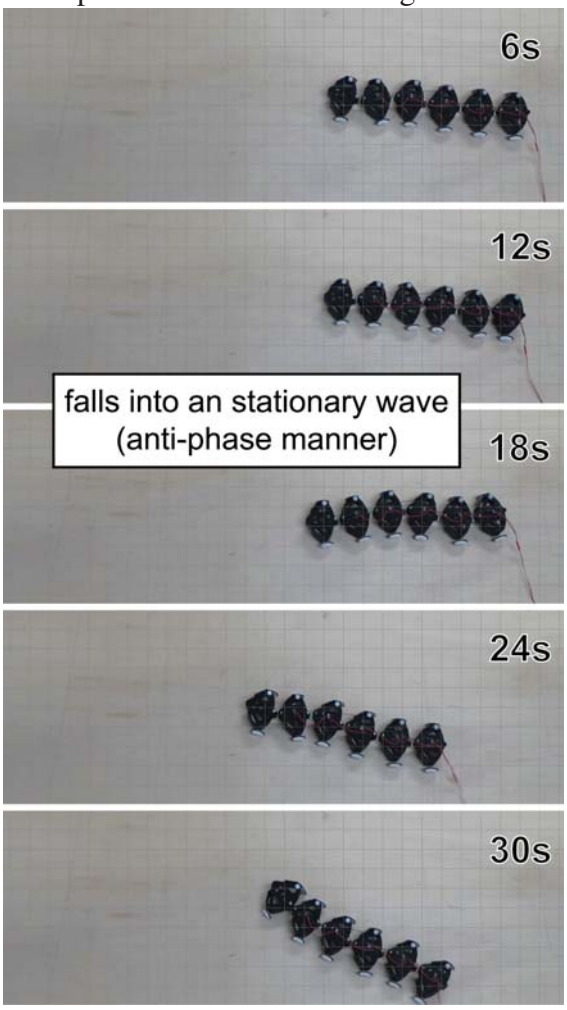

(c) Experimental result when all the passive wheels touch the ground with 3 V

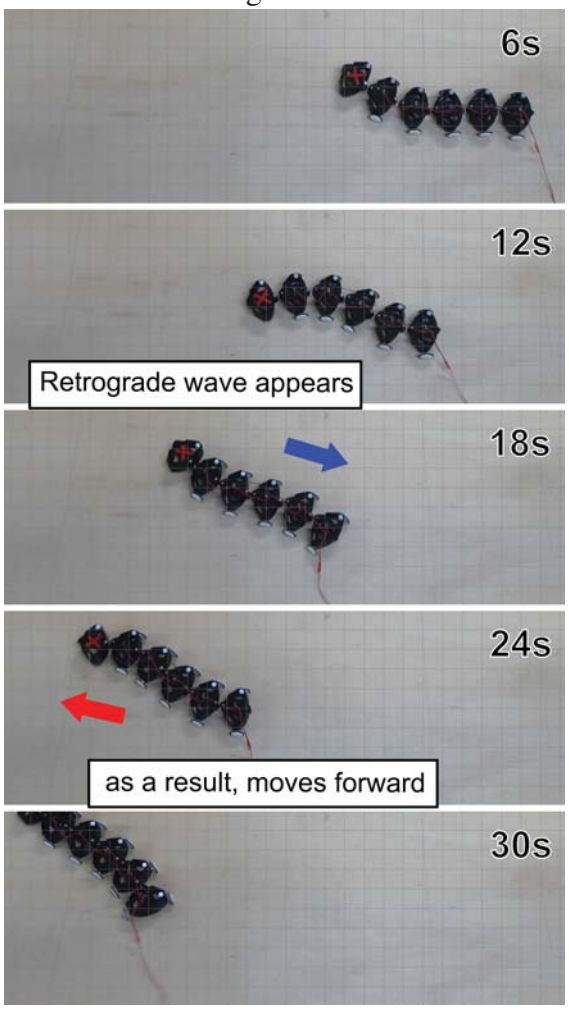

(d) Experimental result when the wheels of one end segment are removed with 3 V

Fig. B.4 Two ground contact conditions and corresponding experimental results. (C) The robot moves toward the lower side while adjusting the motor phases. However, after around 10 seconds, the joint angles falls into a stationary wave in anti-phase manner (adjacent joints move in an opposite direction) (D) The robot moves forward while adjusting the motor phases. After around 3 seconds, the joint angles converge into a retrograde wave (that in a direction opposite to travelling direction of the robot).

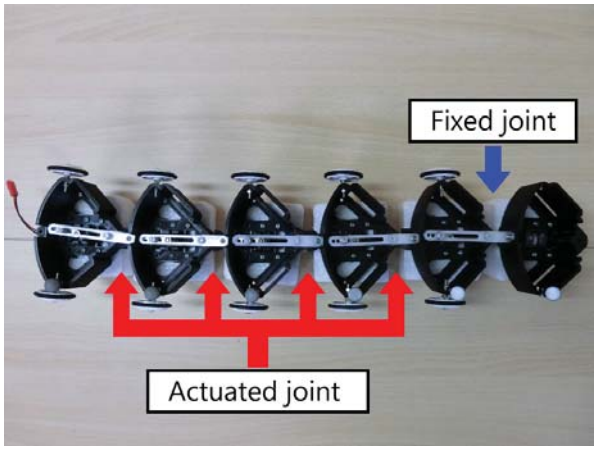

Fig. B.5 Experimental condition for water and sand. To break the fore–hind symmetry of the body structure, we fixed the joint of one end segment.

while adjusting the motor phases. After around 3 seconds, the joint angles converge into a retrograde wave (that in a direction opposite to travelling direction of the robot), and the robot continues to move forward. The result in all other voltages were almost the same as this result.

A difference of these two results is in the symmetry of the robot body structure. The first pattern in Fig. B.4 (c) has a fore–hind symmetry. However, patterns that contribute to locomotion need to propagate waves from fore to hind, or hind to fore.

B.2.2 Environmental adaptability on water and sand

Second, we conduct the experience on water and sand.

To break the fore–hind symmetry of the body structure, we fixed the joint of one end segment (only the joints except the joint of one end segment are driven, as shown in Fig. B.5). Moreover, we made minor modification to the contact surface corresponding to the environments. Fig. B.6 (a)(b) show each contact surface for water and sand. In Fig. B.6 (a), we put floats, stabilizers, and fins under the robot, and in Fig, B.6 (b), we put smooth bottom surfaces.

Fig. B.6 (c) shows the experimental result on water with 4 V. In Fig. B.6 (c), the robot stays while adjusting the motor phases. After around 15 seconds, the joint angles converge into a retrograde wave, and as a result, a forward locomotion is occurred. However, with all other voltages except 4 V, we could not observe steady state locomotion. One of the reasons of the unsteady locomotions in the other voltages except 4 V can be considered that the interaction between the contact surface (with the floats and the fins) and the environment is too small, as compared with the motor torque.

Fig. B.6 (d) shows the experimental result on sand with 4 V. As with the result on water, in Fig. B.6 (d), the robot stays while adjusting the motor phases. Around 30 seconds, the motion pattern was changed dominantly, and a retrograde wave and a very slow forward locomotion is occurred. The result in all other voltages were almost the same as this result, but the convergence time of all other voltages were shorter than 4 V dominantly (less than

10 second). It is considered that the dominant pattern transition with 4 V is caused by a characteristic inherent in sand locomotion. Focusing on the trail of robot locomotion on sand, the robot pushed sand aside and made a sand wall around the robot. We call this phenomenon inherent in sand locomotion *the self environmental modification*, in which the robot itself modifies the environment for its own locomotion. A plan to investigate this phenomenon is now ongoing, and it will be reported in our future work.

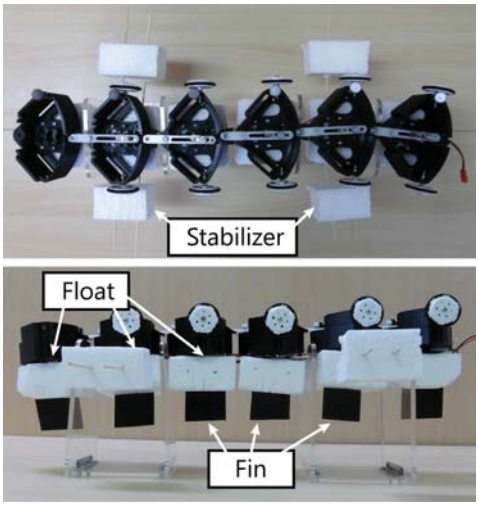

(a)

Contact surface for water: floats, stabilizers, and fins under the robot

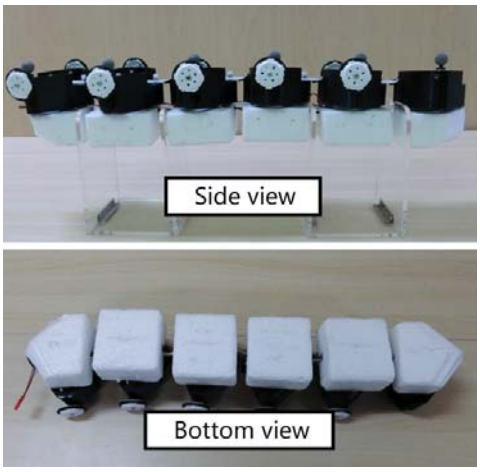

(b)

Contact surface for sand: smooth bottom surfaces under the robot

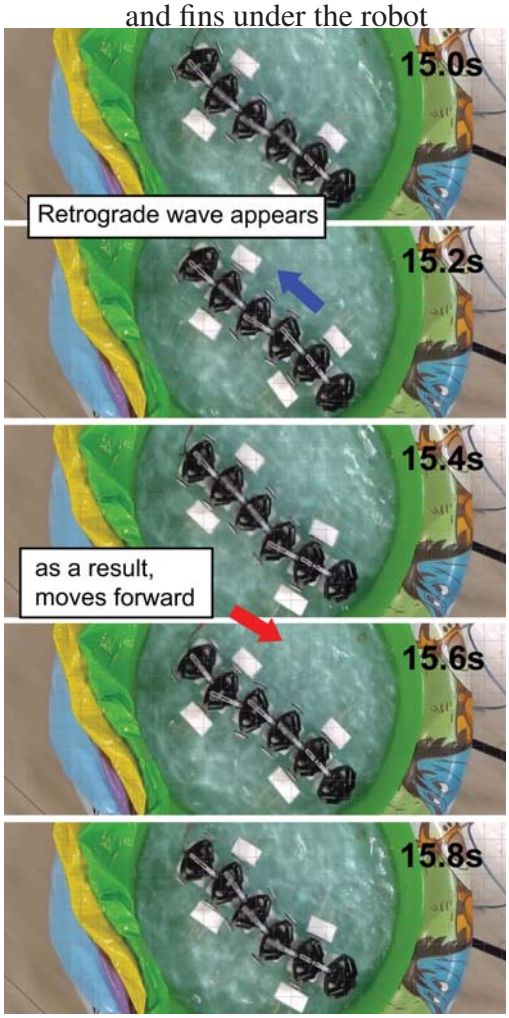

(c)

Experimental result on water with 4 V

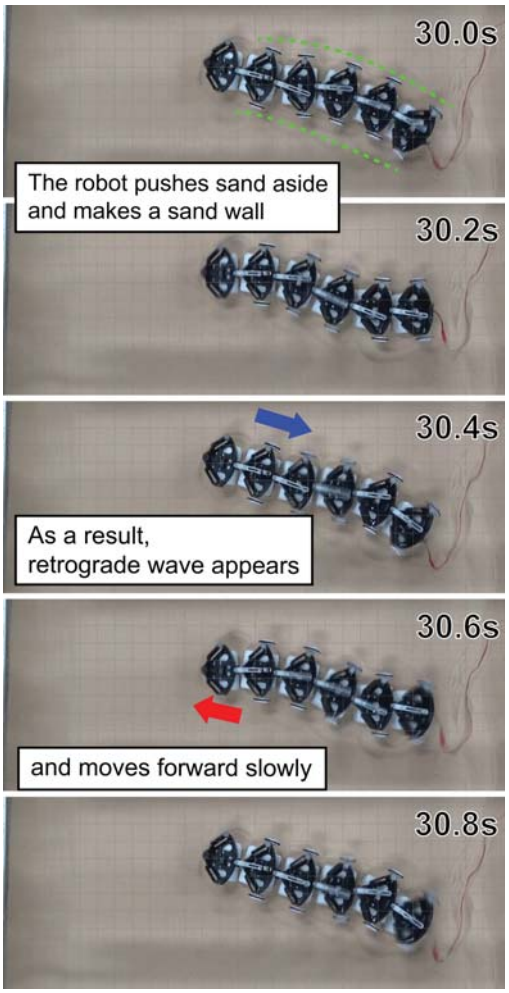

(d)

Experimental result on sand with 4 V

Fig. B.6 Two contact surfaces for locomotion on water and sand, and corresponding experimental results. The robot stays while adjusting the motor phases. Around a few tens of seconds, the motion pattern was changed and a forward locomotion with retrograde wave is occurred

Bibliography

[1] H. W. Park, M. Y. M. Chuah, S. Kim, *et al.*, "Quadruped bounding control with variable duty cycle via vertical impulse scaling," *Intelligent Robots and Systems (IROS), 2014 IEEE/RSJ International Conference on*, 2014.

[2] J. Gray and H. Lissmann, "Studies in animal locomotion: Vii. locomotory reflexes in the earthworm," *Journal of Experimental Biology*, vol. 15, no. 4, pp. 506–517, 1938.

[3] R. M. Alexander, *Principles of animal locomotion*. Princeton University Press, 2003.

[4] ——, "The gaits of bipedal and quadrupedal animals," *The International Journal of Robotics Research*, vol. 3, no. 2, pp. 49–59, 1984.

[5] E. Muybridge, *Animal locomotion*. Da Capo Press New York, 1969.

[6] F. J. Diedrich and W. H. Warren Jr, "Why change gaits? dynamics of the walk-run transition." *Journal of Experimental Psychology: Human Perception and Performance*, vol. 21, no. 1, p. 183, 1995.

[7] ——, "The dynamics of gait transitions: Effects of grade and load," *Journal of motor behavior*, vol. 30, no. 1, pp. 60–78, 1998.

[8] J. A. Vilensky, J. N. Libii, and A. M. Moore, "Trot-gallop gait transitions in quadrupeds," *Physiology & Behavior*, vol. 50, no. 4, pp. 835–842, 1991.

[9] D. F. Hoyt and C. R. Taylor, "Gait and the energetics of locomotion in horses." *Nature*, 1981.

[10] N. C. Heglund, C. R. Taylor, and T. A. McMahon, "Scaling stride frequency and gait to animal size: mice to horses," *Science*, vol. 186, no. 4169, pp. 1112–1113, 1974.

[11] T. M. Casey, M. L. May, and K. R. MorganOrgan, "Flight energetics of euglossine bees in relation to morphology and wing stroke frequency," *Journal of Experimental Biology*, vol. 116, no. 1, pp. 271–289, 1985.

[12] R. J. Kosinski, "A literature review on reaction time," *Clemson University*, vol. 10, 2008.

[13] P. B. Matthews, "The human stretch reflex and the motor cortex," *Trends in neurosciences*, vol. 14, no. 3, pp. 87–91, 1991.

[14] M. L. Shik, "Control of walking and running by means of electrical stimulation of the midbrain," *Biophysics*, vol. 11, pp. 659–666, 1966.

[15] G. W. Hiebert and K. G. Pearson, "Contribution of sensory feedback to the generation of extensor activity during walking in the decerebrate cat," *Journal of neurophysiology*, vol. 81, no. 2, pp. 758–770, 1999.

[16] K. Pearson, Ö. Ekeberg, and A. Büschges, "Assessing sensory function in locomotor systems using neuro-mechanical simulations," *Trends in neurosciences*, vol. 29, no. 11, pp. 625–631, 2006.

[17] J. Hoffer and S. Andreassen, "Regulation of soleus muscle stiffness in premammillary cats: intrinsic and reflex components." *Journal of neurophysiology*, vol. 45, no. 2, pp. 267–285, 1981.
[18] T. Nichols and J. Houk, "Improvement in linearity and regulation of stiffness that results from actions of stretch reflex," *journal of Neurophysiology*, vol. 39, no. 1, pp. 119–142, 1976.
[19] E. P. Zehr and R. B. Stein, "What functions do reflexes serve during human locomotion?" *Progress in neurobiology*, vol. 58, no. 2, pp. 185–205, 1999.
[20] L. Nashner, "Adapting reflexes controlling the human posture," *Experimental brain research*, vol. 26, no. 1, pp. 59–72, 1976.
[21] T. Sinkjaer, J. B. Andersen, and B. Larsen, "Soleus stretch reflex modulation during gait in humans," *Journal of neurophysiology*, vol. 76, no. 2, pp. 1112–1120, 1996.
[22] P. Dyhre-Poulsen, E. B. Simonsen, and M. Voigt, "Dynamic control of muscle stiffness and h reflex modulation during hopping and jumping in man." *The Journal of Physiology*, vol. 437, no. 1, pp. 287–304, 1991.
[23] G. M. Jones and D. Watt, "Observations on the control of stepping and hopping movements in man," *The Journal of Physiology*, vol. 219, no. 3, pp. 709–727, 1971.
[24] A. Rosendo, X. Liu, M. Shimizu, and K. Hosoda, "Stretch reflex improves rolling stability during hopping of a decerebrate biped system," *Bioinspiration & biomimetics*, vol. 10, no. 1, p. 016008, 2015.
[25] S. Grillner, "Neurobiological bases of rhythmic motor acts in vertebrates," *Science*, vol. 228, no. 4696, pp. 143–149, 1985.
[26] F. Delcomyn, "Neural basis of rhythmic behavior in animals," *Science*, vol. 210, no. 4469, pp. 492–498, 1980.
[27] E. Marder and D. Bucher, "Central pattern generators and the control of rhythmic movements," *Current biology*, vol. 11, no. 23, pp. R986–R996, 2001.
[28] A. H. Cohen and P. Wallén, "The neuronal correlate of locomotion in fish," *Experimental brain research*, vol. 41, no. 1, pp. 11–18, 1980.
[29] S. Grillner, T. Deliagina, A. El Manira, R. Hill, G. Orlovsky, P. Wallén, Ö. Ekeberg, and A. Lansner, "Neural networks that co-ordinate locomotion and body orientation in lamprey," *Trends in neurosciences*, vol. 18, no. 6, pp. 270–279, 1995.
[30] A. D. McClellan and W. Jang, "Mechanosensory inputs to the central pattern generators for locomotion in the lamprey spinal cord: resetting, entrainment, and computer modeling," *Journal of Neurophysiology*, vol. 70, no. 6, pp. 2442–2454, 1993.
[31] T. G. Brown, "The intrinsic factors in the act of progression in the mammal," *Proc. R. Soc. Lond. B*, vol. 84, no. 572, pp. 308–319, 1911.
[32] S. Rossignol, "Locomotion and its recovery after spinal injury," *Current opinion in neurobiology*, vol. 10, no. 6, pp. 708–716, 2000.
[33] D. M. Armstrong, "The supraspinal control of mammalian locomotion." *The Journal of physiology*, vol. 405, no. 1, pp. 1–37, 1988.
[34] A. Lundberg and C. Phillips, "T. graham brown's film on locomotion in the decerebrate cat." *The Journal of physiology*, vol. 231, no. 2, p. 90P, 1973.
[35] S. Grillner, A. Georgopoulos, and L. Jordan, *Neurons, networks, and motor behavior*. Citeseer, 1997.

[36] A. J. Ijspeert, "Central pattern generators for locomotion control in animals and robots: a review," *Neural Networks*, vol. 21, no. 4, pp. 642–653, 2008.
[37] T. G. Brown, "On the nature of the fundamental activity of the nervous centres; together with an analysis of the conditioning of rhythmic activity in progression, and a theory of the evolution of function in the nervous system," *The Journal of physiology*, vol. 48, no. 1, pp. 18–46, 1914.
[38] A. J. Ijspeert, "A connectionist central pattern generator for the aquatic and terrestrial gaits of a simulated salamander," *Biological cybernetics*, vol. 84, no. 5, pp. 331–348, 2001.
[39] D. A. McCrea and I. A. Rybak, "Organization of mammalian locomotor rhythm and pattern generation," *Brain research reviews*, vol. 57, no. 1, pp. 134–146, 2008.
[40] M. Lafreniere-Roula and D. A. McCrea, "Deletions of rhythmic motoneuron activity during fictive locomotion and scratch provide clues to the organization of the mammalian central pattern generator," *Journal of neurophysiology*, vol. 94, no. 2, pp. 1120–1132, 2005.
[41] P. J. Whelan, "Shining light into the black box of spinal locomotor networks," *Philosophical Transactions of the Royal Society of London B: Biological Sciences*, vol. 365, no. 1551, pp. 2383–2395, 2010.
[42] Y. Kuramoto, "Self-entrainment of a population of coupled non-linear oscillators," in *International symposium on mathematical problems in theoretical physics*. Springer, 1975, pp. 420–422.
[43] K. Matsuoka, "Sustained oscillations generated by mutually inhibiting neurons with adaptation," *Biological cybernetics*, vol. 52, no. 6, pp. 367–376, 1985.
[44] A. J. Ijspeert, A. Crespi, D. Ryczko, and J.-M. Cabelguen, "From swimming to walking with a salamander robot driven by a spinal cord model," *science*, vol. 315, no. 5817, pp. 1416–1420, 2007.
[45] C. S. Sherrington, "Flexion-reflex of the limb, crossed extension-reflex, and reflex stepping and standing," *The Journal of physiology*, vol. 40, no. 1-2, pp. 28–121, 1910.
[46] N. C. Heglund and C. R. Taylor, "Speed, stride frequency and energy cost per stride: how do they change with body size and gait?" *Journal of Experimental Biology*, vol. 138, no. 1, pp. 301–318, 1988.
[47] D. Owaki, T. Kano, K. Nagasawa, A. Tero, and A. Ishiguro, "Simple robot suggests physical interlimb communication is essential for quadruped walking," *Journal of The Royal Society Interface*, vol. 10, no. 78, p. 20120669, 2013.
[48] D. Owaki, L. Morikawa, and A. Ishiguro, "Listen to body's message: Quadruped robot that fully exploits physical interaction between legs," in *Intelligent Robots and Systems (IROS), 2012 IEEE/RSJ International Conference on*. IEEE, 2012, pp. 1950–1955.
[49] R. Pfeifer and J. Bongard, *How the body shapes the way we think: a new view of intelligence*. MIT press, 2006.
[50] N. J. Nilsson, "Shakey the robot," SRI INTERNATIONAL MENLO PARK CA, Tech. Rep., 1984.
[51] M. Raibert, K. Blankespoor, G. Nelson, R. Playter, and T. Team, "Bigdog, the rough-terrain quadruped robot," in *Proceedings of the 17th World Congress*, vol. 17, no. 1. Proceedings Seoul, Korea, 2008, pp. 10 822–10 825.

[52] M. Hutter, C. Gehring, D. Jud, A. Lauber, C. D. Bellicoso, V. Tsounis, J. Hwangbo, K. Bodie, P. Fankhauser, M. Bloesch, *et al.*, "Anymal-a highly mobile and dynamic quadrupedal robot," in *Intelligent Robots and Systems (IROS), 2016 IEEE/RSJ International Conference on*. IEEE, 2016, pp. 38–44.

[53] T. Kozuki, T. Hirose, T. Shirai, S. Nakashima, Y. Asano, Y. Kakiuchi, K. Okada, and M. Inaba, "Skeletal structure with artificial perspiration for cooling by latent heat for musculoskeletal humanoid kengoro," in *Intelligent Robots and Systems (IROS), 2016 IEEE/RSJ International Conference on*. IEEE, 2016, pp. 2135–2140.

[54] C. Laschi, B. Mazzolai, and M. Cianchetti, "Soft robotics: Technologies and systems pushing the boundaries of robot abilities," *Science Robotics*, vol. 1, no. 1, p. eaah3690, 2016.

[55] R. A. Brooks, "New approaches to robotics," *Science*, vol. 253, no. 5025, pp. 1227–1232, 1991.

[56] ——, "Intelligence without representation," *Artificial intelligence*, vol. 47, no. 1-3, pp. 139–159, 1991.

[57] K. Osuka, A. Ishiguro, X.-Z. Zheng, Y. Sugimoto, and D. Owaki, "Dual structure of mobiligence—implicit control and explicit control—," in *Intelligent Robots and Systems (IROS), 2010 IEEE/RSJ International Conference on*. IEEE, 2010, pp. 2407–2412.

[58] T. McGeer *et al.*, "Passive dynamic walking," *I. J. Robotic Res.*, vol. 9, no. 2, pp. 62–82, 1990.

[59] S. Collins, A. Ruina, R. Tedrake, and M. Wisse, "Efficient bipedal robots based on passive-dynamic walkers," *Science*, vol. 307, no. 5712, pp. 1082–1085, 2005.

[60] 杉本靖博 and 大須賀公一, "受動的動歩行の安定性に関する一考察," **システム制御情報学会論文誌**, vol. 18, no. 7, pp. 255–260, 2005.

[61] K. Osuka, K. Nakatani, Y. Sugimoto, and T. Akazawa, "On existence of multi-legged passive dynamic walking -one-legged, tow-legged, four-legged, six-legged...?-," in *Symposium on Control Theory*, vol. 36. SICE, 2007, pp. 95–98.

[62] K. Nakatani, Y. Sugimoto, and K. Osuka, "Demonstration and analysis of quadrupedal passive dynamic walking," *Advanced Robotics*, vol. 23, no. 5, pp. 483–501, 2009.

[63] D. Owaki, K. Osuka, and A. Ishiguro, "On the embodiment that enables passive dynamic bipedal running," in *Robotics and Automation (ICRA), 2008 IEEE International Conference on*. IEEE, 2008, pp. 341–346.

[64] K. Osuka, T. Kinugasa, R. Hayashi, K. Yoshida, D. Owaki, and A. Ishiguro, "i-CentiPot: A centipede-like robot wanders in the wilderness," in *The 8th International Symposium on Adaptive Motion of Animals and Machines, Sapporo, Japan*, 2017.

[65] R. Pfeifer and G. Gómez, "Morphological computation–connecting brain, body, and environment," *Creating brain-like intelligence*, pp. 66–83, 2009.

[66] R. Pfeifer, F. Iida, and J. Bongard, "New robotics: Design principles for intelligent systems," *Artificial life*, vol. 11, no. 1-2, pp. 99–120, 2005.

[67] M. H. Raibert, "Legged robots," *Communications of the ACM*, vol. 29, no. 6, pp. 499–514, 1986.

[68] I. Poulakakis, E. Papadopoulos, and M. Buehler, "On the stability of the passive dynamics of quadrupedal running with a bounding gait," *The International Journal of*

Robotics Research, vol. 25, no. 7, pp. 669–687, 2006.

[69] A. T. Sprowitz, A. Tuleu, A. J. Ijspeert, *et al.*, "Kinematic primitives for walking and trotting gaits of a quadruped robot with compliant legs," *Frontiers in computational neuroscience*, vol. 8, p. 27, 2014.

[70] A. Spröwitz, A. Tuleu, M. Vespignani, M. Ajallooeian, E. Badri, and A. J. Ijspeert, "Towards dynamic trot gait locomotion: Design, control, and experiments with cheetah-cub, a compliant quadruped robot," *The International Journal of Robotics Research*, vol. 32, no. 8, pp. 932–950, 2013.

[71] Q. Cao and I. Poulakakis, "Passive quadrupedal bounding with a segmented flexible torso," in *Intelligent Robots and Systems (IROS), 2012 IEEE/RSJ International Conference on*. IEEE, 2012, pp. 2484–2489.

[72] B. Zachary, K. Joohyung, and Y. Katsu, "Untethered one legged hopping in 3d using linear elastic actuator in parallel (leap)," in *In the 14th International Symposium on Experimental Robotics (ISER*, 2016.

[73] D. W. Haldane, M. M. Plecnik, J. K. Yim, and R. S. Fearing, "Robotic vertical jumping agility via series-elastic power modulation," *Science Robotics*, vol. 1, no. 1, 2016.

[74] C. Hubicki, J. Grimes, M. Jones, D. Renjewski, A. Spröwitz, A. Abate, and J. Hurst, "Atrias: Design and validation of a tether-free 3d-capable spring-mass bipedal robot," *The International Journal of Robotics Research*, p. 0278364916648388, 2016.

[75] G. Kenneally, A. De, and D. Koditschek, "Design principles for a family of direct-drive legged robots," *IEEE Robotics and Automation Letters*, vol. 1, no. 2, pp. 900–907, 2016.

[76] R. Altendorfer, D. E. Koditschek, and P. Holmes, "Stability analysis of a clock-driven rigid-body slip model for rhex," *The International Journal of Robotics Research*, vol. 23, no. 10-11, pp. 1001–1012, 2004.

[77] M. Reis and F. Iida, "An energy-efficient hopping robot based on free vibration of a curved beam," *IEEE/ASME Transactions on Mechatronics*, vol. 19, no. 1, pp. 300–311, 2014.

[78] M. Reis, X. Yu, N. Maheshwari, and F. Iida, "Morphological computation of multi-gaited robot locomotion based on free vibration," *Artificial life*, vol. 19, no. 1, pp. 97–114, 2013.

[79] D. Owaki, M. Goda, S. Miyazawa, and A. Ishiguro, "A minimal model describing hexapedal interlimb coordination: The tegotae-based approach," *Frontiers in neurorobotics*, vol. 11, p. 29, 2017.

[80] Y. Kurita, Y. Matsumura, S. Kanda, and H. Kinugasa, "Gait patterns of quadrupeds and natural vibration modes," *Journal of System Design and Dynamics*, vol. 2, no. 6, pp. 1316–1326, 2008.

[81] H. M. Oliveira and L. V. Melo, "Huygens synchronization of two clocks," *Scientific reports*, vol. 5, p. 11548, 2015.

[82] B. Van der Pol, "relaxation-oscillations," *The London, Edinburgh, and Dublin Philosophical Magazine and Journal of Science*, vol. 2, no. 11, pp. 978–992, 1926.

[83] B. M. Boszczyk, A. A. Boszczyk, and R. Putz, "Comparative and functional anatomy of the mammalian lumbar spine," *The Anatomical Record*, vol. 264, no. 2, pp. 157–168, 2001.

[84] I. Boyd, "The isolated mammalian muscle spindle," *Trends in neurosciences*, vol. 3, no. 11, pp. 258–265, 1980.
[85] A. Prochazka, M. Hulliger, P. Trend, and N. Dürmüller, "Dynamic and static fusimotor set in various behavioural contexts," in *Mechanoreceptors*. Springer, 1988, pp. 417–430.
[86] D. T. McRuer, R. E. Magdaleno, and G. P. Moore, "A neuromuscular actuation system model," *IEEE Transactions on Man-Machine Systems*, vol. 9, no. 3, pp. 61–71, 1968.
[87] I. A. Rybak, N. A. Shevtsova, M. Lafreniere-Roula, and D. A. McCrea, "Modelling spinal circuitry involved in locomotor pattern generation: insights from deletions during fictive locomotion," *The Journal of physiology*, vol. 577, no. 2, pp. 617–639, 2006.
[88] H. Geyer and H. Herr, "A muscle-reflex model that encodes principles of legged mechanics produces human walking dynamics and muscle activities," *IEEE Transactions on neural systems and rehabilitation engineering*, vol. 18, no. 3, pp. 263–273, 2010.
[89] J. G. Nicholls, A. R. Martin, B. G. Wallace, and P. A. Fuchs, *From neuron to brain*. Sinauer Associates Sunderland, MA, 2001, vol. 271.
[90] P. Matthews, "Muscle spindles and their motor control," *Physiological Reviews*, vol. 44, no. 2, pp. 219–288, 1964.
[91] E. R. Kandel, J. H. Schwartz, T. M. Jessell, S. A. Siegelbaum, and A. J. Hudspeth, *Principles of neural science*. McGraw-hill New York, 2000, vol. 4.
[92] N. Hogan, "Adaptive control of mechanical impedance by coactivation of antagonist muscles," *IEEE Transactions on Automatic Control*, vol. 29, no. 8, pp. 681–690, 1984.
[93] A. V. Hill, "The heat of shortening and the dynamic constants of muscle," in *Proc. R. Soc. Lond. B*, vol. 126, no. 843. The Royal Society, 1938, pp. 136–195.
[94] J. M. Winters and L. Stark, "Muscle models: what is gained and what is lost by varying model complexity," *Biological cybernetics*, vol. 55, no. 6, pp. 403–420, 1987.
[95] M. R. Dimitrijevic, Y. Gerasimenko, and M. M. Pinter, "Evidence for a spinal central pattern generator in humansa," *Annals of the New York Academy of Sciences*, vol. 860, no. 1, pp. 360–376, 1998.
[96] K. A. Daltorio, A. S. Boxerbaum, A. D. Horchler, K. M. Shaw, H. J. Chiel, and R. D. Quinn, "Efficient worm-like locomotion: slip and control of soft-bodied peristaltic robots," *Bioinspiration & biomimetics*, vol. 8, no. 3, p. 035003, 2013.
[97] D. Zarrouk, I. Sharf, and M. Shoham, "Conditions for worm-robot locomotion in a flexible environment: theory and experiments," *IEEE Transactions on Biomedical engineering*, vol. 59, no. 4, pp. 1057–1067, 2012.
[98] C.-W. Song, D.-J. Lee, and S.-Y. Lee, "Bioinspired segment robot with earthworm-like plane locomotion," *Journal of Bionic Engineering*, vol. 13, no. 2, pp. 292–302, 2016.
[99] S. Seok, C. D. Onal, K.-J. Cho, R. J. Wood, D. Rus, and S. Kim, "Meshworm: a peristaltic soft robot with antagonistic nickel titanium coil actuators," *IEEE/ASME Transactions on mechatronics*, vol. 18, no. 5, pp. 1485–1497, 2013.
[100] B. Kim, M. G. Lee, Y. P. Lee, Y. Kim, and G. Lee, "An earthworm-like micro robot using shape memory alloy actuator," *Sensors and Actuators A: Physical*, vol. 125, no. 2, pp. 429–437, 2006.
[101] D. Gu and Y. Zhou, "An approach to the capsule endoscopic robot with active drive motion," *Journal of Zhejiang University-SCIENCE A*, vol. 12, no. 3, pp. 223–231,

2011.
[102] A. Menciassi, S. Gorini, G. Pernorio, and P. Dario, "A sma actuated artificial earthworm," in *Robotics and Automation (ICRA), 2004 IEEE International Conference on*, vol. 4. IEEE, 2004, pp. 3282–3287.
[103] B. Trimmer and H.-t. Lin, "Bone-free: Soft mechanics for adaptive locomotion," 2014.
[104] H. Fang, Y. Zhang, and K. Wang, "Origami-based earthworm-like locomotion robots," *Bioinspiration & biomimetics*, vol. 12, no. 6, p. 065003, 2017.
[105] K. Jung, J. C. Koo, Y. K. Lee, H. R. Choi, *et al.*, "Artificial annelid robot driven by soft actuators," *Bioinspiration & biomimetics*, vol. 2, no. 2, p. S42, 2007.
[106] N. Saga and T. Nakamura, "Development of a peristaltic crawling robot using magnetic fluid on the basis of the locomotion mechanism of the earthworm," *Smart materials and structures*, vol. 13, no. 3, p. 566, 2004.
[107] A. A. Calderón, J. C. Ugalde, J. C. Zagal, and N. O. Pérez-Arancibia, "Design, fabrication and control of a multi-material-multi-actuator soft robot inspired by burrowing worms," in *Robotics and Biomimetics (ROBIO), 2016 IEEE International Conference on*. IEEE, 2016, pp. 31–38.
[108] S. Schwebke and C. Behn, "Worm-like robotic systems: Generation, analysis and shift of gaits using adaptive control," *Artificial Intelligence Research*, vol. 2, no. 1, p. 12, 2012.
[109] C. Behn, "Adaptive control of straight worms without derivative measurement," *Multibody System Dynamics*, vol. 26, no. 3, pp. 213–243, 2011.
[110] H. Fang, C. Wang, S. Li, K. Wang, and J. Xu, "A comprehensive study on the locomotion characteristics of a metameric earthworm-like robot," *Multibody system dynamics*, vol. 35, no. 2, pp. 153–177, 2015.
[111] H. Fang, S. Li, K. Wang, and J. Xu, "Phase coordination and phase–velocity relationship in metameric robot locomotion," *Bioinspiration & biomimetics*, vol. 10, no. 6, p. 066006, 2015.
[112] I.-M. Chen, S. H. Yeo, and Y. Gao, "Locomotive gait generation for inchworm-like robots using finite state approach," *Robotica*, vol. 19, no. 5, pp. 535–542, 2001.
[113] T. Kano and A. Ishiguro, "Decentralized control of earthworm-like robot based on tegotae function," in *The 8th International Symposium on Adaptive Motion of Animals and Machines (AMAM), 2017*, 2017, pp. 92–93.
[114] T. Umedachi, T. Kano, A. Ishiguro, and B. A. Trimmer, "Gait control in a soft robot by sensing interactions with the environment using self-deformation," *Royal Society open science*, vol. 3, no. 12, p. 160766, 2016.

Related papers

The results of this thesis is published in the following articles.

Chapter 2

Yoichi Masuda, Keisuke Naniwa, Masato Ishikawa, and Koichi Osuka, “Weak Actuators Generate Adaptive Animal Gaits without a Brain.” IEEE International Conference on Robotics and Biomimetics (ROBIO2017), China, Macau SAR, December, 2017.

Chapter 3

Yoichi Masuda, Yuki Minami, Masato Ishikawa, “Vibration-Based Motion Generation without Any Sensor or Microprocessor.” Asian Journal of Control. (submitted)

Chapter 4

Yoichi Masuda, Masato Ishikawa, “Simple Reflex Controller for Decentralized Motor Coordination Based on Resonant Oscillation” MDPI Robotics, Vol. 7, No. 23. 2018.

Chapter 5

Yoichi Masuda, Yasuhiro Sugimoto, Masato Ishikawa, “Muscles Excite and Synchronize Themselves through Body Dynamics.” Nonlinear Theory and Its Applications, Vol. E10-N, No.2, 2019. (to appear)

Appendix A

Yoichi Masuda, Masato Ishikawa, Akio Ishiguro “Weak DC Motors Generate Earthworm Locomotion Without a Brain.” in Proceedings of The 7th International Conference on Biomimetic and Biohybrid Systems (Living Machine 2018), France, Paris, pp. 304-315, 2018.

Pulication list

Journal papers

[1] 増田容一，長瀬賢二,「自己釣り合い状態を利用したマルチエージェントシステムのフォーメーション制御」計測自動制御学会論文集，計測自動制御学会，Vol. 51，No. 10，pp. 744-754，2015.

[2] Yoichi Masuda, Masato Ishikawa, “Simplified Triped Robot for Analysis of Three-Dimensional Gait Generation.” Journal of Robotics and Mechatronics, Vol. 29, No. 3, 2017.

[3] Yoichi Masuda, Masato Ishikawa, “Simple Reflex Controller for Decentralized Motor Coordination Based on Resonant Oscillation” MDPI Robotics, Vol. 7, No. 23. 2018.

[4] Yoichi Masuda, Yasuhiro Sugimoto, Masato Ishikawa, “Muscles Excite and Synchronize Themselves through Body Dynamics.” Nonlinear Theory and Its Applications, Vol. E10-N, No.2, 2019. (to appear)

[5] Yoichi Masuda, Yuki Minami, Masato Ishikawa, “Vibration-Based Motion Generation without Any Sensor or Microprocessor.” Asian Journal of Control. (submitted)

Refereed international conference papers

[1] Yoichi Masuda, Kenji Nagase, “Optimal internal force design for formation control of multi-agent systems.” 2015 15th International Conference on Control, Automation and Systems (ICCAS2015), Busan, Korea, October, 2015.

[2] Yoichi Masuda, Kenji Nagase, “Adaptive formation control with self-equilibrium forces.” IEEE/ASME International Conference on Advanced Intelligent Mechatronics (AIM2016), Banff, Canada, July, 2016.

[3] Yoichi Masuda, Masato Ishikawa, “LigamentalJoint: A Tough and Ultra-lightweight Revolute Joint.” Adaptive Motion of Animals and Machines (AMAM2017), Hokkaido, June, 2017.

[4] Yoichi Masuda, Masato Ishikawa, “Development of a Deformation-driven Rolling Robot with a Soft Outer Shell.” IEEE/ASME International Conference on Advanced Intelligent Mechatronics (AIM2017), Munich, Germany, July, 2017.

[5] Yoichi Masuda, Masato Ishikawa, “Muscles Excite and Synchronize Themselves through Their Intrinsic Dynamics” The 2017 International Symposium on Nonlinear Theory and Its Applications (NOLTA2017), Cancun, Mexico, December, 2017.

[6] Yoichi Masuda, Yuki Minami, Masato Ishikawa, “Actuator Synchronization for Adaptive Motion Generation without Any Sensor or Microprocessor.” Asian Control Conference (ASCC2017), Australia, Goald Coast, December, 2017.

[7] Yoichi Masuda, Keisuke Naniwa, Masato Ishikawa, and Koichi Osuka, “Weak Actuators Generate Adaptive Animal Gaits without a Brain.” IEEE International Conference on Robotics and Biomimetics (ROBIO2017), China, Macau SAR, December, 2017.

[8] Yoichi Masuda, Masato Ishikawa, Akio Ishiguro “Weak DC Motors Generate Earthworm Locomotion Without a Brain.” in Proceedings of The 7th International Conference on Biomimetic and Biohybrid Systems (Living Machine 2018), France, Paris, pp. 304-315, 2018.

Domestic conference papers

[1] 増田容一，安田一則，「ディスクリプタシステムに対するオブザーバを用いたスライディングモード制御」日本機械学会関西学生会 学生員卒業研究発表講演会，大阪工業大学大宮キャンパス，3 月，2013.

[2] 増田容一，長瀬賢二，「形状と応力の同時最適化によるテンセグリティ構造の最小質量設計」日本機械学会 2014 年度年次大会，東京電機大学 東京千住キャンパス，9 月，2014.

[3] 増田容一，長瀬賢二，「グラフラプラシアンを用いたマルチエージェントシステムのフォーメーション形状の制御」計測自動制御学会 第 20 回創発システム・シンポジウム，諏訪東京理科大学，8 月，2014.

[4] 増田容一，長瀬賢二，「展開・転がり可能な張力構造物のためのアクチュエータ配置の検討」日本機械学会ロボティクス・メカトロニクス講演会，2P1-15a7，パシフィコ横浜，6 月，2016.

[5] 増田容一，石川将人，「ダイレクトフォースフィードバックを用いた位相振動子による三脚ロボットの歩容生成」第 17 回計測自動制御学会システムインテグレーション部門講演会（SI2016），12 月，2016.

[6] 増田容一，石川将人，石黒章夫，「コントローラをもたない無脳ヘビ型ロボットの適応的運動生成」第 30 回自律分散システムシンポジウム（DAS2017），仙台，1 月，2018.

[7] 増田容一，浪花啓右，石川将人，大須賀公一，「コントローラをもたない無脳 6 脚ロボットの適応的運動生成」第 62 回システム制御情報学会研究発表講演会 (SCI’18)，京都，5 月，2018.

[8] 増田容一，石川将人，「コントローラをもたない無脳三脚ロボットの適応的運動生成」日本機械学会ロボティクス・メカトロニクス講演会，1P1-F15，北九州国際コンベンションゾーン，6 月，2018.

Co-authored papers

[1] Keisuke Naniwa, Yoichi Masuda, Masato Ishikawa, K. Osuka, “Weak Actuators Generate Versatile Locomotion Patterns without a Brain.” IEEE International Conference on Robotics and Biomimetics (ROBIO2017), China, Macau SAR, December, 2017.

[2] 田中颯樹，増田容一，石川将人，「アクチュエータの弱さによる跳躍安定化メカニズム」計測自動制御学会論文集.（採録決定）

[3] 田中颯樹，増田容一，石川将人，「アクチュエータの「弱さ」を利用した跳躍ロボットの非線形力学解析」, 第 18 回システムインテグレーション部門講演会（SI2017），12 月，仙台，2017.

[4] 藤田帝智，増田容一，石川将人，「腹足モデルに基づくカタツムリの這行ロコモーションの解析」第 62 回システム制御情報学会研究発表講演会 (SCI’18)，京都，5 月，2018.

[5] 徳田献一，前岡俊，増田容一，石川将人，大須賀公一，「脚ごとに独立した CPG をもつ多脚移動ロボットモジュール」日本機械学会ロボティクス・メカトロニクス講演会，2P1-F17，北九州国際コンベンションゾーン，6 月，2018.

[6] 重吉比呂，末岡裕一郎，増田容一，石川将人，大須賀公一，「自己相似性から着想を得た脚ロボット Martian fractal の開発」第 19 回システムインテグレーション部門講演会（SI2018），12 月，大阪，2018.

Others

[1] 増田容一，「目で見る海外論文発表」生産と技術，Vol. 70, No. 2, pp. 117, 2018.

[2] 増田容一，長瀬賢二，「マルチエージェントシステムにおける制御力の自己釣り合いと剛性行列の最大固有値」第 3 回 JST 数学領域横断若手合宿，ウェスティンホテル淡路，2 月，2016.

[3] 増田容一，石川将人，「寄生型マスドライバによる力学系の励振制御」, Advanced Theory and Application of Control Systems 研究会 , 東京，2016.

[4] 増田容一，石川将人，「無脳歩行現象の発見と解析～生物の運動原理解明に向けて～」ECSRA 研究会，10 月，2018.

[5] Patent: 特許出願 2017-121695．増田容一，石川将人，「関節機構」，出願日 2017 年 6 月.

Media

[1] “Weak, Brainless Quadruped Robot Autonomously Generates Gaits.” IEEE spectrum, 2017.

[2] “Martian-Inspired Tripod Walking Robot Generates Its Own Gaits.” IEEE spectrum, 2017.

[3] “Video Friday: More Boston Dynamics, Giant Fighting Robots, and ANYmal quadruped.” IEEE spectrum, 2017.

[4] “Could This Squishy Robot Be the Future of Robotics?.” GIZMODO, 2017.

[5] “輪っかを変形させてコロコロ進むロボット” GIZMODO ジャパン, 2017.

Research supports

[1] 「日本教育公務員弘済会和歌山支部平成 24 年度学校研究活動支援事業 研究助成」, 2012.

[2] 「公益財団法人立石科学技術振興財団 研究助成 (C)」, 2016.

[3] 「日本学術振興会 特別研究員 DC2」, 2017 年 4 月から 2019 年 3 月まで.